Title: Implementing an empirical scalar tertiary anisotropic rheology (ESTAR) into large-scale ice sheet models

Authors: Felicity Graham, Mathieu Morlighem, Roland Warner, and Adam Treverrow

Overall response to the reviewers

We thank the reviewers for their initial comments, which have led to a substantially improved manuscript.

The two main points highlighted by both reviewers concern the philosophy underlying ESTAR, specifically whether or not it can be regarded as a physically-based anisotropic rheology that is applicable for most of the ice sheet. We recognise that an understanding of the conceptual basis behind ESTAR, particularly how it relates to anisotropic properties of polar ice and tertiary creep, is important and deserves discussion.

However, the main aim of this paper is not to provide a comprehensive review of anisotropic flow relations, nor a justification of ESTAR or comparison of ESTAR with other anisotropic approaches (e.g., fabric based rheologies). Instead, the aim of this manuscript is to present the implementation and some initial testing of ESTAR within the context of a numerical ice sheet model. We are not introducing ESTAR for the first time: it was derived and discussed in detail in Budd et al. (2013) and a comparison of a simplified version of the generalised ESTAR from Budd et al. (2013) with some of the leading anisotropic flow relations was undertaken by Treverrow et al. (2015). A detailed reprise of Budd et al. (2013) is not feasible here, and would be inappropriate in the present context.

Nevertheless, we provide comments to the reviewer's main points below, and have amended the manuscript, where appropriate. In particular, we have expanded on the background to anisotropic flow relations (Sect. 2), modified the results section (Sect. 5), included ISMIP-HOM experiments investigating the impact of aspect ratios, as suggested. We have modified and reordered the discussion section (Sect. 6) to discuss more broadly the relevance and applicability of ESTAR, and have expanded on the conclusions (Sect. 7).

Our responses to each of the reviewers' specific comments are below, with text from each reviewer's comments presented in italics. Where necessary, we have segmented the reviewers' comments to deal with specific issues sequentially.

All line number and figure references are to the revised manuscript unless otherwise indicated.

A version of the manuscript with all changes marked-up is provided at the end of this response document.

Kind regards,

Dr Graham and coauthors

REVIEWER 1

Main point

R1: My main concern with this paper is that ESTAR is presented as a physically-based alternative to represent the anisotropic rheological properties of polar ice. There is 2 problems with this presentation; first ESTAR is not an anisotropic flow relation; second, ESTAR is based from laboratory measurements for tertiary creep of polycrystalline ice and thus does not apply in large portions of the ice-sheet. I detail these two points below.

Point 1: Anisotropy:

R1: It can only be applied to properties that depend on the orientation of the material. Here the flow relation (3) is stress-configuration dependant, but is isotropic; i.e. for a given stress state, the mechanical response (the strain-rate state) does not change by rotation of the sample as, by definition of ESTAR, the fabric instantaneously adapt to the stress state, and thus to any rotation of the stress state. The dependance of the flow law to the stress state, results from the mechanical anisotropy of the ice crystal and the anisotropy of the crystal orientations (the fabric) that develop during tertiary creep; but the mechanical behaviour predicted by ESTAR is isotropic. Note that this property is not due to the scalar relationship, the CAFFE model (e.g. Seddik et al., J. Glaciol. 2008) is anisotropic as its scalar enhancement factor depends on the direction of the stress state with respect to the ice fabric, and thus the mechanical response depends on the orientation of the stress state relative to the ice sample.

We are certainly presenting ESTAR as a physically-based alternative to the standard Glen flow relation.

The reviewer is incorrect in stating that ESTAR is isotropic. The conceptual origin of the description of anisotropy in ESTAR is based on considerable observations from ice cores, boreholes and laboratory experiments (e.g. Jacka and Maccagnan, 1984; Dahl-Jensen and Gundestrup, 1987; Gao and Jacka, 1987; Budd and Jacka, 1989; Etheridge, 1989; Li and Jacka, 1998; Morgan et al., 1998; Wang and Warner, 1999; Treverrow et al., 2012). Observations such as these demonstrate that if the stress configuration is changed within a fixed reference frame then the compatible fabric that develops in response to that stress is correspondingly altered, i.e. specific fabric patterns are associated with specific stress configurations (note that in the following we use the term 'fabric' to describe the distribution of crystallographic c-axis orientations). This is valid provided that the stress configuration remains stable for a period that exceeds the time (or strain) required for the microstructure to adapt to that state of stress. Since polycrystalline anisotropy is fundamentally linked to microstructure (including fabric, but not exclusively so) the anisotropic response of an aggregate can be directly related to the present stress configuration, if that is a suitable indication of a persistent recent strain history.

Identification of the local non-rotating shear plane (normal, n), the simple shear stress, τ', acting on that plane and its magnitude relative to the total effective stress, τ_e, summarise the computational framework for specifying the anisotropic enhancement factor, $E(\lambda_S)$, in ESTAR (Equations 4-6). The parameter λ_S also characterises the fabric pattern, i.e., when $\lambda_S = 1$ there will be a strong single maximum, while when $\lambda_S = 0$, there will be c-axes concentrated around a conical surface centred on the compression axis – a small circle girdle. The anisotropy of $E(\lambda_S)$ is derived from the spatial variability in the flow field and its dependence on the deformational component of the vorticity.

The concepts of rheology and its description in a flow relation can sometimes become confused. ESTAR is the representation of the deformational response of ice with a crystal fabric anisotropy compatible with prolonged deformation under a stable stress regime – this is the 'tertiary' aspect of ESTAR. When the compatibility requirement is considered, it is clear that there is no sense in contemplating arbitrary rotations between the stress configuration and anisotropic crystal fabrics – this relates to the deformability of anisotropic ice. Regarded in this light, it seems to us that the suggestions of both reviewers that one could meaningfully consider an arbitrary rotation of spatially anisotropic material properties and the applied stresses breaks the intrinsic point of ESTAR. The point also seems semantic – the rheology of polycrystalline anisotropic ice versus an anisotropic rheological description for polycrystalline ice.

This reviewer notes correctly that the enhancement factor in the CAFFE flow relation is anisotropic since it is defined by the local stress field and its orientation relationship with respect to a polycrys-

talline aggregate, and rotation of one relative to the other produces a different effect. In CAFFE the explicit inclusion of fabric in defining the deformability of polycrystalline ice allows the instantaneous flow response for any arbitrary combination of stress and fabric to be calculated. CAFFE and ESTAR are structurally similar in featuring a collinear relationship between stress and strain rate tensor components and hence each can be interpreted as an enhancement factor, defined as a function of some experimentally-based enhancement parameters and the local stress field. A key difference between the two relations is that for ESTAR fabric is not explicitly included in specification of the enhancement. By linking the enhancement directly to the relative magnitude of the components of σ' via $E(\lambda_S)$, ESTAR is restricted to a subset of the fabric/stress combinations that can be contemplated with microstructure based approaches, such as CAFFE. Importantly, these combinations where ESTAR is applicable are those where fabric has evolved to be compatible with the local stress field. Put another way, ESTAR only allows contemplation of tertiary creep (addressed on P2L5-13; P5L5-18; P7L1-4). This is not a problem since tertiary creep is relevant to the vast majority of the most dynamically active regions of an ice sheet. In the revised manuscript, we have noted examples where this might not be the case (P5L21-P6L12):

"There are of course zones within an ice sheet where the assumption of compatible tertiary flow will not apply; however, we note that these zones will be restricted in their extent. We contend that ESTAR will apply to the vast majority of the dynamically active regions of an ice sheet, in particular those zones where creep deformation makes a significant contribution to the overall flow. Specific zones where the assumption of tertiary creep may be inappropriate can be summarised as those where fabric has not yet evolved compatibility with the flow, where there is a rapid transition in the flow configuration, or where creep deformation makes only a minor contribution to the overall dynamics.

For example, in very cold ice in a low stress setting, such as the uppermost layers of the polar ice sheets, the time required to accumulate the strain necessary to develop a compatible fabric may lead to a near-surface zone in which the assumption of tertiary creep is not valid. Since the development of anisotropic fabrics provides an indication of the existence of tertiary flow, their observation at modest depths, (e.g., $\lesssim 100 - 200$ m; Morgan et al., 1997; DiPrinzio et al., 2005; Treverrow et al., 2016) allows estimation of the maximum extent of the zone where tertiary creep is not occurring. The observation within polar firn of microdeformation processes that are necessary for the development of fabric throughout ice sheets (e.g. Kipfstuhl et al., 2009; Faria et al., 2014) suggests that it may be appropriate to even further restrict the extent of the near-surface zone for which the assumption of tertiary creep is not valid. Additionally, the nonlinear nature of polycrystalline ice rheology leads to very high viscosities in low temperature and stress environments, so that incorrectly estimating deformation rates due to the assumption of tertiary flow in such regions may be of limited importance to simulations of ice sheet evolution.

Regions where rapid transitions in dynamic conditions can lead to abrupt changes in the pattern of applied stresses and a potential breakdown in tertiary flow compatibility include ice shelf grounding zones and other locations where basal traction is lost or abruptly changes, e.g., where ice flows over a subglacial lake, or with the onset of basal sliding in ice streams. The convergence zones where tributary glaciers or ice streams merge with a larger flow unit at a high angle may also lead to a transition in dynamic conditions that is problematic for the assumption of tertiary compatibility. Of course the more highly dynamic the evolving flow regime, the more rapidly a new compatible anisotropy will be established, so that the spatial interval where the flow relations are inapplicable may be limited. While there is little guidance on how to extend

empirical flow relations to parametrise ice rheology in these transition regions, we note that similar difficulties exist for a Glen-type flow relation, which unlike ESTAR does not have the benefit of being able to correctly describe anisotropic enhancement throughout the remainder of the ice sheet."

That tertiary creep is relevant to the majority of the ice sheet is crucial and is dealt with further in responding to **Point 2**.

Point 2: Tertiary creep

R1: In the paper tertiary creep is presented as "the predominant mode of deformation in ice sheets", under the justification that it is usually reached after few percent of deformation in laboratory creep experiments. For a detail review on the ductile deformation of ice and textures in polar ice masses one can refer to the book "creep and fracture of ice" by Schulson and Duval. Tertiary creep in laboratory experiments is explained by softening processes associated with migration recrystallization. Textures resulting from migration recrystallization are indeed stress-configuration depend and the argument that the microstructure evolves more rapidly than the flow configuration sufficiently robust to assume a scalar isotropic relationship in the context of large scale ice flow modelling. In the central part of the ice-sheets, temperature and strain energy can be too low to initiate migration recrystallization and there is no evidence that it occurs except in the warm ice near the bed (the last 100-200 meters usually). See texture measurements in all deep ice cores in the central regions of Greenland and Antarctica. There is a general agreement that in the regions of normal grain growth and rotation recrystallization (most of the ice thickness in the central regions) basically develops as the results of lattice rotation due to intractrystalline slip; and thus reflect the deformation history.

The suggestion being made by the reviewer here seems to be that for laboratory experiments conducted at relatively high temperatures, tertiary creep is heavily influenced by migration recrystallisation, and that the results of such experiments are not representative of polar ice dynamics. The extension of this argument is that at lower temperatures boundary migration (a process which allows microstructural recovery during deformation) is less effective and does not contribute to fabric development. It seems this line of reasoning is then used to discount our expectation that appropriate fabrics, and perhaps tertiary creep conditions will be found in polar ice masses.

Following Schulson and Duval (2009), the reviewer states that fabric development at low temperatures is largely attributed to rotation recrystallisation – a deformation process, without the accompanying recovery afforded by boundary migration. Consequently for different polycrystalline aggregates, deformed under identical conditions of stress, it is suggested that the resultant fabric patterns will vary as a function of temperature due to the activity or otherwise of migration recrystallisation. As per Schulson and Duval (2009) the temperature at which migration recrystallisation is claimed to be sufficiently depressed, so that it no longer contributes significantly to fabric development, is $\sim -15°$C. Differences in the fabrics that are supposed to form in uniaxial compression at various temperatures are provided by Schulson and Duval (2009) as evidence to support this view. The small circle girdle (or cone-type) fabrics that form at higher temperatures are claimed to give way to single maximum (or cluster-type) fabrics at lower temperatures and stresses. The suggested implication of this for ESTAR is that the enhancement parameter derived for uniaxial compression from laboratory experiments is not valid for ice sheets. There are two problems with this argument and these appear to relate directly to the reviewer's concerns about how widespread tertiary creep is within an ice sheet. These issues are addressed in detail below, following a summary reiterating our view, before returning to the rest of the reviewer's comments.

4

More broadly, as described in Budd et al. (2013), tertiary creep describes a state of deformation where the microstructure within a polycrystalline aggregate has evolved to be compatible with the stress field, and this results in the development of polycrystalline anisotropy. A conspicuous feature of tertiary creep is the development of a fabric and to an extent one can remain agnostic about the actual microdeformation and recovery mechanisms that contribute to the development of this state. The anisotropic nature of the macroscopic response, and its spatial variability, is of primary importance to modelling large-scale ice sheet dynamics, not the specific mechanisms of microdeformation.

In short, we consider tertiary creep to be far more widespread than reviewer 1 claims it to be. Of course there are zones within the ice sheet where tertiary creep is not relevant and the manuscript has been altered to more clearly highlight these (e.g., P5L21-P6L12 – as quoted directly in our response to **Point 1** above).

Comment to the reviewer on fabric development and the extent of tertiary creep in ice sheets

First we discuss the temperature range over which small circle girdle fabrics occur in response to uniaxial compression and then we address the issue of whether or not a single maximum fabrics can be associated with uniaxial compression.

Small circle girdle/cone-type fabrics

From laboratory experiments there is considerable evidence (e.g. Jacka and Maccagnan, 1984; Jacka, 1984; Gao and Jacka, 1987; Jacka and Li, 2000; Treverrow et al., 2012) supporting the formation of small circle girdle fabrics in response to uniaxial compression. That this occurs is not in question here, rather it is the issue of to what extent similar patterns have been observed in the polar ice sheets.

Law Dome in East Antarctica provides a good example of an approximately radial dome whose dynamics are mostly isolated from the remainder of the Antarctic Ice Sheet. Observations from the A001 core drilled at Law Dome summit, where the ice thickness is $\sim 1200\,\mathrm{m}$ show a distinct small circle girdle fabric at a depth of $318\,\mathrm{m}$ (see Fig. 3a, Budd and Jacka, 1989). At this depth uniaxial compression is expected to be dominant and the in situ temperature is $\sim -22°\mathrm{C}$. We highlight this observation since it demonstrates that small circle girdle fabrics can form in response to uniaxial compression at temperatures below the $\sim -15°\mathrm{C}$ threshold for the activity for migration recrystallisation that is suggested by Schulson and Duval (2009). Small circle girdle fabrics have been recorded at many other locations, e.g. cores drilled at Siple Dome (DiPrinzio et al., 2005), Byrd (Gow and Williamson, 1976), Dye 3, Greenland (Herron et al., 1985) and the Amery (Budd, 1972) and Ross ice shelves (Gow, 1963). Importantly, some of these observations correspond to locations where the in situ temperatures were even lower than the $\sim -22°\mathrm{C}$ described for the Law Dome, A001 example.

Perhaps one reason why small circle girdle fabrics are considered by some to be the preserve of uniaxial compression laboratory experiments conducted at high temperatures and/or stresses is that these fabrics are not frequently identified in ice cores since ideal dome summits are uncommon, i.e., the vertical shortening is typically associated with different horizontal strain rate components in radial directions, particularly at depth. Even at sites that provide a good approximation of a dome surface, the inevitable depth-evolution of the flow configuration leads to correspondingly different fabrics. Indeed, at ice divides a nearly 2D plane-strain flow can be expected.

Under conditions of plane-strain a restricted form of the cone-type fabric pattern is encountered. These are 2-pole fabrics where the individual maxima are aligned in the direction of horizontal extension

and separated by the small circle girdle cone angle (e.g. Gow, 1963; Wakahama, 1974). In laboratory ice deformation experiments, similar levels of flow enhancement are observed for plane strain and unconfined uniaxial compression (e.g. Wilson, 1982; Wilson and Peternell, 2012; Budd et al., 2013). For ESTAR this means E_C has a constant value for both plane strain and unconfined compression. Assuming this equality holds for any combination of normal deformations allows the Budd et al. (2013) flow relation (ESTAR) to be generalised via specification of the ζ-parameter.

Single maximum/cluster-type fabrics

As noted above, strongly clustered vertical single maximum fabrics are routinely observed at depth in polar ice sheets. Contrary to what we interpret as the opinion of reviewer 1, we do not suppose that these fabrics form in response to uniaxial compression at temperatures where the deformation regime is dominated by rotation recrystallisation and recovery by migration recrystallisation is negligible. Where strong single maximum fabrics have been observed in polar ice sheets these can be explained by the contribution of simple shear to the local dynamics – this includes ice-coring sites in central regions of Antarctica and Greenland (e.g. Gow and Williamson, 1976; Russell-Head and Budd, 1979; Azuma and Higashi, 1984; Tison et al., 1994; Gow et al., 1997; Morgan et al., 1997, 1998; Thorsteinsson et al., 1997; Azuma et al., 1999; DiPrinzio et al., 2005; Durand et al., 2007; Montagnat et al., 2012, 2014; Weikusat et al., 2016).

A primary concern when selecting a site to drill an ice core for a palaeoclimate record is that as far as possible it should be dynamically quiescent. Despite this aim it is clear that considerable shear can exist well above bedrock at the dome summit or ridge divide locations chosen for palaeoclimate studies. At drilling sites where there are measurements of borehole inclination to accompany the corresponding fabric data it is apparent that the development of distinct single maxima fabrics is associated with increasing levels of a simple shear deformation in the overall flow regime at depth (e.g. Dahl-Jensen and Gundestrup, 1987; Etheridge, 1989; Morgan et al., 1998; Jansen et al., 2017). No summit/divide is ideal, nor are they necessarily stationary over glacial cycles. Combined, these factors increase the likelihood of encountering single maximum fabrics (and simple shear) at depth at a palaeoclimate coring site. Even at small distances (1-2 ice thicknesses) from an ideal summit, simple shear is present at modest depths and makes a significant contribution to the overall deformation.

In Greenland the GRIP-NGRIP-NEEM ice cores were drilled along a ~ 700 km section of flow line. The coring sites are located nearly equidistant along the flow line, with GRIP at the highest elevation and NEEM furthest along the flow line. For the GRIP, NGRIP and NEEM sites Montagnat et al. (2014) have estimated the depth at which the vertical and simple shear strain rates are equal. Their estimates are 79%, 73% and 65% of the total ice thickness, respectively. As noted by Montagnat et al. (2014), these estimates do not make any allowance for the effect of mechanical anisotropy on enhancing strain rates. It is reasonable to expect that doing so would lead to a proportionally greater increase in the shear strain rates relative to the vertical strain rates. This would shift estimates of the depth where the simple shear and vertical strain rates are equal to lower values, i.e. closer to the ice sheet surface. Results from Law Dome provide some interesting context for these estimates since the simple shear strain rates have been quantified by repeat measurements of borehole inclination at several locations and the vertical strain rate can be estimated by similar methods to those employed by Montagnat et al. (2014). At the Law Dome, Dome Summit South (DSS) site an ice core was drilled 4.7 km (< 4 ice thicknesses) SSW of the dome summit. Here the simple shear and vertical strain rates are equivalent at $\sim 1/2$ the total ice thickness (Morgan et al., 1998; Treverrow et al., 2015), demonstrating that considerable simple shear can develop throughout the depth profile very close to a

dome summit. In accord with the experimental observations of Budd et al. (2013), observations from ice cores reveal there is a progression towards increasingly strong single-maximum fabrics and relatively higher strain rates as the proportion of simple shear within the deformation regime increases (even when the effect of temperature on flow rates is considered, e.g. Etheridge, 1989; Wang and Warner, 1999; Morgan et al., 1997, 1998). These observations are part of the fundamental basis of ESTAR.

Laboratory experiments also demonstrate the formation single maximum fabrics in simple shear (e.g. Bouchez and Duval, 1982; Li and Jacka, 1998; Li et al., 2000; Wilson and Sim, 2002; Budd et al., 2013; Wilson and Peternell, 2012). As described in Schulson and Duval (2009) a two-maxima fabric forms initially during simple shear experiments. The dominant maxima is normal to a plane referred to as the permanent (Bouchez and Duval, 1982) or non-rotating (Budd et al., 2013) shear plane. With increasing strain the second maxima rotates towards the dominant maxima and vanishes (e.g. Bouchez and Duval, 1982).

The only experiments we are aware of which demonstrate that a single maximum fabric can form in response to uniaxial compression have been conducted at very high deviatoric stresses in conjunction with a high confining pressure. Prior et al. (2015) present a diffuse single maximum fabric for a sample deformed in uniaxial compression to a strain of 0.37 with a deviatoric stress of 15 MPa at $-43°$C where the confining pressure was 50 MPa. Similar experiments by Qi et al. (2017) at $-10°$C with 10 MPa confining pressure show that as the deviatoric stress increases from 1.30 MPa to 4.31 MPa the resultant fabric undergoes a transition from a small circle girdle to a diffuse single maximum. This behaviour is attributed to the increased activity of rotation recrystallisation at higher stresses. Importantly, these experiments do not support for the concept of a single maximum forming in response to compression within an ice sheet, since they clearly demonstrate that a small circle girdle is expected for deviatoric normal stresses ≤ 1.30 MPa.

To be clear, we are not suggesting that temperature and stress have no influence on the relative activity of microdeformation and recovery processes occurring within polar ice sheets and the formation of fabric. A detailed comparison of the fabrics encountered in Antarctic and Greenland ice cores and laboratory experiments is beyond the scope of the present response. However, it is worth noting that factors other than stress (both magnitude and configuration) can influence the development of fabric. For example, the presence of soluble and insoluble impurities is related to fluctuations in fabric and grain size over small spatial scales that are observed in ice cores (e.g. Morgan et al., 1997; DiPrinzio et al., 2005).

The series of uniaxial compression experiments of Jacka and Li (2000) provide some insight into the effects of temperature and stress magnitude on the rate at which fabric and strain rates evolve as a function of accumulated strain. Their results suggest that for temperatures below $-15°$C fabrics do not evolve into the distinct small circle girdles that are observed at higher temperatures. For accumulated strains of $\sim 10\%$ (or less) the observed fabrics are weakly anisotropic, displaying a minimal degree evolution from the initially isotropic distribution of c-axis orientations. Unfortunately these fabrics do not provide strong support for the development of either a small circle girdle or single maximum fabric.

Jacka and Li (2000) conducted a single experiment at $-45°$C, that unlike other experiments in the series, was conducted in two stages to allow higher strains to be accumulated (e.g. $> 20\%$, Treverrow et al., 2012). This experiment provides some support for reduced rates of fabric and strain rate evolution at low temperatures and/or stresses. This experiment was incomplete when Jacka and Li (2000) was published, but nevertheless was showing signs of a transition from secondary to tertiary creep (E>1). At the end of the first stage the sample was machined back to a cylindrical shape prior to

recommencing deformation. The experiment was terminated some considerable time after the initial results were published. Analysis of the sample (T.H. Jacka pers. comm) demonstrated that while a weak small circle girdle fabric did eventually form with continued deformation, the strain required for this at $-45\,^\circ$C was higher than the 8-10% observed in the experiments at higher temperatures and stresses.

That lower rates of fabric evolution may be expected at lower temperatures (or stresses) is consistent with the detailed assessment of dynamic recrystallisation within polar ice presented by Faria et al. (2014). They describe how multiple microdeformation and recovery processes are active during microstructural evolution, even in the very cold ice ($T < -20\,^\circ$C) present in the upper regions of the polar ice sheets. Importantly, Faria et al. (2014) note that the relative contribution of these processes to microstructural evolution can vary according to temperature and strain rate.

Since small circle girdle fabrics can form due to uniaxial compression in ice sheets – even if they are not widespread – then allowances must be made for the activity of boundary migration processes at lower temperatures than the suggested threshold values of $\sim -10\,^\circ$C (Duval and Castelnau, 1995) or $\sim -15\,^\circ$C (Schulson and Duval, 2009). Observations from polar firn and ice cores, e.g., Kipfstuhl et al. (2009); Weikusat et al. (2009b,a) reveal microstructural features which clearly demonstrate that internal strain energy is sufficient to allow dynamic recrystallisation processes, including strain-induced boundary migration, to contribute to microstructural evolution at temperatures below $-20\,^\circ$C. Modelling of the microstructural evolution of firn (Steinbach et al., 2016) demonstrates the crucial role of air bubbles in the development of the strain localisation and strain energies that are sufficient to drive dynamic recrystallisation at low temperatures in firn.

The point of the preceding discussion is to demonstrate that tertiary creep and the development of polycrystalline anisotropy is associated with the formation of a statistically steady state microstructure (including fabric) that persists under stable conditions of temperature and stress. Kipfstuhl et al. (2009) and Faria et al. (2014) demonstrate that tertiary creep cannot be simply defined according to activity (or otherwise) boundary migration. Consequently it is incorrect to invoke this single specific microdeformation process as the determinant of fabric variations observed with depth (or temperature) in ice sheets. Kipfstuhl et al. (2009) demonstrate that strain-induced boundary migration is active below the threshold temperatures proposed by Schulson and Duval (2009).

Regarding the issue of just how widespread tertiary creep is within polar ice sheets, Faria et al. (2014) describe (with specific reference to the EDML site) how the densification of firn, driven by a reduction in pore space, must be accommodated by ice deformation. Total accumulated strains within firn are high enough to support the conclusion that tertiary creep is occurring there. Faria et al. (2014) describe how the occurrence of tertiary creep, without the development of a corresponding pattern of preferred c-axis orientations is due to the complex geometry of the pore space in the two-phase ice-air system which produces localised heterogeneity in the stresses driving deformation. Thus, any localised development of preferred c-axis orientations would be masked by the spatial variability in local stress and strain.

There are some counter-intuitive aspects to the argument for single maximum fabrics forming in response to compression. Firstly, for deformation largely accommodated by basal slip, the effective viscosity will continually increase if a single maximum evolves in response to compression. Consequently high levels of deformation would have to be accommodated by non-basal processes. Secondly, if a single maximum forms in compression due to the inactivity of migration recrystallisation, then it is hard to see why single maximum fabrics become stronger with increasing depth in an ice sheet where the ice is is also warmer. If a single maximum did form in an ice sheet due to compression, as the

ice becomes warmer we should see a transition to a cone-type fabric, since the activity of migration recrystallisation would be increased. The problem is that we don't see such a progression in fabrics.

The multiple maxima fabrics observed in zones closest to bed in an ice sheet don't provide the answer here, since they are not the same as the cone-type small circle girdle fabrics associated with uniaxial compression. Multiple maxima fabrics form due to the high activity of migration recrystallisation in temperate ice. In polar ice sheets this often corresponds to warm ice near the bed that has undergone a stress relaxation due to the effect of underlying bedrock topography on disrupting the large-scale flow. The high levels of strain energy in relatively warm ice can drive migration recrystallisation. The existence of a topographic disturbance to the flow can be deduced from horizontal velocity profiles obtained from borehole inclination measurements. The inflection in these profiles close to the bed is consistent with boundary layer flows where there is an adverse pressure gradient, i.e. the reduction in velocity close to the stationary surface (the bed) exceeds expectations associated with either a neutral or favourable pressure gradient.

We now return to the latter part of the reviewer's comment about textures and tertiary creep, which we repeat for convenience:

R1: Textures resulting from migration recrystallization are indeed stress-configuration depend and the argument that the microstructure evolves more rapidly than the flow configuration sufficiently robust to assume a scalar isotropic relationship in the context of large scale ice flow modelling. In the central part of the ice-sheets, temperature and strain energy can be too low to initiate migration recrystallization and there is no evidence that it occurs except in the warm ice near the bed (the last 100-200 meters usually). See texture measurements in all deep ice cores in the central regions of Greenland and Antarctica. There is a general agreement that in the regions of normal grain growth and rotation recrystallization (most of the ice thickness in the central regions) basically develops as the results of lattice rotation due to intractrystalline slip; and thus reflect the deformation history.

We agree with the reviewer that all development of anisotropic fabric reflects the deformation history, more particularly, the recent deformation history. It is certainly true that within the lowest $100 - 200$ m warm ice, high levels of strain energy and stress relaxation due to the effect of underlying bedrock topography on disrupting the large-scale flow can lead to significant migration recrystallisation and formation of multiple-maxima fabrics. The topographic disturbance to the flow can be deduced from horizontal velocity profiles obtained from borehole inclination measurements. Such profiles are consistent with flows where an adverse pressure gradient exists. However, as discussed above, it is incorrect to suggest that there is 'general agreement' on a depth-progression of specific zones of normal grain growth and rotation recrystallisation etc throughout an ice sheet. A more up-to-date review on microdeformation in ice sheets is provided by Faria et al. (2014). The observations of Kipfstuhl et al. (2009); Weikusat et al. (2009a,b) demonstrate that strain energy sufficient to drive strain-induced boundary migration occurs throughout ice sheets, including firn layers. This view is also supported by the numerical simulations of Steinbach et al. (2016).

R1: The combination of anisotropic textures and the high mechanical anisotropy of the ice mono-crystal makes the ice polycrystal highly anisotropic. This has been confirmed by laboratory experiments that have shown that the strain-rates for secondary creep of polycrystalline ice depends on the fabric and its orientation with respect to the test configuration; while the tertiary creep is independent of the initial fabric and depends only on the test configuration.

Yes, this final point is precisely the basic tenet of our theory, but only because the stress configu-

ration has been applied for long enough to achieve the tertiary state. Tertiary creep of polycrystalline ice is dependent upon the stress configuration and whether or not it is occurring is not simply a matter of the activity of migration recrystallisation.

R1: All the studies presented in Sec. 2.1 as 'microstructure approaches', where motivated by representing the mechanical anisotropy of polycrystalline ice that develops as a result of the development of strain-induced preferred orientations of the ice crystals. They can not be opposed or compared to the flow law presented here, as they don't represent the same physical processes.

We disagree with the reviewer. What all flow relations aim to do is represent the bulk deformation of a polycrystalline aggregate. Microstructure based flow relations, where fabric is an input, can be applied equally to predictions of secondary or tertiary creep, or by extension to any arbitrary combination of stress and fabric. ESTAR only claims to represent tertiary creep – a subset of the cases that can be compared with microstructure based flow relations. Consequently comparisons with microstructure based approaches are entirely valid provided that the appropriate combinations of fabric and stress/deformations are considered. Laboratory experiments and ice cores for which corresponding strain rate data are available from repeat measurements of the borehole inclination are valuable sources of data that can be applied in such comparisons. This is particularly true for laboratory measurements of tertiary creep since the applied stresses, strain rates and microstructure data are all available.

R1: Laboratory experiments for tertiary creep are certainly relevant for the regions where migration recrystallization occurs; i.e. in temperate glaciers, in the bottom part of the central regions of the ice-sheets and certainly in the margins where temperature and stresses are sufficiently high. These areas are potentially important for the flow dynamics of polar ice sheets. The flow law presented in this paper must be presented in this perspective, and not as an empirical approach to represent the strain-induced mechanical anisotropy that results from the development of ice fabrics as seen in all deep ice-cores. This implies to largely rewrite large parts of the abstract, introduction and second section, to discuss the validity of the assumptions of the flow law and their domain of applicability for large-scale ice flow modelling.

Based on the preceding discussion, we do contend that ESTAR is a legitimate '...empirical approach to represent the strain-induced mechanical anisotropy that results from the development of ice fabric'. We have slightly modified the manuscript to more clearly highlight the 'domain of applicability' of ESTAR (P4L31-P5L18):

> "A second approach comprising experimental and observational approaches (Li et al., 1996; Wang et al., 2002a,b), modelling (Wang and Warner, 1998, 1999; Hulbe et al., 2003; Wang et al., 2003, 2004; Breuer et al., 2006; Wang et al., 2012), and theoretical studies (Warner et al., 1999), has focussed on the development and assessment of an anisotropic flow relation for polycrystalline ice in which the nature of the crystal fabric and the magnitude of strain rate enhancement, E, are both regarded as determined by the stress regime. This assumption is supported by experimental observations for pure polycrystalline ice, which demonstrate that an accumulated strain of $\sim 10\%$ is required for the microstructure to evolve to a state that is compatible with the flow configuration, irrespective of its initial condition (Jacka and Maccagnan, 1984; Gao and Jacka, 1987; Li and Jacka, 1998; Treverrow et al., 2012). Specifically, this approach regards the fabric and the enhancement in tertiary flow as determined by the relative proportions of the simple shear and normal deviatoric stresses. For such flow relations, it is typically assumed that the spatial variation in dynamic conditions (e.g., flow configuration and temperature) only occur gradually in an ice sheet, so that the microstructure evolves to maintain compatibility

with these conditions. Through most of an ice sheet we expect that the rate of microstructural evolution generally exceeds the rate at which the flow configuration varies, and that the distances travelled by a parcel of ice during the time taken to develop a compatible fabric are typically small compared to the relevant ice sheet spatial scales.

The anisotropic flow relation proposed by Budd et al. (2013) represents a continuation of this strand. They found that a scalar anisotropic flow relation, i.e., one maintaining the collinear relationship between the components of $\vec{\dot{\varepsilon}}$ and $\vec{\sigma'}$ (τ_e is a scalar function of the second invariant of $\vec{\sigma'}$) provides a good fit to laboratory data from combined compression and shear experiments. Such a scalar anisotropic rheology also simplifies the requirements for implementation within ice sheet models that are already compatible with the (scalar) Glen rheological description. Budd et al. (2013) proposed what we term ESTAR as a suitable candidate scalar anisotropic rheology generalised to arbitrary stress configurations (i.e., not restricted in its application to the limited set of experimental stress configurations described in Li et al. (1996) and Budd et al. (2013))."

Rewriting 'large parts of the abstract, introduction and second section' is not required. It is important to bear in mind that this is a paper about the implementation of a flow relation, not its formulation (P3L12-17).

Point 3:

Application to the embayed ice shelf
R1: I think it would have been more interesting to test the model with larger transverse dimensions, i.e. to represent non-embayed ice-shelves, as I assume that simple shear along the margin will be less important and the difference with Glen and a uniform enhancement factor for shear should increase?

As mentioned in the manuscript (P11L17-22) we have carried out the embayed ice shelf experiment for the cases where the transverse dimensions are $L \in [20, 60, 100]$ km. Figures 1-3 below show the ESTAR to Glen velocity ratio, ESTAR to Glen thickness ratio, and λ_S for each of the three cases. Note that the figures are plotted to approximately preserve their aspect ratio. It is clear from these figures that as the real aspect ratio increases, the ice shelves become flatter, so the proportion of the ice shelf that is shear dominated does not change markedly. Specifically, approximately 60% of the $L = 20$ km ice shelf is shear dominated (i.e., $\lambda_S > 0.5$), 63% of the $L = 60$ km ice shelf is shear dominated, and 67% of the $L = 100$ km ice shelf is shear dominated. This is an important result, demonstrating that, contrary to the reviewer's expectations, changing the aspect ratio does not result in an embayed ice shelf that approaches the unembayed situation (i.e., with free-slip at the side walls).

Furthermore, regardless of aspect ratio the pattern and magnitude of the velocity ratios is similar in all cases, the maximum difference being approximately 15% near the ice-ocean front where normal stresses dominate.

Hence, given the similarities in the influence of the rheology on the dynamics between the aspect ratios, we prefer to focus our discussion in the manuscript on only one transverse dimension, $L = 20$ km. We have updated the manuscript to be more explicit about the consequences of increasing the aspect ratios, as per P11L17-22:

"The experiment was carried out for model domains with transverse spans $x \in [0, L]$, for $L = 20$, 60, and 100 km and along-flow dimension $y \in [0, 100]$ km. The initial ice thickness decreases uniformly from 1000 m at the grounded zone to 300, 600, and 850 m at the ice front for the $L = 20$, 60, and 100 km cases, respectively. The main features of the anisotropic effects are similar regardless of aspect ratio. This is principally because wider embayed ice shelves are flatter so that the influence of simple shear stresses on the dynamics is not particularly sensitive
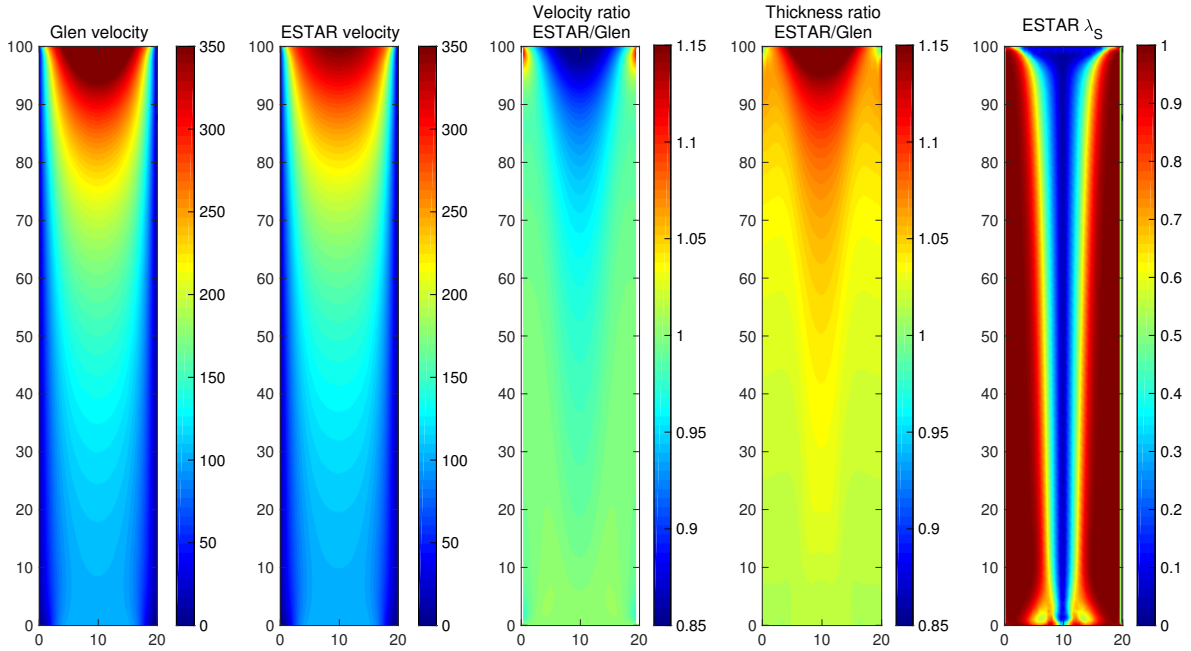
Figure 1: HO steady-state surface fields for the embayed ice shelf with transverse dimension $L = 20$ km. From left: ratio of ESTAR/Glen velocity ($E_G = 8$); ESTAR λ_S; Glen thickness ($E_G = 8$; m); ESTAR thickness (m); ratio of ESTAR/Glen thickness.

to aspect ratio. Accordingly, we focus our discussion on one transverse length scale: $L = 20$ km."
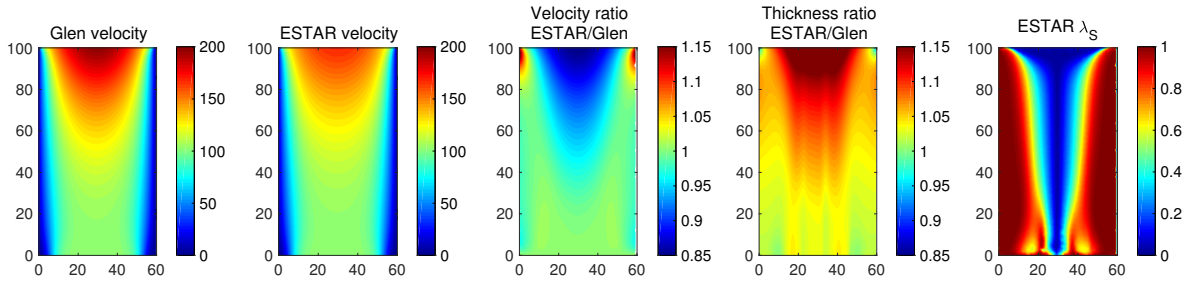
Figure 2: HO steady-state surface fields for the embayed ice shelf with transverse dimension $L = 60$ km. From left: ratio of ESTAR/Glen velocity ($E_G = 8$); ESTAR λ_S; Glen thickness ($E_G = 8$; m); ESTAR thickness (m); ratio of ESTAR/Glen thickness.
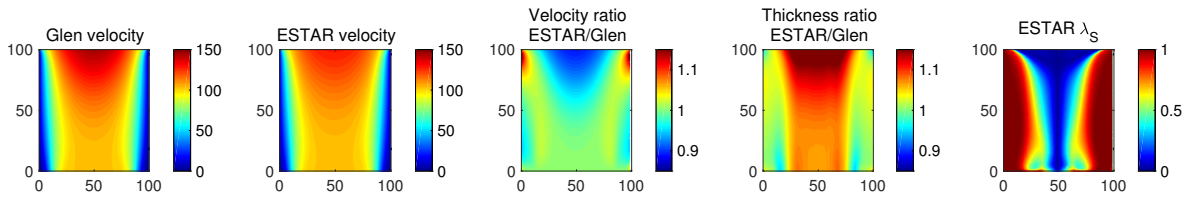

Figure 3: HO steady-state surface fields for the embayed ice shelf with transverse dimension $L = 100$ km. From left: ratio of ESTAR/Glen velocity ($E_G = 8$); ESTAR λ_S; Glen thickness ($E_G = 8$; m); ESTAR thickness (m); ratio of ESTAR/Glen thickness.

Point 4:

ISMIP-HOM experiments

R1: When discussing the results for Glen in the main text it is never clear for which value of the enhancement factor. The fact that the velocity scales with the enhancement factor is not a result, but as written in the manuscript follows from the definition of the experiment. So it would be more clear for the reader, to discuss the results for only one value of the enhancement factor or maybe better, find the value of the Glen enhancement factor that minimize the velocity difference with the tertiary creep flow law, and discuss this value and the results for this value.

The ISMIP-HOM experiments are scenarios in which the bed-parallel shear is the main driver of the flow. Hence, it emerges as appropriate that we choose a value for the Glen enhancement factor equal to the shear enhancement factor, i.e., $E_G = E_S = 8$. Accordingly, we have adopted the reviewer's first suggestion and have deleted the paragraph from the manuscript that compares the results for different values of E_G. Since in response to Reviewer 2 we have introduced additional experiments (see details later), and as an interested observer would recognise the overall scaling properties, we have not considered it useful to take up the alternative suggestion of fine-tuning E_G for each experiment. On P13L23-25 of the manuscript for ISMIPB, we clarify that our discussion of the results concentrates on the value $E_G = 8$, which is the most appropriate overall choice for this experiment:

"In what follows, we consider the case when the Glen enhancement factor is equal to the ESTAR shear enhancement factor, i.e., $E_G = E_S = 8$. This is the most relevant case for the ISMIPB experiment as the dynamics here are driven by bed-parallel shear, as discussed below."

For ISMIPD, we include the following lines, echoing the above lines regarding ISMIPB that here we compare only the results from the case when $E_G = E_S = 8$ (P15L17-19):

"Consistent with ISMIPB, the control of the final deformation flow in the ISMIPD experiment is bed-parallel shear, so we consider the case when the Glen enhancement factor is equal to the ESTAR shear enhancement factor, i.e., $E_G = E_S = 8$."

R1: The discussion in page 12 about the value of the shear fraction along the transition curve is not very clear.

We have amended the discussion about the shear fraction along the transition curve on P14L23-P15L5 to be clearer, as follows:

"In order to examine the dynamics giving rise to the high shear-dominance peaks in Fig. 6d and Fig. 7d, we consider the following exact form of λ_S^2 (for these two-dimensional flow fields) expressible using the cartesian frame strain rate components

$$\lambda_S^2 = \frac{\alpha \dot{\varepsilon}_{xx}^2 + \beta \dot{\varepsilon}_{xz}^2 + \gamma \dot{\varepsilon}_{xx} \dot{\varepsilon}_{xz}}{\dot{\varepsilon}_{xx}^2 + \dot{\varepsilon}_{xz}^2}, \tag{23}$$

for some spatially varying coefficients α, β, and γ. Since there is no surface accumulation, velocities and hence local non-rotating shear planes at the ice sheet surface are parallel to the surface. The traction free surface boundary condition implies that the numerator ($\dot{\varepsilon}'^2$) in Eq. 23, and accordingly λ_S, vanishes at the surface, except that if $\dot{\varepsilon}_e$ also vanishes, λ_S is technically undefined. Our implementation sets $\lambda_S = 0$ for vanishing $\dot{\varepsilon}'$ in such situations. It is apparent from Eq. 23 that along the transition curves, i.e., where $\dot{\varepsilon}_{xx} = \dot{\varepsilon}_{zz} = 0$, $\lambda_S^2 = \beta$, independent of (non-zero) $\dot{\varepsilon}_{xz}$ strain rate. One can show that $\beta \to (1 - S_x^2)^2$ towards the surface (i.e., for surface slope in the x-direction S_x) along the transition curve, in order to satisfy the surface

14

boundary condition. This indicates that λ_S would be finite along the transition curves all the way to the surface, except that we enforced its vanishing there. For these locations, the Glen and ESTAR viscosities corresponding to Eqs. 2-3 would tend to infinity as $\dot{\varepsilon}_e$ vanished approaching the surface, but are limited to a maximum value in the ISSM implementation.

Note that away from the transition curves λ_S goes to zero as we approach the surface, associated with vanishing shear on the non-rotating shear plane and the corresponding dominance of normal deformations. We return to these near-surface spikes in λ_S in the discussion."

REVIEWER 2

Point 1:

Anisotropy

R2: I have had a chance to look at the other reviewer comments and I have to say that I fully agree with him/her in the main two points of his/her review. First, the authors always refer to the method as "anisotropic", it is the "A" in the acronym. That is not simply misleading, it is wrong. In an isotropic rheology the relation between stress and strain-rate is a scalar number, twice the viscosity, in a more general anisotropic rheology it is a tensor. The method presented in the paper is simply not anisotropic.

The question of the anisotropic nature of ESTAR has already been addressed in our response to Reviewer 1. ESTAR is an anisotropic flow relation. The fact that ESTAR describes the rheology of anisotropic polycrystalline ice via a scalar enhancement factor does not preclude it from being an anisotropic flow relation. Reviewer 2 is incorrect in claiming that a scalar (collinear) relationship between the stress and strain rate tensor components is a necessary feature of an isotropic flow relation and that a tensor relationship between the stress and strain rate tensors is a necessary condition for an anisotropic rheological description. This issue has been addressed previously in the literature (Placidi et al., 2010).

The Continuum-mechanical, Anisotropic Flow model, based on an anisotropic Flow Enhancement factor (CAFFE) (Placidi et al., 2010) is an anisotropic flow relation that features an enhancement factor that is scalar function of a deformability parameter that is defined in terms the fabric and stress field. Faria (2008) provides a derivation of the anisotropy of CAFFE and Section 4 of (Placidi et al., 2010) provides further verification of its anisotropy, despite its collinear nature. Conceptually the same arguments apply to ESTAR, since it also features collinearity of the stress and strain rate tensors and a scalar enhancement that is an anisotropic function of the stress configuration.

As discussed in the response to Reviewer 1, the required ('tertiary') compatibility of the anisotropy with the stresses prevents any idea that stress can be rotated relative to the anisotropic material as the reviewer implies – this is the essence of anisotropy.

R2: Also in this point, the authors refer to Glen flow relation vs ESTAR throughout the manuscript. ESTAR as far as I can see is a Glen flow relation with a pre-exponential factor that varies spatially to account for ice fabric. A in Equation 1 is known to depend on ice fabric and a myriad of other things (not only on temperature as stated in the manuscript), the whole point of ESTAR is that it is giving a method to estimate the effect of ice fabric on A.

One could regard the ESTAR flow relation as it is presented, as a fabric-dependent enhancement factor for the Glen flow relation in tertiary flow. We regard this as essentially a semantic point since the task of implementing this factor is identical regardless of the viewpoint, and the enhancement function would still need a name that would encompass, empirical, tertiary and anisotropic. In terms of tertiary flow, it is not entirely certain (e.g. Treverrow et al., 2012) that tertiary flow does only differ from the Glen relation by this pre-factor. Regarding the "myriad of other things" known to influence A in addition to temperature, we contend that these are usually persistent material properties, like dissolved or particulate impurities, rather than dynamically evolving features such as crystal anisotropy. We now make this distinction more clearly in the manuscript, as per P2L18-20:

"$A(T')$ is a flow parameter ($\mathrm{Pa}^{-n}\,\mathrm{s}^{-1}$), dependent on homologous temperature T' and persistent material properties, for which various parameterisations exist based on laboratory tests and field measurements (e.g., Budd and Jacka, 1989; Cuffey and Paterson, 2010)."

Point 2:

Tertiary creep

R2: And second, the empirical relation to extract the enhancement factor is based on laboratory experiments of tertiary flow, and it may well be that it can not reproduce the widespread observations of strain-induced anisotropy in polar ice. There is no discussion in the paper about how the proposed method explain observations or even expectations of the effect of ice fabric in polar flow. Do the vertical or horizontal variations of enhancement factor make sense according to observations of fabric or strain-rate fields?

The aim of this paper is to describe the numerical implementation of a flow relation or ice rheology within an ice sheet model (P3L12-17). While ESTAR is not directly concerned with determining strain-induced anisotropy, there is a connection through the empirical observation that the flow-induced anisotropy is connected to the stress regime, so incorporation of ESTAR into an ice dynamics model is clearly an essential step in testing whether this can *"reproduce the widespread observations of strain-induced anisotropy in polar ice"*.

This flow relation, ESTAR, has been previously described (Budd et al., 2013) and its performance evaluated using ice core, borehole and laboratory data (Treverrow et al., 2015). It is outside the scope of this paper to present a comprehensive review of how ESTAR *"explain(s) observations or even expectations of the effect of ice fabric in polar flow"*, or to provide an even more general review on the effects of polycrystalline anisotropy on polar ice sheet dynamics. The background to ESTAR is described in Sects. 2.2-2.3. It is important to realise that implementation of ESTAR (or any other rheological description) in an ice sheet model provides an additional quantitative means by which that flow relation can be further tested and subsequently applied in simulating ice sheet dynamics. Regarding the validity of the assumption that tertiary creep is the predominant mechanism of deformation in the dynamically active region of polar ice sheets, we refer the reviewer to preceding comments in this response document. We also slightly modify the sections from the previous manuscript detailing conditions under which we expect ESTAR to be valid (P4L31-P5L18; quoted directly in the response to Reviewer 1 above), and provide new paragraphs discussing regions where it might not hold (P5L21-P6L12; again, quoted directly in the response to Reviewer 1 above).

In response to the last item above:

R2: Do the vertical or horizontal variations of enhancement factor make sense according to observations of fabric or strain-rate fields?

We refer the reviewer to Treverrow et al. (2012) and Budd et al. (2013) and references therein for a detailed discussion on the variation in strain rate enhancement according to the stress configuration. Wang and Warner (1999), Wang et al. (2002a), and Treverrow et al. (2015) each discuss the vertical variations in enhancement that are required to explain observed strain rate profiles within an ice sheet and also present fabric profile information.

Point 3:

ESTAR vs tuning hardness parameter

R2: I also miss an important point in the paper, what is the point of using ESTAR in a large-scale ice sheet model?

We have interpreted this question as 'what is the point of using any anisotropic flow relation in any large-scale ice sheet model?'.

There has long been recognition that a flow relation that realistically incorporates the anisotropic

rheology of polycrystalline ice is a necessary component of any ice sheet model. While a diverse range of anisotropic flow relations have been proposed, implementing such a relation within an ice sheet model in computationally efficient manner has proven challenging. Additionally, there has been a long standing awareness that using a Glen-type flow relation with a spatially-invariant enhancement factor does not provide an adequate description of polycrystalline ice rheology. What we are presenting is our attempt at incorporating a description of anisotropic rheology into an ice sheet model (P3L12-17).

R2: I may be missing something here but large-scale models are capable to initialize the local depth-averaged hardness parameter in the Glen flow law using satellite observations. What is ESTAR adding?

While it is possible to "tune" a "local depth-averaged hardness parameter" as well as a basal friction parameter using inverse methods to match modelled and observed surface velocities, such an approach provides no physical insight into the local controls on deformation rates and no indication how the "depth-averaged hardness" should change as the ice sheet evolves (note, we also do not want to invert for both ice rheology parameters and basal friction, as there would be an infinite number of solutions – they have "similar" effects on the surface velocities. This is why we only invert for B on floating ice, and friction on grounded ice, but never both at the same place). ESTAR is adding the ability to incorporate the spatial variability of large-scale anisotropy within ice sheets into simulations of ice sheet evolution, with a physical basis, in a fashion that will remain valid as the system evolves. It would be possible to explore using inverse methods to find appropriate global values for E_C and E_S, since ESTAR describes the spatial variations, encoded in λ_S, e.g. (P19L32-34):

> "Indeed, with the implementation of ESTAR in ISSM, it might be possible to use inverse methods to search for values of E_S and E_C that improved the match between modelled and observed surface velocities."

However, there is clearly too little data in a 2D surface velocity field to determine a 3D varying "hardness parameter" throughout an ice sheet.

R2: Could ESTAR inform the initialization of a large-scale model somehow? It could be applied to simulations were there is no satellite observations but then, as I suggested in my previous point, shouldn't we check how well does it do in a case where we have observations? Also, are there any significant vertical variations on enhancement factors that are captured by ESTAR but can't be inverted by a large-scale model? In any case, the paper needs be clearer about what is ESTAR and what can it do.

The purpose of implementing and testing ESTAR in a large-scale ice sheet model is to explore what advantages it offers. We have shown that it is a computationally-efficient, physically based description of anisotropic flow (Sects. 5-7). We are reluctant to further expand Section 2.3 about the theory underlying ESTAR, as this paper is about the implementation of a flow relation that has already been discussed at length by Budd et al. (2013). In this manuscript, we have explained the implementation and explored what ESTAR can do in some preliminary test examples; its implementation is a necessary precursor to testing it in other more realistic situations, including the reviewer's suggestion to "check how well it does". Indeed, we are currently applying ESTAR to an Antarctic glacier system where observations are available to validate our simulations and these are forthcoming. However, it is outside the scope of this current manuscript to include full simulations of real glaciers.

As already discussed, large-scale models are capable of initialising the "local depth-averaged hardness parameter" in the Glen flow relation (relying, of course, on also tuning of the basal traction

parameter over grounded ice) using satellite observations. However, this sort of initialisation, without physical insights into the processes controlling the tuned parameter, is problematic. As the system evolves, the various physical processes that a "black box" parameter represents may change, rendering the "initialisation" values inappropriate. ESTAR could potentially inform the initialisation of an ice sheet model, through determining appropriate global values of enhancement factors E_S and E_C, using the physics embodied in ESTAR through λ_S to include spatial variations in 3D (P19L32-34). Indeed, in our ice shelf example, an essentially 2D flow problem in the absence of temperature effects, one could attempt to invert for the values of E_S and E_C to see if this improved agreement between modelled and observed velocities. However, the enhancement factor in ESTAR is not physically or dynamically equivalent to the overall flow parameter in the Glen flow relation. Furthermore, in this study, we have used the full-Stokes 3D implementation of ESTAR, which relies on more than just depth-averaged parameters. Indeed, there is insufficient data in satellite-derived surface velocities to derive a local, 3D ice flow parameter.

R2: Also, are there any significant vertical variations on enhancement factors that are captured by ESTAR but can't be inverted by a large-scale model? In any case, the paper needs be clearer about what is ESTAR and what can it do.

Wang et al. (2002a) demonstrate the need for a significant vertical variation in enhancement factor – simply derived from observations – together with a convincing connection to both an ESTAR-type prescription that yields that depth variation, and to the anisotropic crystal orientation fabrics observed. Treverrow et al. (2015) continues this study by exploring how ESTAR compares with other candidate flow relations. Both these studies advocate the need for a depth dependent enhancement factor, though in the general context of an assumed driving stress. This further drives the motivation for implementing ESTAR in an ice dynamics model that can solve for the full stress field to extend the testing of ESTAR against observations.

Point 4:

Aspect ratios

R2: Finally, I find really intriguing that the authors state that results are very similar with different aspect ratios in the experiments presented in Sections 5.1 (P9-L31) and 5.2 (P11-L25). What do they mean? In the embayed ice-shelf, I would expect the ice fabric induced by extension and shear at the margins to be different. The narrower the ice-shelf is I would expect that the overall effect of lateral shearing should be more important. In the ice flow over a bumpy bed, L is the wavelength of the bedrock undulations. I would expect the increase in basal roughness to have a strong control over the orientation of the fabric. What does it mean that aspect ratios don't affect ESTAR results? I would like to see some discussion about the results presented.

For the embayed ice shelf, as discussed above in response to reviewer 1, we have focussed our discussion in the manuscript on the case when the transverse dimension is $L = 20$ km. Figures 1-3 in this document show the Glen and ESTAR steady-state surface velocity ratio, the Glen to ESTAR thickness ratio, and λ_S, for the cases when the transverse dimensions are $L \in [20, 60, 100]$ km, respectively. The key point highlighted in these figures is that as the aspect ratio increases, the ice shelves become flatter, and the overall proportion of the ice shelf that is shear dominated does not change markedly (so the embayed ice shelf does not approach the unembayed situation). Hence, and in the interests of constraining the length of the manuscript, we have omitted the results of the cases when $L = 60$ and 100 km. We have amended the manuscript to be clearer on the impact of increasing aspect ratio, as

highlighted on P11L17-22:

> "The experiment was carried out for model domains with transverse spans $x \in [0, L]$, for $L = 20$, 60, and 100 km and along-flow dimension $y \in [0, 100]$ km. The initial ice thickness decreases uniformly from 1000 m at the grounded zone to 300, 600, and 850 m at the ice front for the $L = 20$, 60, and 100 km cases, respectively. The main features of the anisotropic effects are similar regardless of aspect ratio. This is principally because wider embayed ice shelves are flatter so that the influence of simple shear stresses on the dynamics is not particularly sensitive to aspect ratio. Accordingly, we focus our discussion on one transverse length scale: $L = 20$ km."

Regarding the ISMIP-HOM experiments (Sects. 5.2 and 5.3), we wish to thank the reviewer for encouraging us to explore more deeply the cases of bed variations with shorter wavelengths. We did observe greater variations in the anisotropic case, and we have also developed a more extensive discussion of the results (Sect. 6). The analysis also provides some indications of regions where the assumptions of the ESTAR rheology may not hold and this is now addressed in the discussion (Sect. 6), though the consequences of that type of lapse in realistic ice sheets requires further study.

Given that ESTAR does not directly calculate crystal orientations our interpretations do not directly address the reviewer's interest in fabrics, though we do provide some interpretations in the discussion (P17L31-P19L22):

> "Our idealised test cases also provide some insights into the validity of the tertiary flow assumption underlying ESTAR, and the development of anisotropic crystal fabrics compatible with the current deformation regime. In the embayed ice shelf test the most significant change in the deformation regime is clearly the transition to extensive flow on approach to the ice shelf front. The contours of λ_S here are relatively well aligned with the ice flow so that flowing ice experiences gradual changes in stress regime, and the magnitudes of strain rates (e.g., Fig. 4b) and velocities (Fig. 3) indicate that in the region near the ice front, where the Glen and ESTAR results vary appreciably, a progression of essentially compatible fabrics would be maintained. Indeed, under the prevailing deformation and flow conditions these would even develop from random fabrics over a few km.
>
> The ISMIP-HOM experiments reveal potential violations of the tertiary flow assumption, although the significance for the flow field of these apparent short-comings needs to be assessed with regard to the somewhat artificial nature of the tests. Indeed as we saw, the difference between the ESTAR predictions and the Glen flow relations (provided $E_G = E_S$) was small, except for ISMIPB with $L = 5$ km, although of course ESTAR makes no claim to correctly describe the transient rheology of ice with an evolving anisotropy.
>
> The ISMIP experiments have a spatial periodicity, which could allow one portion of the repetitive basal conditions to dominate the overall flow. Also, there is no surface mass budget in these experiments so that, as remarked earlier, the ice surface is a flow line, whereas in a system with surface accumulation fresh snow is always being added and advected down into the ice sheet where it makes the transition to solid ice. Accordingly, in the flow regime of these prognostic experiments even the surface layers would be regarded as having developed some anisotropy just as the lower layers would, since they have in principle been deforming over an arbitrarily long time.
>
> The main issue about the establishment of tertiary flow conditions in the periodic environment of our ISMIP experiments concerns the possible cycling of the flowing ice through a variety of stress regimes. This leads to transition regions where the stress regime and presumably the crystal anisotropy would be evolving, and the compatibility assumptions behind ESTAR could

20

locally be violated. Clearly the spatial extent of transitional flow and the delay in attaining any new tertiary state depends on the magnitudes of the strain rates and the velocity of the ice. By combining these with a threshold for accumulated strain as the criterion for development of a compatible (tertiary) fabric under a persistent flow regime, the extent of a transition zone can be estimated. This scale can then be compared to the horizontal variation of the stress regime. Selecting the 10% strain required to develop a compatible anisotropy from initially randomly oriented ice should provide a conservative yardstick, when applied to gradual changes in stress regime.

The patterns of stress regimes revealed by the distributions of λ_S (Figs. 6d, 7d, 9a, and 10f) indicate where along-flow variations in stress regime might be too rapid to sustain the assumption that a compatible crystallographic anisotropy had evolved. For the ISMIPB experiments this concern is essentially focussed to the near surface spikes in λ_S around the two locations where longitudinal deformations vanish, since the anisotropy of deeper ice will be compatible with deformation dominated by simple shear. There may be some complications with a slow cycling of the upper levels between extensive and compressive flow. Very near the surface, the λ_S peak intervals are narrow and the shear strain rates there are very small (corresponding to transition scales of several kilometres) so that there will be no appreciable development of a shear compatible fabric. Either side of the peaks, the main extensive and compressive flow domains for $L = 20$ km (see Fig. 6e) are ≈ 5 km long and have transition scales of < 1 km which suggests that the strongly normal stress dominated upper layer will be mainly in tertiary state. Turning to the transient shear intrusions into this layer: at 100 m depth over the bump the shear transition scale is 3 km while at 200 m depth over the depression the shear transition scale is ≈ 5 km, suggesting that that the λ_S peaks do represent a local failure of ESTAR's tertiary assumption. Throughout the domain the lower half of the ice column has transition scales of ≤ 300 m which, given the gradual variations in λ_S and the direction of ice flow, indicates that region is in the tertiary state.

For ISMIPB with $L = 5$ km, which displays a generally deeper band of normal stress dominated regime (Fig. 7d), the transition scales for the compressive and extensive regions are ~ 500 m for regions of ≈ 1 km in extent, while the shear transition scales at 100 m depth above the bump and 200 m depth above the depression are now ~ 10 km and ~ 1 km, respectively. For most of the domain the transition rates in the lower half of the ice column are ≤ 100 m, although this rises to nearly 1000 m above the bedrock bump.

In the ISMIPD case, for $L = 20$ km, the pattern of λ_S (Fig. 9a) shows there are also transitions between simple shear dominated and extension dominated deformation associated with the slippery region, with varying abruptness at different depths, and some of the contours of λ_S in this instance almost orthogonal to the ice flow. A complication is that there is very little longitudinal deformation (Fig. 9e) occurring over the slippery region because the overall flow is controlled by the periodic sticky spot. Accordingly, there would not be any significant fabric evolution across this ~ 4 km region (estimated transition scales there are > 40 km) so that the tertiary assumption and using E_C (since $\lambda_S = 1$) would be inappropriate. Once again, the low strain rates here (Figs. 9e-f) translate into very stiff ice and might make the influence of ESTAR enhancement factors relatively unimportant. A factor of 100 in $\dot{\varepsilon}_e$ changes viscosity by a factor of 21.5, whereas the maximum viscosity contrast from $E(\lambda_S)$ is 1.39. The shear strain rates are also very low, with transition scales > 1 km except very close to the bed over the sticky spot. Accordingly, while a compatible fabric could be expected where the large λ_S

values are shown in Fig. 6a, its presence would be due to the periodic flow, and the inability of the $\lambda_S \sim 0$ region to modify it.

For the last test, ISMIPD with $L = 5$ km, strain-rates are once again very low, and there is no simple structure to the picture of the stress regime portrayed by λ_S in Fig. 10f. Below mid-depth there is a periodically continuous band of shear that might favour the development of crystal anisotropy, but clearly the tertiary flow assumption of ESTAR would not be particularly useful here."

For the ISMIP-HOM experiments with larger horizontal extents (i.e., $L > 20$ km), the extent to which the longitudinal stresses impact flow and the differences between ESTAR and Glen results both decrease as L increases, such that the dominant sensitivity of the flow to the bed aspect ratio is similar for both rheologies. This is generally consistent with the results concerning the longitudinal stresses presented by Pattyn et al. (2008), allowing for the fact that our simulations have evolved to steady-state whereas those tests were to find flows satisfying initial stress balance. By contrast, for smaller horizontal extents (e.g., $L = 5$ km), the increasing importance of longitudinal stresses leads to greater differences between Glen and ESTAR experiments. We overview the expanded ISMIPB and ISMIPD results in turn.

In ISMIPB the more rapid bed variation shows greater reductions in ESTAR velocities (stiffer ice) and higher spatial contrast in the velocity ratios. This is evident when comparing the $L = 5$ km results in new Fig. 4 below (Fig. 7 from the updated manuscript) with the case when $L = 20$ km in Fig. 6 from the updated manuscript. The smaller aspect ratio ($L = 5$ km) leads to a difference of up to 25% between the Glen and ESTAR velocities in the topographic depression, and a difference of almost 20% in the surface layers over the topographic bump. We have amended the manuscript in section 5.2 for ISMIPB to include discussion on this smaller aspect ratio, as follows (P14L14-22):

"In addition to the case where $L = 20$ km, we also investigated the impact of reducing the horizontal extent to $L = 5$ km. In this steeper bed scenario (Fig. 7), the ESTAR surface velocities are at least 11% slower than the Glen velocities in the surface layers across the whole domain, as much as 20% slower around the topographic bump, and up to 25% slower in the topographic depression (Fig. 7c). The much greater reductions in the magnitude of the ESTAR velocities for $L = 5$ km are a consequence of the increasing importance of longitudinal stresses in the stress balance equations for the smaller aspect ratio (Fig. 7e), and also in some areas the lower strain rates, which lead to correspondingly stiffer ice. Indeed we see a clear decline in the shear strain rate in the lower part of the bed depression in Fig. 7f, in contrast to Fig. 6f. The qualitative pattern of the longitudinal strain-rates in Fig. 7e is similar to the $L = 20$ km case, although the horizontal gradients are naturally accentuated, and the "transition curves" are displaced."

Note that while the contrast due to the ESTAR incorporation of anisotropy is greater for the $L = 5$ km case, the structure and patterns of the results are broadly similar, e.g. compare Figs. 6 and 7 from the updated manuscript. We have extended the discussion section (as suggested) to cover these additional results (P17L20-P17L30):

"For more rapidly varying bed topography in ISMIPB, with $L = 5$ km, the differences in velocity for the two flow relations reached 25%, with surface variations of 11%...These results suggest if major bed topography only varied on scales much longer than the ice thickness, close agreement between ESTAR and the Glen flow relation might be achieved more generally by choosing the
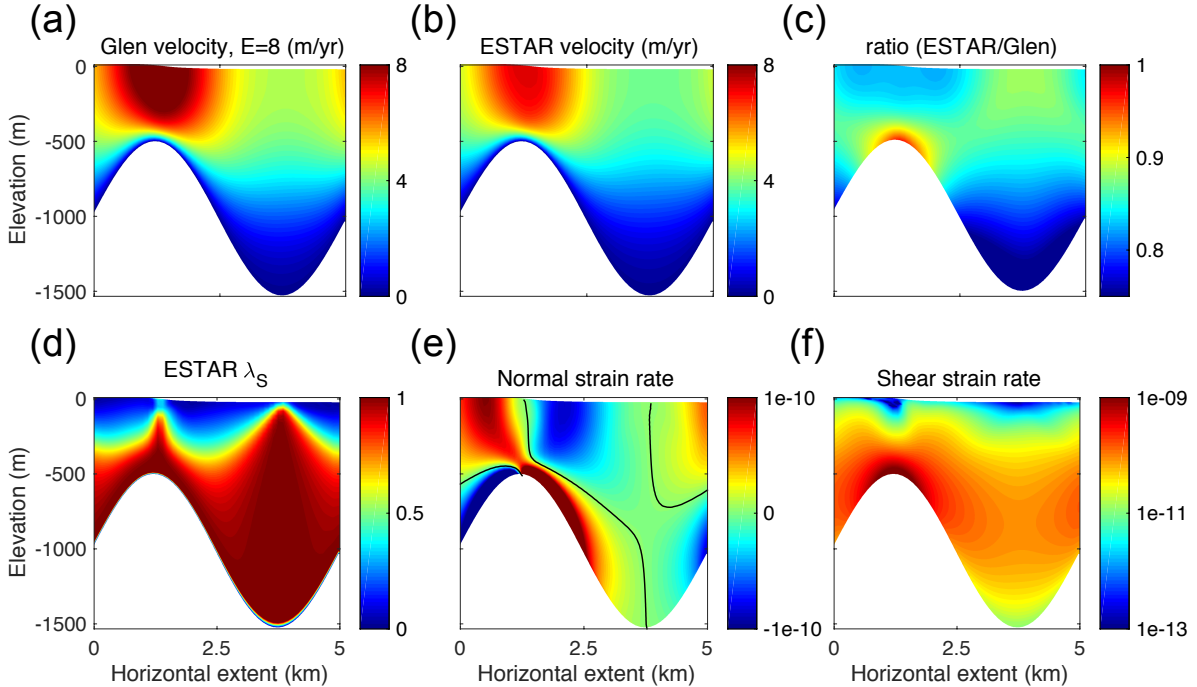
22

Figure 4: Steady-state results for the ISMIPB experiment with horizontal extent $L = 5$ km. **(a)** Glen ($E_G = 8$) along-flow velocity v_x (m yr^{-1}); **(b)** ESTAR v_x (m yr^{-1}); **(c)** ratio of ESTAR/Glen v_x ($E_G = 8$); **(d)** ESTAR λ_S, **(e)** ESTAR normal strain (s^{-1}), and **(f)** ESTAR shear strain rate (s^{-1}). The black contours in **(e)** correspond to the curves where $\dot{\varepsilon}_{xx} = 0$.

tertiary shear enhancement factor as the Glen enhancement factor ($E_G = E_S$). This might provide a physical rationale to replace the *ad hoc* enhancement factors typically used in large-scale grounded ice sheet modelling with the value appropriate to flow dominated by simple shear. However, larger differences between velocities and vertical shear profiles emerged for the more rapid bedrock variation, where the importance of including longitudinal stresses in the momentum balance is already recognised (Pattyn et al., 2008), suggesting that adopting ESTAR would be preferable."

We do not observe similar dramatic changes in flow for ISMIPD when the horizontal extent is reduced (Fig. 5 below). In the ISMIPD experiments, sliding dominates over deformation to an extreme extent for both length scales. For $L = 20$ km (new Fig. 8 of the manuscript) the only difference between the velocities for the Glen and ESTAR cases are observed over the sticky spot. The differences between the horizontal velocities in ISMIPD tests are less than 1% in both cases, which already had prompted us to examine the ratio of the deformational contributions to the velocities as well. While these are clearly very small contributors to the flow, we observe that there is both a marked spatial contrast in the ratio, and a considerable change in that contrast between the two spatial scales.

For $L = 20$ km the aspect ratio appears to favour a simple correlation between the variation in bed friction coefficient and the deformational regime. Over the slippery spot the stiffer ice of the ESTAR case correlates with stiffer ice a reduced horizontal deformational velocity, but for $L = 5$ km a different, more complex picture emerges. The structure of the longitudinal strain rates is similar for both aspect ratios, but the pattern of shear strain rates is more complex for $L = 5$ km. We note the resulting interesting pattern in λ_S (Fig. 5 below) compared with λ_S for the $L = 20$ km case (Fig. 9

from the manuscript). This is commented on in the explanation of the surface spike structures (see below). Again, and as remarked in the updated manuscript (P16L4-13), the only region for which λ_S is relevant and plays a role in the dynamics is the region over the sticky spot, where deformation is the dominant control of flow near the bed. In this region, the proportion of shear-dominated deformational flow does not increase markedly over the $L = 20$ km case. We have included discussion on the impact of the smaller aspect ratio (P16L14-29):

"The results of a FS prognostic run to steady-state for the ISMIPD experiment for $L = 5$ km are presented in Fig. 10. The v_x velocity ratio (Fig. 10c) shows that very little difference is seen between results for the two flow relations, unlike the ISMIPB experiments in the previous section, where differences up to 25% between ESTAR and Glen cases emerged for the shorter bedrock periodicity. The tiny differences in overall velocities are enhanced but the patterns in Fig. 9c and Fig. 10c are similar. However, there is a significantly different picture in the ratio of deformation velocities seen in Fig. 10d, compared to Fig. 9e. The largest differences are now limited to the lower portion of the ice column and for much of the region over the slippery bed the ratio is almost unity.

The pattern of deformation regimes mapped by λ_S (Fig. 10f) is also more complex than that seen in the preceding $L = 20$ km case (see Fig. 9d). The general structure of the normal strain rates is similar to previous experiments, but here the persistence of a band of shear (Fig. 10h) above the slippery spot at intermediate depths prevents the establishment of a vertical block of flow dominated by normal stresses. The shear profile above the sticky spot is also much weaker in the upper layers. Accordingly, λ_S reveals a band of unevenly shear-dominated deformation which is continuous across the periodic domain. Once again, shear dominated spikes extend towards the surface in association with the vanishing of the normal strain rates.

The spatial variations in the viscosity ratio (Fig. 10e) depart significantly from those of λ_S, reflecting more strikingly than for $L = 20$ km (Fig. 9e) the combined influence of the pattern of enhancement (controlled by $E(\lambda_S)$) and the effect of different strain rates, with values both above and below the range (1.0-1.39) directly controlled by $E(\lambda_S)/E_G$."
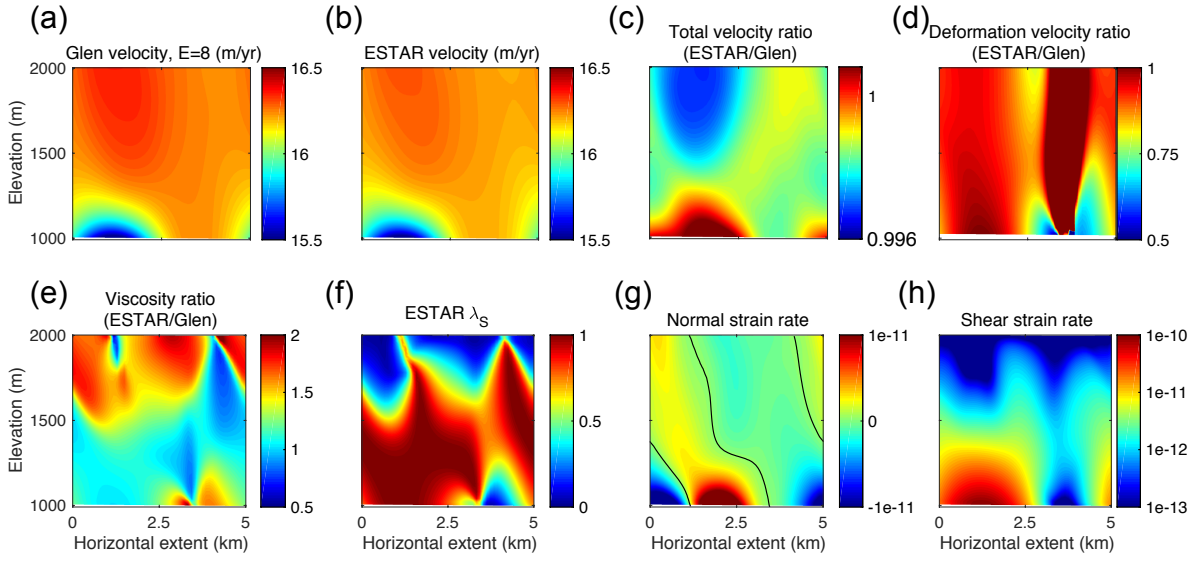
Figure 5: Steady-state results for the ISMIPD experiment with horizontal extent $L = 5$ km. **(a)** Glen ($E_G = 8$) along-flow velocity v_x (m yr^{-1}); **(b)** ESTAR v_x (m yr^{-1}); **(c)** ratio of ESTAR/Glen v_x ($E_G = 8$); **(d)** ratio of ESTAR/Glen deformation v_x; **(e)** ratio of ESTAR/Glen viscosity; **(f)** ESTAR λ_S; **(g)** ESTAR normal strain (s^{-1}); and **(h)** ESTAR shear strain rate (s^{-1}). The black contours in **(g)** correspond to the curves where $\dot{\varepsilon}_{xx} = 0$.

Other modifications

As indicated at the start of this response document, we have considerably expanded the discussion section as suggested (Sect. 6). The additional observations led to some alterations in ordering in that section. We also introduced additional diagnostics in the results section (Sect. 5) – including ratios of total and deformational velocities and of viscosities to assist our interpretation of the influence of ESTAR versus Glen rheology. We changed the presentation of shear strain rates to use a logarithmic colour scale to better capture the contrast and assist in the interpretation. The conclusion (Sect. 7) has also been expanded to cover the additional insights and to respond to reviewers' concerns.

References

Azuma, N. and Higashi, A.: Mechanical properties of Dye 3 Greenland deep ice cores, Ann. Glaciol., pp. 1–8, 1984.

Azuma, N., Wang, Y., Mori, K., Narita, H., Hondoh, T., Shoji, H., and Watanabe, O.: Textures and fabrics in the Dome F (Antarctica) ice core, Ann. Glaciol., 29, 163–168, doi:10.3189/172756499781821148, 1999.

Bouchez, J. and Duval, P.: The fabric of polycrystalline ice deformed in simple shear: Experiments in torsion, natural deformation and geometrical interpretation, Texture Microstruct, 5, 171–190, 1982.

Breuer, B., Lange, M. A., and Blindow, N.: Sensitivity studies on model modifications to assess the dynamics of a temperature ice cap, such as that on King George Island, Antarctica, J. Glaciol., 52, 235–247, 2006.

Budd, W. and Jacka, T.: A review of ice rheology for ice sheet modelling, Cold Reg. Sci. Technol., 16, 107–144, 1989.

Budd, W. F.: The development of crystal orientation fabrics in moving ice, Z. Gletscherkd. Glazialgeol, 8, 65–105, 1972.

Budd, W. F., Warner, R. C., Jacka, T. H., Li, J., and Treverrow, A.: Ice flow relations for stress and strain-rate components from combined shear and compression laboratory experiments, J. Glaciol., 59, 374–392, doi:10.3189/2013JoG12J106, 2013.

Cuffey, K. and Paterson, W. S. B.: The Physics of Glaciers, 4th Edition, Elsevier, Oxford, 2010.

Dahl-Jensen, D. and Gundestrup, N.: Constitutive properties of ice at Dye 3, Greenland, in: The Physical Basis of Ice Sheet Modelling, edited by Waddington, E. and Walder, J., pp. 31–43, IAHS Publ. no. 170, 1987.

DiPrinzio, C., Wilen, L., Alley, R., Fitzpatrick, J., Spencer, M., and Gow, A.: Fabric and texture at Siple Dome, Antarctica, J. Glaciol., 51, 281–290, 2005.

Durand, G., Gillet-Chaulet, F., Svensson, A., Gagliardini, O., Kipfstuhl, S., Meyssonnier, J., Parrenin, F., Duval, P., and Dahl-Jensen, D.: Change in ice rheology during climate variations – implications for ice flow modelling and dating of the EPICA Dome C core, Clim. Past, pp. 155–167, doi:10.5194/cp-3-155-2007, 2007.

Duval, P. and Castelnau, O.: Dynamic recrystallisation of ice in polar ice sheets, Journal de Physique IV, Colloque C3, supplement to Journal de Physique III, 5, 197–205, 1995.

Etheridge, D.: Dynamics of the Law Dome ice cap, Antarctica, as found from bore-hole measurements, Ann. Glaciol., 12, 46–50, 1989.

Faria, S. H.: The symmetry group of the CAFFE model, J. Glaciol., 54, 643–645, doi:10.3189/002214308786570935, 2008.

Faria, S. H., Weikusat, I., and Azuma, N.: The microstructure of polar ice. Part II: State of the art, J. Struct. Geol., 61, 21 – 49, doi:10.1016/j.jsg.2013.11.003, 2014.

Gao, X. and Jacka, T.: The approach to similar tertiary creep rates for Antarctic core ice and laboratory prepared ice, Journal de Physique, Colloque C1, supplement to no. 3, Tome 48, pp. 289–296, 1987.

Gow, A.: The inner structure of the Ross Ice Shelf at Little America, Antarctica, as revealed by deep core drilling, in: IUGG General Assembly of Berkeley, pp. 272–284, IASH Publ. No. 61, 1963.

Gow, A. and Williamson, T.: Rheological Implications Of Internal Structure And Crystal Fabrics Of West Antarctic Ice Sheet As Revealed By Deep Core Drilling At Byrd-station, Geol. Soc. Am. Bull., 87, 1665–1677, 1976.

Gow, A., D.A., M., Alley, R., Fitzpatrick, J., Anandakrishnan, S., Woods, G., and Elder, B.: Physical and structural properties of the Greenland Ice Sheet Project 2 ice core: A review, J. Geophys. Res., 102, 26 559–26 575, 1997.

Herron, S., Langway, Jr, C., and Brugger, K.: Ultrasonic velocities and crystalline anisotropy in the ice core from Dye 3, Greenland, in: Greenland ice core : geophysics, geochemistry, and the environment, edited by Langway, Jr, C., Oeschger, H., and Dansgaard, W., no. 33 in Geophysical monograph, pp. 23–31, American Geophysical Union, 1985.

Hulbe, C. L., Wang, W., Joughin, I. R., and Siegert, M. J.: The role of lateral and vertical shear in tributary flow toward a West Antarctic ice stream, Ann. Glaciol., 36, 244–250, 2003.

Jacka, T.: Laboratory studies on relationships between ice crystal size and flow rate, Cold Reg. Sci. Technol., 10, 31–42, 1984.

Jacka, T. and Li, J.: Flow rate and crystal orientation fabrics in compression of polycrystalline ice at low temperatures and stresses, in: Physics of Ice Core Records, edited by Hondoh, T., pp. 83–101, The Institute of Low Temperature Science, Hokkaido University, Sapporo, Hokkaido University Press, Sapporo, 2000.

Jacka, T. and Maccagnan, M.: Ice crystallographic and strain rate changes with strain in compression and extension, Cold Reg. Sci. Technol., 8, 269–286, 1984.

Jansen, D., Weikusat, I., Kleiner, T., Wilhelms, F., Dahl-Jensen, D., Frenzel, A., Binder, T., Eichler, J., Faria, S., Sheldon, S., Panton, C., Kipfstuhl, S., and Miller, H.: In situ-measurement of ice deformation from repeated borehole logging of the EPICA Dronning Maud Land (EDML) ice core, East Antarctica., in: Geophysical Research Abstracts, vol. 19, EGU General Assembly, 2017.

Kipfstuhl, S., Faria, S., Azuma, N., Freitag, J., Hamann, I., Kaufmann, P., Miller, H., Weiler, K., and Wilhelms, F.: Evidence of dynamic recrystallization in polar firn, J. Geophys. Res., 114, B05 204, 2009.

Li, J. and Jacka, T.: Correspondence. Horizontal shear rate of ice initially exhibiting vertical compression fabrics, J. Glaciol., 44, 670–672, 1998.

Li, J., Jacka, J., and Budd, W. F.: Deformation rates in combined compression and shear for ice which is initially isotropic and after the development of strong anisotropy, Ann. Glaciol., 23, 247–252, 1996.

Li, J., Jacka, T., and Budd, W.: Strong single-maximum crystal fabrics developed in ice undergoing shear with unconstrained normal deformation, Ann. Glaciol., 30, 88–92, 2000.

Montagnat, M., Buiron, D., Arnaud, L., Broquet, A., Schlitz, P., Jacob, R., and Kipfstuhl, S.: Measurements and numerical simulation of fabric evolution along the Talos Dome ice core, Antarctica, Earth Planet. Sci. Lett., 357–358, 168 – 178, doi:10.1016/j.epsl.2012.09.025, 2012.

Montagnat, M., Azuma, N., Dahl-Jensen, D., Eichler, J., Fujita, S., Gillet-Chaulet, F., Kipfstuhl, S., Samyn, D., Svensson, A., and Weikusat, I.: Fabric along the NEEM ice core, Greenland, and its comparison with GRIP and NGRIP ice cores, The Cryosphere, 8, 1129–1138, doi:10.5194/tc-8-1129-2014, 2014.

Morgan, V., Wookey, C., Li, J., van Ommen, T., Skinner, W., and Fitzpatrick, M.: Site information and initial results from deep ice drilling on Law Dome, Antarctica, J. Glaciol., 43, 3–10, 1997.

Morgan, V., van Ommen, T., Elcheikh, A., and Li, J.: Variations in shear deformation rate with depth at Dome Summit South, Law Dome, East Antarctica, Ann. Glaciol., pp. 135–139, 1998.

Pattyn, F., Perichon, L., Aschwanden, A., Breuer, B., de Smedt, B., Gagliardini, O., Gudmundsson, G. H., Hindmarsh, R. C. A., Hubbard, A., Johnson, J. V., Kleiner, T., Konovalov, Y., Martin, C., Payne, A. J., Pollard, D., Price, S., Rückamp, M., Saito, F., Soucek, O., Sugiyama, S., and Zwinger, T.: Benchmark experiments for higher-order and full-Stokes ice sheet models (ISMIP-HOM), The Cryosphere, 2, 95–108, 2008.

Placidi, L., Greve, R., Seddik, H., and Faria, S.: Continuum-mechanical, Anisotropic Flow model, for polar ice masses, based on an anisotropic Flow Enhancement factor, Continuum Mech. Thermodyn., 22, 221–237, doi:10.1007/s00161-009-0126-0, 2010.

Prior, D., Lilly, K., Seidemann, M., Vaughan, M., Becroft, L., Easingwood, R., Diebold, S., Obbard, R., Daghlian, C., Baker, I., Caswell, T., Golding, N., Goldsby, D., Durham, W., Piazolo, S., and Wilson, C.: Making EBSD on water ice routine, J. Microsc., pp. 1–20, doi:10.1111/jmi.12258, 2015.

Qi, C., Goldsby, D. L., and Prior, D.: The down-stress transition from cluster to cone fabrics in experimentally deformed ice, Earth Planet. Sci. Lett., 471, 136–147, doi:10.1016/j.epsl.2017.05.008, 2017.

Russell-Head, D. and Budd, W.: Ice-sheet flow properties derived from bore-hole shear measurements combined with ice-core studies, J. Glaciol., 24, 117–130, 1979.

Schulson, E. and Duval, P.: Creep and fracture of ice, Cambridge University Press, Cambridge UK, 2009.

Steinbach, F., Bons, P. D., Griera, A., Jansen, D., Llorens, M.-G., Roessiger, J., and Weikusat, I.: Strain localization and dynamic recrystallization in the ice–air aggregate: a numerical study, The Cryosphere, 10, 3071–3089, doi:10.5194/tc-10-3071-2016, 2016.

Thorsteinsson, T., Kipfstuhl, J., and Miller, H.: Textures and fabrics in the GRIP ice core, J. Geophys. Res., 102, 26 583–26 599, doi:10.1029/97JC00161, 1997.

Tison, J.-L., Thorsteinsson, T., Lorrain, R., and Kipfstuhl, J.: Origin and development of textures and fabrics in basal ice at Summit, Central Greenland, Earth Planet. Sci. Lett., 125, 421–437, doi:10.1016/0012-821X(94)90230-5, 1994.

Treverrow, A., Budd, W. F., Jacka, T. H., and Warner, R. C.: The tertiary creep of polycrystalline ice: experimental evidence for stress-dependent levels of strain-rate enhancement, J. Glaciol., 58, 301–314, doi:10.3189/2012JoG11J149, 2012.

Treverrow, A., Warner, R. C., Budd, W. F., Jacka, T. H., and Roberts, J. L.: Modelled stress distributions at the Dome Summit South borehole, Law Dome, East Antarctica: a comparison of anisotropic ice flow relations, J. Glaciol., 61, 987–1004, doi:13.3189/2016JoG14J198, 2015.

Treverrow, A., Jun, L., and Jacka, T. H.: Ice crystal c-axis orientation and mean grain size measurements from the Dome Summit South ice core, Law Dome, East Antarctica, Earth System Science Data, 8, 253–263, doi:10.5194/essd-8-253-2016, 2016.

Wakahama, G.: On the structure and texture of deep ice cores from the Amery Ice Shelf, Wilkes Dome and Cape Folger, Antarctica, in: Physical and Chemical Studies of Ices from Glaciers and Ice Sheets, pp. 99–108, Institute of Low Temperature Science, Hokkaido University, Sapporo, Japan, 1974.

Wang, W. and Warner, R. C.: Modelling of anisotropic ice flow in Law Dome, East Antarctica, Ann. Glaciol., 29, 184–190, 1999.

Wang, W., Warner, R. C., and Budd, W. F.: Ice-flow properties at Dome Summit South, Law Dome, East Antarctica, Ann. Glaciol., 35, 567–573, 2002a.

Wang, W., Jun, L., Zwally, H. J., Morgan, V., and van Ommen, T. D.: The effect of anistropic flow properties on ice-sheet surface elevation change, Ann. Glaciol., 39, 439–444, 2004.

Wang, W., Li, J., and Zwally, H. J.: Dynamic inland propagation of thinning due to ice loss at the margins of the Greenland ice sheet, J. Glaciol., 58, 734–740, doi:10.3189/2012JoG11J187, 2012.

Wang, W. L. and Warner, R. C.: Simulation of the influence of ice rheology on velocity profiles and ice-sheet mass balance, Ann. Glaciol., 27, 194–200, 1998.

Wang, W. L., Zwally, H. J., Abdalati, W., and Luo, S.: Modeling of ice flow and internal layers along a flowline through Swiss Camp, West Greenland, Ann. Glaciol., 34, 303–308, 2002b.

Wang, W. L., Zwally, H. J., Hulbe, C. L., Siegert, M. J., and Joughin, I. R.: Anisotropic ice flow leading to the onset of Ice Stream D, West Antarctica: numerical modelling based on the observations from Byrd Station borehole, Ann. Glaciol., 37, 397–403, 2003.

Warner, R. C., Jacka, T. H., Li, J., and Budd, W. F.: Tertiary flow relations for compression and shear components in combined stress tests on ice, in: Advances in cold-region thermal engineering and sciences: technological, environmental, and climatological impact, edited by Hutter, K., Wang, Y., and Beer, H., pp. 259–270, Springer-Verlag, 1999.

Weikusat, I., Kipfstuhl, S., Azuma, N., Faria, S., and Miyamoto, A.: Deformation microstructures in an Antarctic ice core (EDML) and in experimentally deformed ice, in: Physics of Ice Core Records II, edited by Hondoh, T., pp. 115–123, Hokkaido University Press, Sapporo, 2009a.

Weikusat, I., Kipfstuhl, S., Faria, S. H., Azuma, N., and Miyamoto, A.: Subgrain boundaries and related microstructural features in EDML (Antarctica) deep ice core, J. Glaciol., 55, 461–472, doi:10.3189/002214309788816614, 2009b.

Weikusat, I., Jansen, D., Binder, T., Eichler, J., Faria, S. H., Wilhelms, F., Kipfstuhl, S., Sheldon, S., Miller, H., Dahl-Jensen, D., and Kleiner, T.: Physical analysis of an Antarctic ice core—towards an integration of micro- and macrodynamics of polar ice, Philosophical Transactions of the Royal Society of London A: Mathematical, Physical and Engineering Sciences, 375, doi:10.1098/rsta.2015.0347, 2016.

Wilson, C.: Fabrics in polycrystalline ice deformed experimentally at -10°C, Cold Reg. Sci. Technol., pp. 149–161, 1982.

Wilson, C. and Peternell, M.: Ice deformed in compression and simple shear: control of temperature and intial fabric, J. Glaciol., 207, 11–22, doi: 10.3189/2012JoG11J065, 2012.

Wilson, C. and Sim, H.: The localization of strain and c-axis evolution in anisotropic ice, J. Glaciol., 48, 601–610, 2002.

Implementing an empirical scalar tertiary anisotropic rheology (ESTAR) into large-scale ice sheet models

Felicity S. Graham[1], Mathieu Morlighem[2], Roland C. Warner[3], and Adam Treverrow[3]

[1]Institute for Marine and Antarctic Studies, University of Tasmania, Private Bag 129, Hobart, Tasmania 7001, Australia
[2]Department of Earth System Science, University of California, Irvine, California, USA
[3]Antarctic Climate and Ecosystems Cooperative Research Centre, Private Bag 80, Hobart, Tasmania 7001, Australia

Correspondence to: Felicity S. Graham (felicity.graham@utas.edu.au)

Abstract. The microstructural evolution that occurs in polycrystalline ice during deformation leads to the development of anisotropic rheological properties that are not adequately described by the most common, isotropic, ice flow relation used in large-scale ice sheet models – the Glen flow relation. We present a preliminary assessment of the implementation in the Ice Sheet System Model (ISSM) of a computationally-efficient, empirical, scalar, tertiary, anisotropic rheology (ESTAR). The

5   effect of this anisotropic rheology on ice flow dynamics is investigated by comparing idealised simulations using ESTAR with those using the isotropic Glen flow relation, where the latter includes ~~a~~ an overall flow enhancement factor. For an idealised embayed ice shelf, the Glen flow relation overestimates velocities by up to 17% when using an enhancement factor equivalent to the maximum value prescribed by ESTAR. Importantly, no single Glen enhancement factor can accurately capture the spatial variations in flow over the ice shelf. For flow-line studies of idealised grounded flow over ~~a bumpy topography or a sticky~~

10   ~~base~~ varying topography or variable basal friction – both scenarios dominated at depth by bed-parallel shear – the differences between simulated velocities using ESTAR and the Glen flow relation vary according to the value of the enhancement factor used to calibrate the Glen flow relation. These results demonstrate the importance of describing the anisotropic rheology of ice in a physically realistic manner, and have implications for simulations of ice sheet evolution used to reconstruct paleo-ice sheet extent and predict future ice sheet contributions to sea level.

1 Introduction

15   An essential component of an ice sheet model is its formulation of ice rheology, which relates deformation rates to applied stresses. Data from laboratory ice deformation experiments can be used to define flow relations suitable for implementation in numerical ice sheet models. Previous experiments have demonstrated that under conditions of constant stress and temperature, polycrystalline ice with a statistically random distribution of crystallographic c-axes (fabric) initially behaves as a mechanically

20   isotropic material (Budd and Jacka, 1989) where the rate of deformation is not sensitive to the character of the applied stresses. We use the term fabric to describe the distribution of crystallographic c-axis orientations within a polycrystalline aggregate. At the commencement of deformation, during the primary stage of creep, the initially high strain rate rapidly decreases. A minimum strain rate is reached during secondary creep (Fig. 1), which is associated with a transitory balance between strain hardening and the strain-induced activation of microstructural recovery processes. With continued strain, a tertiary stage of

1

creep is established (typically observed at strain of $\sim 10\%$ in laboratory experiments), which is characterised by a dynamic balance between microdeformation and recovery processes, statistically steady-state anisotropic polycrystalline microstructures (e.g., crystal orientation fabric and grain size), and steady strain rates that are enhanced relative to the rate observed during secondary creep.

5   Tertiary creep, with the associated development of polycrystalline anisotropy driven by the microstructural response to applied stresses, is the predominant mode of ice deformation in ice sheets ~~. The~~ (Budd and Jacka, 1989) . The pattern of fabric anisotropy and the tertiary strain rates both depend on the nature of the applied stresses (Fig. 1). Attaining a state of tertiary creep requires that a stable pattern of stresses acts for sufficient time to develop the compatible crystal anisotropy. We can expect this tertiary state to be common throughout the bulk of a polar ice sheet from simple considerations of the observed

10   velocities and strain rates, provided the spatial pattern of deformation varies slowly compared to the passage of ice through that pattern. Clearly there are also some regions where tertiary flow is not expected to be achieved. We discuss applicability of this tertiary creep assumption in more detail in Sects. 2.2 and 2.3, and in discussions in Sect. 6 in light of the results of the idealised experiments.

    The prevailing description of ice rheology used in large-scale ice sheet models, the Glen flow relation (Glen, 1952, 1953,

15   1955, 1958; Nye, 1953), is a creep power law:

$$\dot{\boldsymbol{\varepsilon}} = A(T')\tau_e^{n-1}\boldsymbol{\sigma}', \tag{1}$$

where $\dot{\boldsymbol{\varepsilon}}$ is the strain rate tensor (s^{-1}), τ_e is the effective stress (Pa), proportional to the second invariant of the deviatoric stress tensor $\boldsymbol{\sigma}'$, and n is a power law stress exponent (observations support a value of $n = 3$). $A(T')$ is a ~~temperature dependent~~ flow parameter (Pa^{-n} s^{-1}), dependent on homologous temperature T' and persistent material properties, for which various

20   parameterisations exist based on laboratory tests and field measurements (e.g., Budd and Jacka, 1989; Cuffey and Paterson, 2010).

    The Glen flow relation was empirically derived from secondary creep rates, determined under various conditions of constant stress and temperature, for polycrystalline ice with an initially random distribution of c-axes and assuming mechanical isotropy. While the Glen flow relation captures the observed nonlinear response of ice deformation to ~~an applied stress~~the magnitude

25   of applied stresses, it is unable to account for the mechanical anisotropy of polycrystalline ice ~~during~~ that develops during the transition to tertiary creep (e.g., Nye, 1953; Glen, 1958; Budd et al., 2013). That is, it cannot explain the dependence of tertiary strain rates on the character of the applied stress. To account for the increased deformability associated with tertiary creep, a common adaptation of the Glen flow relation is the inclusion of a constant flow enhancement factor, E_G,

$$\dot{\boldsymbol{\varepsilon}} = E_G A(T')\tau_e^{n-1}\boldsymbol{\sigma}'. \tag{2}$$

30   The specification of E_G is typically ad hoc: E_G may be selected from reported experimental values (e.g., Duval, 1981; Jacka and Maccagnan, 1984; Pimienta et al., 1987; Treverrow et al., 2012), or used as a model tuning parameter~~(e. g., to alter the relative contribution of viscous deformation and basal sliding to the overall dynamics of an ice sheet). In either~~. Such a parameter is included in most large-scale ice sheet models (e.g., Saito and Abe-Ouchi, 2004; Greve, 2005; Huybrechts et al., 2007; Winkel

Indeed, Greve and Blatter (2009) comment that it is "often introduced without explicitly mentioning anisotropy". In any case, a value of E_G that does not vary spatially in connection with the fabric and flow configuration, will lead to an unrealistic spatial distribution of strain rates (Wang and Warner, 1999; Wang et al., 2002a; Treverrow et al., 2015). Previous studies have used anisotropic flow models or approximations to assign regional values to E_G (e.g., Ma et al., 2010) that may also vary according to the prevailing stress regime.

Budd et al. (2013) recently proposed an anisotropic flow relation based on results from laboratory ice deformation experiments involving simple shear, compression, and combinations of these. As tertiary creep rates and the corresponding compatible fabrics were found to vary according to the relative proportions of the simple shear and compression stresses, Budd et al. (2013) defined an enhancement factor E as an anisotropic function of the stress configuration, based on interpolating between separate, experimentally-determined enhancement factors for simple shear-alone and compression-alone. We refer to the generalised form of the anisotropic flow relation proposed by Budd et al. (2013) as ESTAR (Empirical, Scalar, Tertiary, Anisotropic Rheology), since it is based on tertiary (steady-state) creep rates describing the deformation of anisotropic ice and features a scalar (collinear) relationship between the strain rate and deviatoric stress tensor components.

Here, as a first step towards exploring the implications of this description of tertiary creep, we describe how to implement ESTAR in large-scale ice sheet models and apply the required changes to the Ice Sheet System Model (ISSM; Larour et al., 2012). ISSM is a thermomechanical finite element model that solves the full system of Stokes equations to describe ice flow. This will permit exploration of the ramifications of ESTAR in general ice flow situations. In an initial study here, we examine the effect of anisotropy in simple, idealised scenarios of a floating ice shelf and of grounded ice sheets, comparing simulated flow fields using ESTAR with the corresponding isotropic flow modelled by the Glen flow relation. Section 2 presents a brief overview of anisotropic rheologies, including the experimental and theoretical basis for ESTAR. Section 3 details the implementation of ESTAR in ISSM while Sect. 4 verifies the implementation against an analytical solution. In Sect. 5, we compare simulations of ice flow with ESTAR and the Glen flow relation using a suite of idealised flow geometries, including selected experiments from the Ice Sheet Model Intercomparison Project for Higher Order Models (ISMIP-HOM; Pattyn et al., 2007). Section 6 discusses the results, and implications of the ESTAR description of the flow of anisotropic ice. Conclusions are drawn together in Sect. 7.

2 Anisotropic ice rheology

A range of ice rheologies have been proposed to account for polycrystalline anisotropy. They can be broadly grouped in two categories: (1) those defined at the individual ice crystal scale, where the effects of anisotropy are parameterised based on specific properties of individual crystals, and (2) those that describe anisotropic aspects of deformation empirically: either based on regional expectations about local crystallographic microstructure, or through an empirical function of the stress configuration. In this section, we briefly review these two approaches, and the underlying experimental and modelling basis for ESTAR. In what follows, we distinguish between the Glen enhancement factor E_G and the ESTAR enhancement factor

$E(\lambda_S)$, which is a function of compression deviatoric and simple shear stresses, parameterised by the shear fraction λ_S. Where necessary, we denote a more general enhancement factor, i.e., with unspecified form, as E.

2.1 Microstructure approaches

Experiments on single crystals of ice demonstrate that deformation occurs predominantly by slip on the crystallographic basal plane, with the yield stress being geometrically related to the magnitude of the applied stress resolved onto the basal plane (Trickett et al., 2000) according to Schmid's Law (Schmid and Boas, 1950). This observation, in conjunction with the development of crystallographic preferred orientations during deformation of polycrystalline ice to high strains (e.g. Russell-Head and Budd, 1979; Jacka and Maccagnan, 1984; Pimienta et al., 1987; Morgan et al., 1998; DiPrinzio et al., 2005; Durand et al., 2009; Budd et al., 2013; Montagnat et al., 2014), has driven the development of rheological descriptions in which the connection between deviatoric stresses and resulting strain-rates is regarded as an intrinsic material property determined by the effects of microstructure on bulk deformation processes, (e.g. Lile, 1978; Lliboutry, 1993; Azuma and Goto-Azuma, 1996; Staroszczyk and Gagliardini, 1999; Thorsteinsson, 2001; Gödert, 2003; Gillet-Chaulet et al., 2005; Pettit et al., 2007; Placidi et al., 2010). See also the review by Gagliardini et al. (2009). In broad terms, the anisotropic nature of these rheological descriptions is derived from the geometric relationship between the crystallographic c-~~axis~~ -axes and the stresses driving deformation, with the role of misorientation relationships between nearest neighbour grains explicitly considered in some cases.

The complexity of numerical flow relations varies according to the extent to which a physically realistic description of microdeformation and recovery processes, or a parameterisation of these, enters into the relationship between strain rates and the stresses driving deformation. Many of these rheological models are more complicated than a collinear flow relation and involve a tensor coupling in place of Eq. 2. A further consideration is the quantitative description of fabric that is used in flow relations. Those incorporating a discrete, c-axis vector based description of fabric (e.g. Lile, 1978; van der Veen and Whillans, 1994; Azuma and Goto-Azuma, 1996; Thorsteinsson, 2002) are only appropriate for highly localised studies and are incompatible with large-scale ice sheet modelling. Flow relations based on a continuous description of fabric, e.g., a parameterised orientation distribution function (ODF) or c-axis orientation tensor are also possible (e.g. Staroszczyk and Gagliardini, 1999; Gödert, 2003; Gillet-Chaulet et al., 2005; Pettit et al., 2007; Placidi et al., 2010). Including any fabric-based rheological description in an ice sheet model requires a separate set of equations governing the fabric evolution. A ~~drawback to~~ complication of such an approach is the computational overhead and uncertainty associated with defining the spatial distribution of fabric within ice sheets, which is poorly constrained by observations. Furthermore, for simplicity, restricted forms of the ODF or orientation tensor are specified, which may not adequately describe all fabrics likely to be encountered in an ice sheet. As such, flow relations utilising a fabric description that relies on fabric evolution equations or that is imposed as a function of location within the ice sheet are currently restricted to regional simulations (e.g., Seddik et al., 2011; Martín and Gudmundsson, 2012; Zwinger et al., 2014).

2.2 Empirical approaches

A second approach comprising ÷ experimental and observational approaches (Li et al., 1996; Wang et al., 2002a, b), modelling (Wang and Warner, 1998, 1999; Hulbe et al., 2003; Wang et al., 2003, 2004; Breuer et al., 2006; Wang et al., 2012), and theoretical studies (Warner et al., 1999), has focussed on the development and assessment of an anisotropic flow relation for poly-

5 crystalline ice in which the nature of the crystal fabric and the magnitude of strain rate enhancement, E, are both regarded as determined by the stress regime. This assumption is supported by experimental observations for pure polycrystalline ice, which demonstrate that an accumulated strain of $\sim 10\%$ is required for the microstructure to evolve to a state that is compatible with the flow configuration, irrespective of its initial condition (Jacka and Maccagnan, 1984; Gao and Jacka, 1987; Li and Jacka, 1998; Treverro Specifically, this approach regards the fabric and the enhancement in tertiary flow as determined by the relative proportions

10 of the simple shear and normal deviatoric stresses. For such flow relations, it is typically assumed that the spatial variation in dynamic conditions (e.g., flow configuration and temperature) only occur gradually in an ice sheet, so that the microstructure evolves to maintain compatibility with these conditions. ~~That is, throughout~~ Through most of an ice sheet we expect that the rate of microstructural evolution generally exceeds the rate at which the flow configuration varies. ~~This assumption is supported by experimental observations for pure polycrystalline ice, which demonstrate that an accumulated strain of~~

15 ~~$\lesssim 10\%$ is required for the microstructure to evolve to a state that is compatible with the flow configuration, irrespective of its initial condition (Jacka and Maccagnan, 1984; Gao and Jacka, 1987; Li and Jacka, 1998; Treverrow et al., 2012)~~, and that the distances travelled by a parcel of ice during the time taken to develop a compatible fabric are typically small compared to the relevant ice sheet spatial scales.

The anisotropic flow relation proposed by Budd et al. (2013) represents a continuation of this strand. They found that a scalar

20 anisotropic flow relation, i.e., one maintaining the collinear relationship between the components of $\dot{\varepsilon}$ and $\boldsymbol{\sigma}'$ (τ_e is a scalar function of the second invariant of $\boldsymbol{\sigma}'$) provides a good fit to laboratory data from combined compression and shear experiments. Such a scalar anisotropic rheology also simplifies the requirements for implementation within ice sheet models that are already compatible with the (scalar) Glen rheological description. Budd et al. (2013) proposed what we term ESTAR as a suitable candidate scalar anisotropic rheology generalised to arbitrary stress configurations (i.e., not restricted in its application to the

25 limited set of experimental stress configurations described in Li et al. (1996) and Budd et al. (2013)). A simplified version of ESTAR, called ESTAR-MFL (MFL: Minimal Flow Law), has also been incorporated into the ice sheet model SICOPOLIS (SImulation COde for POlythermal Ice Sheets, http://www.sicopolis.net; Greve and Blatter, 2009, 2016).

There are of course zones within an ice sheet where the assumption of compatible tertiary flow will not apply; however, we note that these zones will be restricted in their extent. We contend that ESTAR will apply to the vast majority of the dynamically

30 active regions of an ice sheet, in particular those zones where creep deformation makes a significant contribution to the overall flow. Specific zones where the assumption of tertiary creep may be inappropriate can be summarised as those where fabric has not yet evolved compatibility with the flow, where there is a rapid transition in the flow configuration, or where creep deformation makes only a minor contribution to the overall dynamics.

For example, in very cold ice in a low stress setting, such as the uppermost layers of the polar ice sheets, the time required to accumulate the strain necessary to develop a compatible fabric may lead to a near-surface zone in which the assumption of tertiary creep is not valid. Since the development of anisotropic fabrics provides an indication of the existence of tertiary flow, their observation at modest depths, (e.g., $\lesssim 100 - 200$ m; Morgan et al., 1997; DiPrinzio et al., 2005; Treverrow et al., 2016) allows estimation of the maximum extent of the zone where tertiary creep is not occurring. The observation within polar firn of microdeformation processes that are necessary for the development of fabric throughout ice sheets (e.g. Kipfstuhl et al., 2009; Faria et al., 2 that it may be appropriate to even further restrict the extent of the near-surface zone for which the assumption of tertiary creep is not valid. Additionally, the nonlinear nature of polycrystalline ice rheology leads to very high viscosities in low temperature and stress environments, so that incorrectly estimating deformation rates due to the assumption of tertiary flow in such regions may be of limited importance to simulations of ice sheet evolution.

Regions where rapid transitions in dynamic conditions can lead to abrupt changes in the pattern of applied stresses and a potential breakdown in tertiary flow compatibility include ice shelf grounding zones and other locations where basal traction is lost or abruptly changes, e.g., where ice flows over a subglacial lake, or with the onset of basal sliding in ice streams. The convergence zones where tributary glaciers or ice streams merge with a larger flow unit at a high angle may also lead to a transition in dynamic conditions that is problematic for the assumption of tertiary compatibility. Of course the more highly dynamic the evolving flow regime, the more rapidly a new compatible anisotropy will be established, so that the spatial interval where the flow relations are inapplicable may be limited. While there is little guidance on how to extend empirical flow relations to parametrise ice rheology in these transition regions, we note that similar difficulties exist for a Glen-type flow relation, which unlike ESTAR does not have the benefit of being able to correctly describe anisotropic enhancement throughout the remainder of the ice sheet.

2.3 Empirical scalar tertiary anisotropic rheology (ESTAR)

Here, we summarise the anisotropic rheology proposed by Budd et al. (2013) – ESTAR – that we are implementing in ISSM as an alternative to the Glen flow relation, to provide a relation more applicable to the tertiary creep of anisotropic polycrystalline ice typical of ice sheets and glaciers. ESTAR is a scalar power law formulation based on tertiary creep rates measured in laboratory ice deformation experiments under various combinations of simple shear and compression that has been generalised to arbitrary stress configurations. Recasting Eqs. 62 and 63 of Budd et al. (2013) to more closely resemble Eq. 2, ESTAR is given by the following expression:

$$\dot{\varepsilon} = E(\lambda_S)A(T')\tau_e^2 \boldsymbol{\sigma}'. \tag{3}$$

Assuming $n = 3$ in Eq. 2, Eq. 3 only differs from the Glen flow relation by the form of the functional enhancement factor $E(\lambda_S)$, which explicitly depends on the nature of the applied stresses via the shear fraction, λ_S, and could be regarded as providing a variable enhancement function for the Glen relation that incorporates the effect of anisotropy. We note in passing that in contrast to ISSM, flow relations in Budd et al. (2013) are couched in terms of the octahedral shear stress, $\tau_o = \sqrt{2/3}\tau_e$, which provides a more physically meaningful scalar measure of the overall stress magnitude than τ_e (Jaeger, 1969).

$E(\lambda_S)$ in Eq. 3 is defined as

$$E(\lambda_S) = E_C + (E_S - E_C)\lambda_S^2, \tag{4}$$

where E_C ~~is a compression enhancement factor, E_S is a simple shear enhancement factor,~~ and E_S are the enhancement factors above the minimum or secondary deformation rate of isotropic ice under compression alone or simple shear alone, respectively. The shear fraction λ_S in Eq. 4 is a non-dimensional variable ~~that takes~~ taking values in $[0, 1]$. ~~The shear fraction,~~ which characterises the contribution of simple shear ($\boldsymbol{\tau}'$) to the effective stress (τ_e)

$$\lambda_S = \frac{\|\boldsymbol{\tau}'\|}{\tau_e}. \tag{5}$$

The essence of Budd et al. (2013) and ESTAR is the observation that tertiary strain rates depend on the nature of the applied stresses, and the identification of the shear fraction λ_S is the appropriate variable to characterise that pattern. Accordingly, determining the portion of the overall deformation stress that can be regarded as simple shear is the main ingredient in implementing ESTAR. This involves the identification of a particular local plane – the local non-rotating shear plane – and the determination of the shear acting on that plane, $\boldsymbol{\tau}'$, as the measure of simple shear. As discussed in Budd et al. (2013), the importance of moving beyond strain rates to consider other aspects of flow – the 'movement picture' – has been recognised since at least the 1970s (e.g., Budd, 1972; Kamb, 1973; Duval, 1981). Duval (1981) identified the plane normal to the velocity gradient in a simple shear regime as the 'permanent shear plane' and discussed its role in the evolution of crystal fabrics. Budd et al. (2013) proposed a definition for this local plane in an arbitrary flow as the plane containing the vorticity vector associated solely with deformation and the velocity vector. As discussed below they also prescribed a further projection to remove any component of $\boldsymbol{\tau}'$ parallel to the deformational vorticity. The collinear nature of ESTAR (Eq. 3) allows λ_S to be written in terms of the corresponding strain rates, which is more convenient for Stokes flow modelling, as

$$\lambda_S = \frac{\dot{\varepsilon}'}{\dot{\varepsilon}_e}, \tag{6}$$

where $\dot{\varepsilon}'$ is the magnitude of the shear strain rate on the locally non-rotating shear plane, as defined in Eq. 7 below. In compression-alone scenarios, including three-dimensional uniaxial compression and two-dimensional plane compression and extension, $\lambda_S = 0$, so that $E(\lambda_S) = E_C$. Similarly, for simple shear alone, $\lambda_S = 1$ and $E(\lambda_S) = E_S$.

Analysis of tertiary creep rates for experiments conducted in simple shear-alone and compression-alone suggests that a suitable ratio of E_S to E_C for ice sheets is $\sim 8/3$ (Treverrow et al., 2012). The same ~~data also suggest~~ study also suggests that $E \propto \sqrt{\tau_e}$ for tertiary creep rates determined over a range of stress magnitudes. A flow relation incorporating such a stress dependent enhancement could be achieved by employing a creep power-law stress exponent of $n = 3.5$, rather than the more commonly used $n = 3$, assuming both E_S and E_C are described by functions of $\sqrt{\tau_e}$. For simplicity, we have excluded the apparent stress dependence of E_S and E_C in our initial implementation of ESTAR in ISSM since further work is required to verify the stress dependence of E_S and E_C experimentally for complex, combined stress configurations. Accordingly, we use scalar enhancement factors of $E_S = 8$ and $E_C = 3$ for the idealised scenarios examined in this study. These values may be at the higher end of the anticipated range in E_S and E_C for an ice sheet (see e.g., Russell-Head and Budd, 1979). However, the

strength of anisotropy and its influence on ice dynamics in comparison to the enhanced Glen flow relation depends on the ratio E_S/E_C and its spatial variation, i.e., the dynamically controlled distribution of $E(\lambda_S)$.

If the enhancement parameters are selected so that $E_C = E_S = E_G$, where E_G is the Glen enhancement factor, ESTAR becomes isotropic and equivalent to the Glen flow relation since $E(\lambda_S) \equiv E_G$. However, the viscous creep behaviour of poly-crystalline ice is highly anisotropic and regional variations in the relative proportions of shear and normal strain rates, which are driven by variations in the distribution of the stresses responsible for deformation, mean that spatial contrasts in anisotropy are common and widespread in ice sheets. For this reason, a spatially varying enhancement factor is required for ice sheet mod-elling ~~(e.g., Morgan et al., 1998; Wang et al., 2002a)~~ (e.g., Morgan et al., 1998; Wang and Warner, 1999; Wang et al., 2002a) .

Comparisons of simulations of ice sheet dynamics using ESTAR and the Glen flow relation will be influenced by: the choice of the Glen enhancement parameter, E_G; the ESTAR parameters E_C ~~:~~ and E_S; and the spatial distribution of λ_S. The most significant differences between Glen- and ESTAR-based simulations are expected where there are regional contrasts in λ_S. Specific regions where these conditions are likely to arise include: the progression with increasing depth in the ice sheet from a regime of normal stresses to one dominated by bed parallel shear; the contrasts between lateral margins of embayed ice shelves and ice streams ~~; locations where there are changes in dynamic conditions at the bed, e.g., at the transition between bed-parallel shear and basal sliding; ice shelf grounding zones;~~ and their central flows; and where there is significant relief in the bedrock topography.

A caveat is that as stated earlier, for ESTAR the assumptions of crystallography and deformation rates being compatible with the instantaneous stress/deformation regime requires that this does not change too rapidly along the flow. That is to say, for a compatible (tertiary) anisotropy to be present, the present deformation regime needs to be a suitable indicator of the recent strain history of the flowing ice.

3 Implementation of ESTAR

The magnitude of the shear strain rate defined on the local non-rotating shear plane, $\dot{\varepsilon}'$ ~~from~~ for Eq. 6, is central to the formulation of ESTAR ~~.~~ (Eqs. 3-4). The full prescription, following Budd et al. (2013), involves the ~~following~~ expression

$$\dot{\varepsilon}' = \|\dot{\boldsymbol{\varepsilon}} \cdot \mathbf{n} - (\mathbf{n} \cdot (\dot{\boldsymbol{\varepsilon}} \cdot \mathbf{n})) \mathbf{n} - (\hat{\boldsymbol{\omega}}_D \cdot (\dot{\boldsymbol{\varepsilon}} \cdot \mathbf{n})) \hat{\boldsymbol{\omega}}_D\|, \tag{7}$$

where: $\mathbf{n}$ is the unit normal to the non-rotating shear plane, $\hat{\boldsymbol{\omega}}_D$ is the unit vector parallel to that part of the vorticity that is associated solely with deformation $(\boldsymbol{\omega}_D)$, and $\dot{\boldsymbol{\varepsilon}}$ is the strain rate tensor. The unit normal to the non-rotating shear plane, $\mathbf{n}$, is defined as the normalised cross product of the velocity and the deformational vorticity

$$\mathbf{n} = \frac{\mathbf{v} \times \boldsymbol{\omega}_D}{\|\mathbf{v} \times \boldsymbol{\omega}_D\|}. \tag{8}$$

The last projection term in Eq. 7 was proposed in Budd et al. (2013) to prevent any shear component parallel to the defor-mational vorticity from contributing to the measure of simple shear.

The vorticity of a flow, whether viewed as the anti-symmetrised part of the velocity gradient tensor or as the usual vector $\boldsymbol{\omega} = \nabla \times \mathbf{v}$, contains motions associated with both deformation and local rigid-body rotation. The locally non-rotating shear

plane is intended to be rotating with any rigid rotation portion of the flow field, so it is only vorticity associated with the deformation process that is relevant to determining the shear fraction. Accordingly we formally decompose vorticity into deformational and rotational parts:

$$\boldsymbol{\omega} = \nabla \times \mathbf{v} = \boldsymbol{\omega}_D + \boldsymbol{\omega}_R. \tag{9}$$

5   For the present implementation it is convenient to decompose the vorticity further, into vectors perpendicular and parallel to the velocity direction as follows:

$$\boldsymbol{\omega} = \boldsymbol{\omega}_D^{\perp} + \boldsymbol{\omega}_R^{\perp} + \boldsymbol{\omega}_D^{\parallel} + \boldsymbol{\omega}_R^{\parallel}. \tag{10}$$

From Eq. 8, only the perpendicular projection $\boldsymbol{\omega}_D^{\perp}$ of the deformational vorticity is relevant in determining the direction of the normal to the non-rotating shear plane. This is fortunate since the perpendicular projection of the rotational vorticity can be

10   calculated directly for steady flow from the flow speed and the curvature of the local flowline, and is oriented along the bi-normal to the flow-line. The decomposition of the component of vorticity parallel to the flow direction, conventionally termed swirling motion, into deformational and rotational pieces is not so straightforward, but we can use the following expression, which can be calculated using variables available within an individual element of ISSM to generate a vector suitable for computing $\mathbf{n}$:

15    $$\tilde{\boldsymbol{\omega}}_D = \nabla \times \mathbf{v} - \frac{2\mathbf{v} \times ((\mathbf{v} \cdot \nabla)\mathbf{v})}{\|\mathbf{v}\|^2}. \tag{11}$$

This vector contains the correct perpendicular component $\boldsymbol{\omega}_D^{\perp}$ to compute $\mathbf{n}$ using Eq. 8, but contains all of $\boldsymbol{\omega}_D^{\parallel} + \boldsymbol{\omega}_R^{\parallel}$. We can obviously also project out the component parallel to velocity to find

$$\boldsymbol{\omega}_D^{\perp} = \tilde{\boldsymbol{\omega}}_D - (\mathbf{v} \cdot \tilde{\boldsymbol{\omega}}_D)\frac{\mathbf{v}}{\|\mathbf{v}\|^2}. \tag{12}$$

In the present implementation of ESTAR, we assume that swirling effects are small for flows with the relevant spatial scales,

20   aspect ratios etc., which can be verified from the modelled flow-fields in our test cases, and hence $\boldsymbol{\omega}_D^{\parallel}$ is also expected to be small. We use the unit vector corresponding to $\boldsymbol{\omega}_D^{\perp}$ (i.e., $\hat{\boldsymbol{\omega}}_D$) in Eq. 7 for our computation of $\dot{\varepsilon}'$. This corresponds to extracting the component of the shear resolved on the non-rotating shear plane which is parallel to the velocity direction, which could be regarded as an alternative generalisation for the simple shear to that proposed by Budd et al. (2013). No approximation is involved for flows that are exactly two dimensional in character, since vorticity is always orthogonal to velocity in such

25   situations.

     The ESTAR description above is implemented in ISSM for the full-Stokes (FS) model of flow. We also extended the implementation of ESTAR to ISSM versions of the higher-order (HO) three-dimensional model of Blatter (1995) and Pattyn (2003), and the shallow-shelf approximation (SSA) of MacAyeal (1989). The HO model is derived from the FS model by assuming that horizontal gradients in the vertical velocities are negligible ($\partial v_z/\partial x = \partial v_z/\partial y = 0$) compared with vertical gradients in the

30   horizontal velocities when computing vertical shear, and longitudinal derivatives of vertical shear stress (bridging effects van der Veen and V ignored. The HO vertical velocities are recovered directly through incompressibility. Extending on the HO model assumptions,

for the SSA model, vertical shear is assumed to be negligible ($\dot{\varepsilon}_{xz} = \dot{\varepsilon}_{yz} = 0$). For both the HO and SSA models, the approximations will affect calculations of the total vorticity and hence the magnitude of the shear strain rate on the non-rotating shear plane (Eq. 7) and λ_S (Eq. 6).

4 Analytical verification

5   We perform convergence tests in order to verify the ~~ISSM~~ implementation of ESTAR within the ~~full Stokes (FS) and higher order (HO)~~ ISSM FS and HO models. The objective of these tests is to compare the model results to analytical solutions for different mesh resolutions. As the mesh becomes finer, the error between the model and the analytical solution (i.e., $\sqrt{\int_\Omega (X - X_a)^2 / \int_\Omega X_a^2}$, for model solution X, analytical solution X_a, and domain Ω) should decrease, with a cubic dependence on resolution for FS (quadratic for ice pressure) when using Taylor-Hood finite elements, and a quadratic dependence

10   for HO using P1×P1 finite elements (e.g., Ern and Guermond, 2004).

We designed our analytical solutions by considering a three-dimensional, grounded, isothermal ice slab of unit dimension lying on a flat bed topography, with cartesian coordinates (x, y, z), where z is vertically upward and where there is no gravitational force. The FS three-dimensional velocity field is given by

$$v_x(x,y,z) = 3z, \tag{13}$$

15    $$v_y(x,y,z) = 2x + y, \tag{14}$$

$$v_z(x,y,z) = -z, \tag{15}$$

and the HO velocity field by

$$v_x(x,y,z) = x^2, \tag{16}$$

$$v_y(x,y,z) = 3z + y. \tag{17}$$

20   In the case of the HO model, $v_z(x,y,z)$ is recovered by incompressibility. For both FS and HO models, we use ESTAR shear and compression enhancement factors of $E_S = 3$ and $E_C = 1$, and the flow parameter $A(T') = 2/3 \, \mathrm{Pa}^{-3} \, \mathrm{s}^{-1}$. The open source mathematics software system SageMath (http://www.sagemath.org/) is used to calculate analytical solutions for the force balance equations based on the above velocity fields:

$$f_x(x,y,z) = -\left(\frac{\partial \sigma'_{xx}}{\partial x} + \frac{\partial \sigma_{xy}}{\partial y} + \frac{\partial \sigma_{xz}}{\partial z} \right), \tag{18}$$

25    $$f_y(x,y,z) = -\left(\frac{\partial \sigma_{xy}}{\partial x} + \frac{\partial \sigma'_{yy}}{\partial y} + \frac{\partial \sigma_{yz}}{\partial z} \right), \tag{19}$$

$$f_z(x,y,z) = -\left(\frac{\partial \sigma_{xz}}{\partial x} + \frac{\partial \sigma_{yz}}{\partial y} + \frac{\partial \sigma'_{zz}}{\partial z} \right). \tag{20}$$

Here, the deviatoric stress fields are calculated using ESTAR as specified in Eq. 3. When the total, rather than ~~deformation~~ deformational, vorticity (i.e., without inclusion of the rigid body correction or removal of the vorticity component aligned with the flow) is

10

used in the calculation of ESTAR, the FS analytical solution for (f_x, f_y, f_z) comprises (20 521, 9 190, 20 523) characters. By contrast, non-trivial analytical solutions for the forcing functions that are calculated from an anisotropic enhancement factor that is based on the ~~deformation~~deformational, rather than total, vorticity are at minimum 200 000 characters, well in excess of the character limits for most compilers. ~~Hence~~Accordingly, we verify ESTAR using the total, rather than the deformational, vorticity.

To test the numerical implementation of ESTAR, ISSM is forced using the analytical expressions for f_x, f_y, and f_z in Eqs. 18-20 and the resulting three-dimensional flow field is compared with the relevant analytical specification in Eqs. 13-17. Since the aim is to verify correct coding of the ESTAR modifications within ISSM, we apply the analytic velocities on the faces as the boundary conditions. Four sets of element sizes are used for each of the FS and HO models, increasing in resolution from 0.2 (272 elements over 5 vertical layers) to 0.08 (4656 elements over 13 vertical layers). We find convergence powers of 2.5 (v_x), 3.1 (v_y), and 2.6 (v_z) for FS, respectively, and 1.4 (v_x) and 1.1 (v_y) for HO (Fig. 2), which are consistent with theory and verify our implementation.

5   Application of ESTAR to idealised scenarios

ESTAR was applied to a suite of test cases. The first case we present simulates flow in an embayed ice shelf; the second two are based on experiments from the Ice Sheet Model Intercomparison Project for Higher Order Models (ISMIP-HOM; Pattyn et al., 2007). The ISMIP-HOM experiments describe idealised scenarios of ice flow where the bed topography or basal friction vary. ISSM has already been validated against ~~each of these~~ the ISMIP-HOM experiments (Larour et al., 2012).

In each experiment, the velocity, surface, and thickness fields were allowed to run to steady-state, as defined in ~~each section~~ the corresponding section below (the original ISMIP-HOM experiments were simply diagnostic). The ice sheet is isothermal in each case.

As mentioned ~~in the previous section~~above, we use ESTAR shear and compression enhancement factors of $E_S = 8$ and $E_C = 3$, respectively (Treverrow et al., 2012). For each experiment, we ~~perform simulations using~~ performed simulations using a range of Glen enhancement factors ~~of~~ (1, 3, 5, and 8~~; this range of enhancement factors facilitates a 1:1 comparison with ESTAR for different governing stress regimes, yet remains consistent with the broad range of enhancement factors used in previous ice sheet model experiments (e.g., Greve, 1997; Parizek and Alley, 2004; Tarasov and Peltier, 2004; Martin et al., 2011)~~), but since these idealised experimental systems have simple scaling properties under global changes in flow rates, we present only results for $E_G = 8$ since that proved the most directly relevant value. The ISMIP-HOM experiments used the ~~same~~ original parameter values (Pattyn et al., 2007) unless otherwise indicated.

5.1   Flow through an embayed ice shelf

The first experiment simulates three-dimensional flow through a rectangular embayed ice shelf. The experiment was carried out for model domains with transverse spans $x \in [0, L]$, for $L = 20$, 60, and 100 km and along-flow dimension $y \in [0, 100]$ km. The initial ice thickness decreases uniformly from 1000 m at the grounded zone to 300, 600, and 850 m at the ice front for

the $L = 20$, 60, and 100 km cases, respectively. The main features of the anisotropic effects are similar regardless of aspect ratio~~, so~~. This is principally because wider embayed ice shelves are flatter so that the influence of simple shear stresses on the dynamics is not particularly sensitive to aspect ratio. Accordingly, we focus our discussion on one transverse length scale: $L = 20$ km. The plan view mesh is extruded ten quadratically-spaced layers in the vertical. A no-slip boundary condition is

5   applied along the $x = 0$ and $x = L$ side boundaries. At the inflow boundary, the y-component of velocity is set to

$$v_y(x,0) = V_0 e^{-\left[\frac{5(x-x_{\mathrm{mid}})}{2L}\right]^8}, \tag{21}$$

where $V_0 = 100$ m yr^{-1} and $x_{\mathrm{mid}} = L/2$. As is standard, ocean water pressure is applied at the ice-ocean interface where tangential (traction) stresses vanish. It is assumed that there is no surface or basal melting or accumulation over the ice shelf domain. The flow parameter $A(T') = 1.74 \times 10^{-25}$ Pa^{-3} s^{-1}, is set using the Budd and Jacka (1989) value for an isothermal

10   ice shelf of $-20\,°$C. We consider the case where the Glen enhancement factor is equal to the ESTAR shear enhancement factor, i.e., $E_G = E_S = 8$.

We run the HO ice flow model for each of the ESTAR and Glen rheologies to steady-state, which we define to be reached when the mean velocity change over the surface mesh points is less than 1×10^{-2} m yr^{-1} between two consecutive time steps (of $\triangle t = 2$ yr). ~~ISSM uses the Blatter-Pattyn form of the HO approximation (Blatter, 1995; Pattyn, 2003), which assumes that~~

15   ~~horizontal gradients in the vertical velocities are negligible compared with vertical gradients in the horizontal velocities when computing vertical shear, and longitudinal derivatives of vertical shear stress (bridging effects) are ignored.~~

The Glen and ESTAR HO steady-state surface velocity magnitudes are compared in Fig. 3~~, where a Glen enhancement factor of $E_G = 8$ has been used~~. The patterns of ice flow are similar for the two rheologies: in each case the ice velocity increases as it flows through the ice shelf, reaching its maximum at the ice front. Over most of the domain the velocities are in close

20   agreement, reflecting the dominance of the shear flow. However, the Glen velocities are up to 17% larger than the ESTAR velocities at the ice front, where the flow field is predominantly extensive in accordance with the ice front boundary conditions. The differences in velocities can be attributed to differences in flow enhancement factors for simple shear and compression. ~~In the centre~~ Near the centre line of the ice shelf and across the ice front, where longitudinal and vertical normal stresses dominate, the Glen enhancement is as much as $8/3$ times larger than the corresponding ESTAR enhancement.

25   The steady-state thickness ratio for the two rheologies is shown in Fig. 3d. In both cases, the equilibrated ice shelf is thicker along the centre line and thinner towards the side margins where ice flow is slower, and thicknesses agree within 5% over much of the domain. However, the Glen ice shelf is consistently thinner than the ESTAR ice shelf, particularly along the centre line where Glen velocity is enhanced relative to ESTAR, and it is up to 20% thinner at the ice front. ~~Reducing the Glen enhancement factor (i.e., for $E_G = 1,3,5$) results in almost identical steady-state velocities to the $E_G = 8$ case. However, the~~

30   ~~ice shelf thicknesses for $E_G = 1,3,5$ are then uniformly greater across the shelf than the $E_G = 8$ case by approximately 100%, 40%, and 17%, respectively.~~

The ESTAR strain rate components are presented in Fig. 4. As expected, shear strain rate in the $x - y$ plane is very high near the lateral boundaries (Fig. 4d). However, it dominates the effective strain rate (and hence λ_S) well beyond those margins (Fig. 5), before decreasing towards the centre line, where it identically vanishes. Towards the ice-ocean front, each of the normal

strain rates – $\dot{\varepsilon}_{xx}$, $\dot{\varepsilon}_{yy}$, and $\dot{\varepsilon}_{zz}$ – increase in magnitude, reaching their maxima at the front. The (approximately) longitudinal $\dot{\varepsilon}_{yy}$ is the dominant normal strain rate component and is extensive towards the front. Due to the confined geometry, towards the front $\dot{\varepsilon}_{yy}$ is largely balanced by $\dot{\varepsilon}_{zz}$, which drives ice shelf thinning. Transverse normal strain rate $\dot{\varepsilon}_{xx}$ plays a lesser role at the ice-ocean front than the ~~remaining~~ other normal strain rates. It is extensive along the front as the streamlines diverge,

5 but changes sign to compressive towards the corners. The patterns in the component strain rates, including the dominance of ~~vertical compression~~ normal strain rates in the centre of the ice shelf and at the ice-ocean front, are evident in the strain rate on the non-rotating shear plane (~~NRSP strain rate~~ $\dot{\varepsilon}'$) and the effective strain rate ($\dot{\varepsilon}_e$~~; Fig. 5~~), the ratio of which sets the magnitude of λ_S ~~.~~ (Fig. 5). In the ESTAR embayed ice shelf simulation, the vanishing of basal traction and the depth independent nature of the inflow velocity lead to an almost 2D flow field with local non-rotating shear planes essentially vertical where they can

10 be defined – there being neither $x - y$ plane shear nor vorticity along the centre line. We note that $\dot{\varepsilon}_{yy}$ decreases in magnitude with depth at the ice-ocean front, coincident with ice front tilting (Weertman, 1957), which also gives rise to some local shear deformation in the $y - z$ plane.

~~The~~ To assess the computational demands of the full ISSM model with ESTAR, the FS ice flow model was computed for ~~1~~ one model year (i.e., steady state had not yet been reached) and the results compared with the HO simulation results for the

15 same model period (results not shown). At the ice front, the HO velocities are everywhere within 5% of the FS velocities, with the maximum differences occurring near the lateral boundaries. Across the shelf, the HO component velocities accord well with the FS velocities. The magnitude and spatial patterns of $\dot{\varepsilon}'$, $\dot{\varepsilon}_e$, and λ_S also agree well between the ~~two flow equations~~ FS and HO models.

Computation times for FS simulations using each of the two rheologies, and for increasing mesh resolutions, are summarised

20 in Table 1. In each case, the model was run for 1 month with a time step of $\triangle t = 1 \times 10^{-4}$ yr. The ESTAR simulation computation times are no more than 3% slower than the corresponding Glen times, and the simulation times for the two rheologies converge as the mesh resolution increases. This result gives us confidence that ESTAR is essentially as computationally-efficient as the Glen rheology.

5.2 ISMIP-HOM experiment B: two-dimensional flow over a bumpy bed

25 ISMIP-HOM Experiment B (ISMIPB) describes two-dimensional flow (x horizontal, z vertical) over a bed topography that varies sinusoidally, according to the following equation

$$z_b(x) = z_s(x) - 1000 + 500 \sin\left(\frac{2\pi x}{L}\right). \tag{22}$$

where $z_s(x) = -x \tan \alpha$, for a mean bed slope of $\alpha = 0.5°$, and L controls the scale of the bedrock undulation. We take $z_s(x)$ as the initial surface so that the mean initial ice thickness is 1000 m. ~~As for the embayed ice shelf experiment, we discuss only~~

30 ~~the~~ We present results for two different aspect ratios, $L = 20$ ~~case since the anisotropic effects are similar regardless of aspect ratio~~ km and $L = 5$ km, to explore the influence of different longitudinal stresses. In each case we used the full-Stokes (FS) version of ISSM. The flow parameter is fixed at 3.96×10^{-25} Pa^{-3} s^{-1}, corresponding to an ice temperature of approximately $-14°$ C (Budd and Jacka, 1989). The value for the flow parameter in the original ISMIPB was 3.17×10^{-24} Pa^{-3} s^{-1}, which

corresponds to a Budd and Jacka (1989) ice temperature of approximately $-3.6°$ C. We have reduced the original flow parameter by a factor of 8 (i.e., equal to E_S) to ensure our results are as close as possible to the original ISMIP-HOM experiments. Periodic boundary conditions are applied at the vertical edges of the domain and a no-slip boundary condition is applied at the base. In this and the following two-dimensional test case, the normal to the non-rotating shear plane is simply the direction perpendicular to the velocity and there is no uncertainty about the vorticity (which has only one non-vanishing component) being perpendicular to the velocity. Steady-state is regarded as reached when the mean velocity change over the surface mesh points is less than 1×10^{-2} m yr^{-1} between two consecutive time steps of $\triangle t = 1$ yr for this and the following ISMIP-HOM experiment.

In what follows, we consider the case when the Glen enhancement factor is equal to the ESTAR shear enhancement factor, i.e., $E_G = E_S = 8$. This is the most relevant case for the ISMIPB experiment as the dynamics here are driven by bed-parallel shear, as discussed below.

The ESTAR and Glen FS steady-state ~~along-flow~~ horizontal velocities (v_x) ~~are compared~~ for ISMIPB for $L = 20$ km are shown in Fig. ~~??~~ ~~and the shear fraction~~ 6a and b, with their ratio in Fig. 6c. The shear fraction (λ_S) used to calculate the ESTAR enhancement is shown in Fig. ~~??a. When $E_G = E_S = 8$, the~~ 6d. The ESTAR velocities are marginally slower than the Glen velocities throughout the domain, regionally by as much as 6%. ~~Although, we note that~~ While in a real-world situation, a local difference of 6% may not be significant to overall flow, clearly unless the Glen enhancement factor is approximately E_S there would be a significant and widespread difference in velocities. One major contrast occurs either side of the topographic bump in the near-surface layers (Fig. ~~??~~6c) where normal stresses dominate ($\lambda_S < 1$ ~~) and E_G is greater than E_C (;~~ Fig. ~~??) .~~ 6d) and $E(\lambda_S)$ tends to $E_C < E_G$, as λ_S tends to 0. This reduces the shear deformation in the upper-layers for ESTAR compared to Glen, leading to slightly lower horizontal velocities ~~. Another~~ near the surface. We will discuss the relevance of this in Sect. 6. Another major velocity contrast occurs in the lowest part of the ice sheet directly above the topographic depression. Since deformation here is clearly shear dominated ($\lambda_S = 1$ ~~; Fig. ??~~ for essentially the whole column), the ~~difference~~ differences must arise from a varying but consistently lower shear stress profile in the ESTAR case, reflecting indirectly the distributed effect of the stiffer ice in the upper layers ~~because $E(\lambda_S) < E_G = 8$.~~ where $E(\lambda_S) < E_G$ and a slightly different final geometry of the ice surface. In contrast, the closest agreement between the two velocity distributions is in the basal region over the topographic high.

Figure ~~??~~ 6 also shows the FS ~~shear and normal~~ $\dot\varepsilon_{xz}$ and $\dot\varepsilon_{xx}$ strain rates for the ESTAR simulation: effectively the shear and normal strain rates. The dominance of high values of λ_S indicates that bed-parallel simple shear is the main driver of ice flow in ISMIPB with the expected transition through the ice column from compression/extension-dominated flow near the surface to shear-dominated flow near the non-slip bed. Note that while ~~our~~ the component strain rates are ~~locked into a global~~ presented in the background cartesian frame, λ_S denotes the relative importance of simple shear on local non-rotating shear planes. ~~High shear peaks~~ Peaks in λ_S appear directly over the topographical bump and depression, extending further into the surface layers than in surrounding regions. The locations of the peaks ~~correspond to~~ in λ_S correspond to the transitions between extensive and compressive longitudinal stresses, centred on "transition curves" (Fig. 6e), along which normal strain rates are identically zero ~~at some point.~~ .

In addition to the case where $L = 20$ km, we also investigated the impact of reducing the horizontal extent to $L = 5$ km. In this steeper bed scenario (Fig. 7), the ESTAR surface velocities are at least 11% slower than the Glen velocities in the surface layers across the whole domain, as much as 20% slower around the topographic bump, and up to 25% slower in the topographic depression (Fig. 7c). The much greater reductions in the magnitude of the ESTAR velocities for $L = 5$ km are a consequence of the increasing importance of longitudinal stresses in the stress balance equations for the smaller aspect ratio (Fig. 7e), and also in some areas the lower strain rates, which lead to correspondingly stiffer ice. Indeed we see a clear decline in the shear strain rate in the lower part of the bed depression in Fig. 7f, in contrast to Fig. 6f. The qualitative pattern of the longitudinal strain-rates in Fig. 7e is similar to the $L = 20$ km case, although the horizontal gradients are naturally accentuated, and the "transition curves" are displaced.

In order to examine the dynamics giving rise to the high ~~shear peaks~~ shear-dominance peaks in Fig. 6d and Fig. 7d, we consider the following exact form of λ_S^2 (for ~~this~~ these two-dimensional flow ~~field) expressible in~~ fields) expressible using the cartesian frame strain rate components

$$\lambda_S^2 = \frac{\alpha \dot{\varepsilon}_{xx}^2 + \beta \dot{\varepsilon}_{xz}^2 + \gamma \dot{\varepsilon}_{xx}\dot{\varepsilon}_{xz}}{\dot{\varepsilon}_{xx}^2 + \dot{\varepsilon}_{xz}^2}, \tag{23}$$

for some spatially varying coefficients α, β, and γ. Since there is no surface accumulation, velocities and hence local non-rotating shear planes at the ice sheet surface are parallel to the ~~ice sheet~~ surface. The traction free surface boundary condition implies ~~$\lambda_S = 0$ there,~~ that the numerator ($\dot{\varepsilon}'^2$) in Eq. 23, and accordingly λ_S, vanishes at the surface, except that if $\dot{\varepsilon}_e$ also vanishes, λ_S is technically undefined. ~~We set~~ Our implementation sets $\lambda_S = 0$ for vanishing $\dot{\varepsilon}'$ in such situations. It is apparent from Eq. 23 that along the transition curves, i.e., where $\dot{\varepsilon}_{xx} = \dot{\varepsilon}_{zz} = 0$, $\lambda_S^2 = \beta$, independent of (non-zero) $\dot{\varepsilon}_{xz}$ strain rate. ~~We find~~ One can show that $\beta \to (1 - S_x^2)^2$ towards the surface (i.e., for surface slope in the x-direction S_x) along the transition curve, in order to satisfy the surface boundary condition. This indicates that λ_S ~~should~~ would be finite along the transition ~~curve~~ curves all the way to the surface. ~~The fact that $\lambda_S \to 0$ along the transition curves towards the surface in Fig. ?? may also be a consequence of mesh averaging over elements such that there is not necessarily an exact point in our finite mesh for which $\dot{\varepsilon}_{xx}$ is identically equal to 0.~~, except that we enforced its vanishing there. For these locations, the Glen and ESTAR viscosities corresponding to Eqs. 2-3 would tend to infinity as $\dot{\varepsilon}_e$ vanished approaching the surface, but are limited to a maximum value in the ISSM implementation.

Note that away from the transition curves λ_S ~~does go to zero at~~ goes to zero as we approach the surface, associated with vanishing shear on the non-rotating shear plane ~~there.~~

~~The FS spatial pattern of velocities is consistent for both ESTAR and Glen using each of the Glen enhancement factors $E_G = 1, 3, 5, 8$. Naturally, the Glen velocities decrease with decreasing enhancement factor (as the ice becomes stiffer): for $E_G = E_C = 3$, the Glen velocity magnitudes are 38-40% of the corresponding ESTAR velocities; for $E_G = 1$, Glen velocities are only 16-17% of the corresponding ESTAR velocities. These results indicate that the velocities in the Glen case scale exactly with the choice of E_G. This follows from the nature of the boundary conditions here, so that one can rescale velocity to compensate for changes in E_G.~~

~~In addition to the ESTAR FS simulation of ISMIPB, we performed an HO simulation to investigate the representation of anisotropic flow in that approximation scheme. Figure **??** compares velocities, shear fractions λ_S, and anisotropic viscosities, and their ratios, between HO and FS simulations. The HO velocities are slower than the FS velocities throughout the domain. Generally, this is attributable to the neglect of strain rate components – notably the horizontal gradient of vertical velocity – in~~ the HO force balance equations, leading to stiffer ice in the HO approximation. The maximum differences between the HO and FS velocities occur in the basal layers. Consistent with Pattyn et al. (2008) , in the and the corresponding dominance of normal deformations. We return to these near-surface ~~layers, HO velocities are everywhere within 3% of the FS velocities, with larger differences between HO and FS velocities directly over the topographic bump and depression. The differences between HO and FS velocities are magnified in the near-surface layers over the topographic bump relative to the topographic depression. In combination with the neglect of strain rate components in the HO approximation, this difference arises due to slight differences in the locations of vanishing longitudinal strain rates. The local viscosity maxima in the near-surface layers also correspond to regions of vanishing longitudinal strain rates. For these locations, the Glen viscosities would be infinite, but are limited to a maximum value in the ISSM implementation.~~ spikes in λ_S in the discussion.

5.3 ISMIP-HOM experiment D: two-dimensional flow over a sticky spot

ISMIP-HOM experiment D (ISMIPD) describes a two-dimensional domain over which the basal friction coefficient $~~\eta~~ \chi$ varies sinusoidally in the horizontal direction. A Paterson-type friction law (Paterson, 1994) of the following form is used

$$\tau_b = -\underline{\eta}\underline{\chi}^2 v_b, \tag{24}$$

where τ_b is the basal stress and v_b the basal velocity, and $~~\eta~~$ the friction coefficient, χ^2 (Pa a m^{-1}), varies according to the equation

$$\underline{\eta}\chi^2 = 1000 + 1000 \, \sin\left(\frac{2\pi}{L}x\right). \tag{25}$$

The bed topography and the initial ice surface are inclined planes with a slope of $0.1°$, and the initial thickness is 1000 m throughout the domain. As ~~before~~ in the preceding ISMIPB experiments, the flow parameter is taken as $A(T') = 3.96 \times 10^{-25}$ Pa^{-3} s^{-1} (the ISMIPB and ISMIPD original flow parameters were equal). Periodic boundary conditions are applied at the edges of the domain.

~~First, the Glen and ESTAR FS stress balance (diagnostic) results for ISMIPD are compared (upper panels, Fig. 8). Note that applied stresses from the initial slope are uniform for this solution type. Along-flow velocities (v_x) are lowest over the sticky spot (0-10), and greatest over the slippery spot (10-20)~~ Once again, we present results for steady-state solutions for two different horizontal scales: $L = 20$ km and $L = 5$ km. As with the ISMIPB experiments above, we employ the full-Stokes (FS) solver in ISSM. Consistent with ISMIPB, the control of the final deformation flow in the ISMIPD experiment is bed-parallel shear, so we consider the case when the Glen enhancement factor is equal to the ESTAR shear enhancement factor, i.e., $E_G = E_S = 8$. ~~However, the contribution from the deformation flow is the other way around since there is negligible vertical shear where the basal friction vanishes. The Glen isotropic and ESTAR anisotropic viscosities in the basal layers directly over~~

~~the sticky spot are approximately equal , but towards the surface the ESTAR ice becomes stiffer over the sticky spot.By contrast, over the slippery spot, the ESTAR ice is on average 1.8 times stiffer than the Glen ice (see λ_S~~

The Glen and ESTAR FS results for ISMIPD when $L = 20$ km are shown in Fig. 9a)~~, leading to ESTAR velocities that are up to 10% slower there. For the deformation velocities alone, the maximum difference between the ESTAR and Glen velocities~~

5 ~~occurs over the sticky spot where ESTAR velocities are up to 7% faster (ignoring the region over the slippery spot where both the ESTAR and Glen deformation velocities are identically zero).~~

~~We next consider the FS prognostic results for Glen and ESTAR. Over the sticky spot, vertical shear develops, leading to faster velocities~~ 8. For both rheologies, the fastest velocities develop in the upper part of the column ~~(Fig. 8d~~over the sticky spot (centred around 5 km). This is required by continuity, given the ~~low~~ lower basal velocities over the sticky spot, to

10 balance the block flow over the slippery section ~~. Sliding occurs throughout the domain.~~ (basal friction coefficient vanishes at 15 km). The basal velocities increase ~~over the interval where the~~ as the basal friction coefficient decreases~~, with a corresponding adjustment in the upper layer velocities. This is part of the transition to block flow over the slippery spot.~~

~~With a Glen enhancement factor equal to the ESTAR shear enhancement factor, the total Glen FS~~. The total steady-state ESTAR velocities are everywhere within 1% of the corresponding ~~ESTAR velocities~~ Glen velocities (see Fig. 8c), with the

15 maximum difference occurring in the near-surface layers over the sticky spot~~(0-5)~~, where the ESTAR ice is stiffer, as shown by the corresponding contrast in viscosities (Fig. ~~9). The~~ 8e). Sliding occurs throughout the domain and the deviations from block flow are modest throughout, so to explore what differences might be associated with the departure from block flow we calculated "deformational velocities" from v_x by subtracting the basal motion, and examined the ratio between ESTAR and Glen cases (Fig. 8d). The most notable feature of this ratio is a localised 50% decrease in deformational velocity for ESTAR

20 compared to Glen through the entire column, peaking directly over the point where the basal friction coefficient (Eq. 25) vanishes. This major band of difference coincides with the band of higher viscosity for ESTAR, relative to Glen, (see Fig. 8e) over the slippery region.

The ESTAR component strain rates and shear fraction λ_S are illustrated in Fig. 9 ~~. The distribution~~ for ISMIPD, for the $L = 20$ km case. The plot of λ_S ~~evolves primarily due to the evolution of normal stresses to steady-state. Shear dominates~~

25 (Fig. 9d) depicts transitions in the deformation regime from shear-dominated to compression/extension-dominated and back over a few kilometres around the slippery spot. These transitions extend all the way to the bed, becoming perpendicular to the ice flow direction and reflect the low shear over the slippery region. This is in marked contrast to the ISMIPB experiments, where the shear deformation regime dominated except near the free surface. We discuss the implications of these abrupt transitions for the assumptions that underpin ESTAR in the next section. Shear dominates much of the ice column ($\lambda_S > 0.5$)

30 throughout ~~most~~ the rest of the domain (~~i.e., for~~ over the region where values of the basal friction coefficient ~~>~~exceed 10% of the maximum value). ~~In~~ The shear strain rates are greatest in the region of maximum stickiness at approximately 5 km, ~~the shear stresses are greatest, while in the near-surface layers longitudinal stresses develop either side of the sticky spot.~~

~~In examining the evolution of the FS strain rates to steady-state, the shear is largely unchanged although a steeper profile develops over the sticky spot, while longitudinal normal strain rates are reduced by about an order of magnitude over most of~~

35 ~~the domain~~and a steep profile in the shear strain rate is present there. Naturally, ~~a compressive to extensive transition occurs~~

~~across~~ transitions between extensive and compressive flows occur around the sticky spot and the transition curves (vanishing normal strain rates) ~~now~~ resemble the ISMIPB ~~case~~ cases (Fig. ~~??b)~~ ~~rather than their diagnostic starting point (Fig. 9b)~~ 6e). ~~The change in the normal strain rates increases the vertical extent of the shear enhancement~~ Here the transition curves reach the surface as the friction coefficient increases, and just downstream of its peak value (the sticky spot), leading to near surface spikes of high values λ_S analogous to ISMIPB. It should be noted that the strain rates here are very small compared to the ISMIPB experiments. The viscosity ratio in Fig. 8e reveals that there are also lower strain rates for ESTAR in the compression dominated regions, as the ratios there are higher than the factor of 1.39 that would be produced by the influence of $E(\lambda_S)$ alone.

The results of a FS prognostic run to steady-state for the ISMIPD experiment for $L = 5$ km are presented in Fig. 10. The v_x velocity ratio (Fig. ~~9d) , except over the slippery spot.~~ 10c) shows that very little difference is seen between results for the two flow relations, unlike the ISMIPB experiments in the previous section, where differences up to 25% between ESTAR and Glen cases emerged for the shorter bedrock periodicity. The tiny differences in overall velocities are enhanced but the patterns in Fig. 8c and Fig. 10c are similar. However, there is a significantly different picture in the ratio of deformation velocities seen in Fig. 10d, compared to Fig. 8e. The largest differences are now limited to the lower portion of the ice column and for much of the region over the slippery bed the ratio is almost unity.

The pattern of deformation regimes mapped by λ_S (Fig. 10f) is also more complex than that seen in the preceding $L = 20$ km case (see Fig. 9d). The general structure of the normal strain rates is similar to previous experiments, but here the persistence of a band of shear (Fig. 10h) above the slippery spot at intermediate depths prevents the establishment of a vertical block of flow dominated by normal stresses. The shear profile above the sticky spot is also much weaker in the upper layers. Accordingly, λ_S reveals a band of unevenly shear-dominated deformation which is continuous across the periodic domain. Once again, shear dominated spikes extend towards the surface in association with the vanishing of the normal strain rates.

The spatial variations in the viscosity ratio (Fig. 10e) depart significantly from those of λ_S, reflecting more strikingly than for $L = 20$ km (Fig. 8e) the combined influence of the pattern of enhancement (controlled by $E(\lambda_S)$) and the effect of different strain rates, with values both above and below the range (1.0-1.39) directly controlled by $E(\lambda_S)/E_G$.

6 Discussion

~~The ISMIP-HOM experiments B and D simulated scenarios in which the dominant control of flow was bed-parallel simple shear. Only small differences ($< 6\%$ for ISMIPB and $< 1\%$ for ISMIPD) were apparent between the Glen and ESTAR velocities for a Glen enhancement factor equal to the ESTAR shear enhancement factor ($E_G = E_S$). These results suggest that close agreement with the ESTAR results might be achieved more generally by this choice of the Glen enhancement factor. The results provide a physical rationale to replace the ad hoc enhancement factors typically used in grounded ice sheet modelling. Nevertheless, there remain scenarios of ice flow over grounded ice with more complicated stress regimes than those simulated in the ISMIP-HOM experiments presented here (e.g. , ice stream flow with similar contrasts in shear dominated margins and normal stress dominated central regions; flow close to rugged bedrock topography where combinations of shear~~

~~and normal stressesmay be important; or, generally, regions in which λ_S demonstrates large spatial variations corresponding to different stress regimes)~~

In this study we conducted various ice flow simulations, comparing ESTAR with the isotropic Glen flow relation. ESTAR incorporates the observed differences between tertiary deformation rates for shear dominated and normal stress dominated stress regimes. ~~In these instances, tuning the Glen enhancement factor may not be able to adequately account for multiple, or varying, controls on ice velocities, nor will it necessarily result in a physically realistic enhancement factor.~~

Our simulations of embayed ice shelf flow ~~comparing ESTAR and isotropic rheology~~ showed that no single Glen enhancement factor (E_G) can ~~approximate~~ reproduce the anisotropic flow characteristic of the various stress regimes encountered. ~~Our most significant result indicated that for an embayed ice shelf,~~ Significantly, while a choice of $E_G = E_S$ was necessary to reproduce the ~~overall velocities~~same overall velocities and ice thicknesses, which are largely controlled by lateral shear, this overestimated velocities near the ice front by up to 17% compared to ESTAR. This is a consequence of ~~excessively soft ice for~~ softer ice in the Glen case ~~in~~ for the zone near the ice front~~where extensional normal~~, where extensional longitudinal stresses dominate. The steady-state Glen ice shelf was accordingly up to 20% thinner than the ESTAR ice shelf in this region. Even with this thinner ice influencing the ocean pressure boundary condition at the ice front, the softer ice in the Glen case meant that the longitudinal strain rates there were higher.

These results highlight one of the key failures of the Glen flow relation~~in adequately accounting~~: an inability to account for complex, spatially varying stress regimes in its prescription of ice flow. The addition of an enhancement factor E_G to the Glen flow relation ~~provides~~ permits some compensation for the flow enhancement associated with microstructural development (i.e., rescaling the minimum creep rate data conventionally used in prescribing the Glen flow relation, e.g., ~~table~~ Table 3.3, Cuffey and Paterson, 2010). However, such a modification does nothing to allow for the anisotropic (stress configuration dependent) aspects of ice rheology that are characteristic of tertiary creep. The improvement offered by ESTAR is that the specification of the pattern and degree of enhancement is physically based, varying spatially as a function of the stress configuration. This is achieved without the complication of a detailed treatment of microstructural information. ~~For near-surface regions of~~

The ISMIP-HOM experiments B and D simulated scenarios in which the dominant control of flow was bed-parallel simple shear. In the prognostic runs with the larger aspect ratio ($L = 20$ km), only small differences were apparent between the Glen and ESTAR velocities ($< 6\%$ for ISMIPB and $< 1\%$ for ISMIPD), again provided the Glen enhancement factor was chosen equal to the ESTAR shear enhancement factor ($E_G = E_S$).

For more rapidly varying bed topography in ISMIPB, with $L = 5$ km, the differences in velocity for the two flow relations reached 25%, with surface variations of 11%. For ISMIPD, which explored variations in basal friction, the ~~ice sheet, there may be some lag in the development of anisotropy that is not captured by ESTAR. However, in this zone, both stresses and temperatures are low , so the resulting deformation rates are also low. As such, it is unlikely that an over-enhancement in this zone will impact significantly on the overall dynamics of the ice sheet.~~ $L = 5$ km experiments still showed $< 1\%$ differences in velocities with very low strain rates, so that although a complex pattern of deformation regimes emerged, there was little effect on flow from the choice of flow relation.

These results suggest if major bed topography only varied on scales much longer than the ice thickness, close agreement between ESTAR and the Glen flow relation might be achieved more generally by choosing the tertiary shear enhancement factor as the Glen enhancement factor ($E_G = E_S$). This might provide a physical rationale to replace the *ad hoc* enhancement factors typically used in large-scale grounded ice sheet modelling with the value appropriate to flow dominated by simple
5 shear. However, larger differences between velocities and vertical shear profiles emerged for the more rapid bedrock variation, where the importance of including longitudinal stresses in the momentum balance is already recognised (Pattyn et al., 2008) , suggesting that adopting ESTAR would be preferable.

Our idealised test cases also provide some insights into the validity of the tertiary flow assumption underlying ESTAR, and the development of anisotropic crystal fabrics compatible with the current deformation regime. In the embayed ice shelf ~~results~~
10 ~~have significant implications for ice sheet model simulations that rely on the Glen flow relation to simulate past, present, and future ice flow, which are used to constrain uncertainty in reconstructions and projections of sea levels. In particular, the result of unrealistically fast thinning ice, as simulated with the Glen flow relation, is to deform an ice shelf~~test the most significant change in the deformation regime is clearly the transition to extensive flow on approach to the ice shelf front. The contours of λ_S here are relatively well aligned with the ice flow so that flowing ice experiences gradual changes in stress regime, and the
15 magnitudes of strain rates (e.g., Fig. 4b) and velocities (Fig. 3) indicate that in the region near the ice front, where the Glen and ESTAR results vary appreciably, a progression of essentially compatible fabrics would be maintained. Indeed, under the prevailing deformation and flow conditions these would even develop from random fabrics over a few km.

The ISMIP-HOM experiments reveal potential violations of the tertiary flow assumption, although the significance for the flow field of these apparent short-comings needs to be assessed with regard to the somewhat artificial nature of the tests. Indeed
20 as we saw, the difference between the ESTAR predictions and the Glen flow relations (provided $E_G = E_S$) was small, except for ISMIPB with $L = 5$ km, although of course ESTAR makes no claim to correctly describe the transient rheology of ice with an evolving anisotropy.

The ISMIP experiments have a spatial periodicity, which could ~~lead to unrealistic ice shelf geometries and affect buttressing if it were to spread beyond the "passive ice" sector (Furst et al., 2016) near the ice front. Our findings motivate further enquiry~~
25 ~~into the simulated ice sheet dynamics of glaciers,~~ allow one portion of the repetitive basal conditions to dominate the overall flow. Also, there is no surface mass budget in these experiments so that, as remarked earlier, the ice surface is a flow line, whereas in a system with surface accumulation fresh snow is always being added and advected down into the ice sheet where it makes the transition to solid ice. Accordingly, in the flow regime of these prognostic experiments even the surface layers would be regarded as having developed some anisotropy just as the lower layers would, since they have in principle been deforming
30 over an arbitrarily long time.

The main issue about the establishment of tertiary flow conditions in the periodic environment of our ISMIP experiments concerns the possible cycling of the flowing ice through a variety of stress regimes. This leads to transition regions where the stress regime and presumably the crystal anisotropy would be evolving, and the compatibility assumptions behind ESTAR could locally be violated. Clearly the spatial extent of transitional flow and the delay in attaining any new tertiary state depends
35 on the ~~flow of which is governed by anisotropy as captured in ESTAR rather than the Glen flow relation.~~ magnitudes of

the strain rates and the velocity of the ice. By combining these with a threshold for accumulated strain as the criterion for development of a compatible (tertiary) fabric under a persistent flow regime, the extent of a transition zone can be estimated. This scale can then be compared to the horizontal variation of the stress regime. Selecting the 10% strain required to develop a compatible anisotropy from initially randomly oriented ice should provide a conservative yardstick, when applied to gradual

5 changes in stress regime.

~~In order to measure the impact of an anisotropic rheology on simulated ice dynamics, the ISMIP-HOM and embayed iceshelf experiments were carried out assuming isothermal conditions. However, strong vertical gradients in temperature, where they exist, will be a stronger control on viscosity than the factor of $8/3$ in anisotropic enhancement. This is particularly relevant for the ISMIP-HOM experiments simulated here for simple shear dominated flow.~~ The patterns of stress regimes revealed by

10 the distributions of λ_S (Figs. 6d, 7d, 9a, and 10f) indicate where along-flow variations in stress regime might be too rapid to sustain the assumption that a compatible crystallographic anisotropy had evolved. For the ISMIPB experiments this concern is essentially focussed to the near surface spikes in λ_S around the two locations where longitudinal deformations vanish, since the anisotropy of deeper ice will be compatible with deformation dominated by simple shear. There may be some complications with a slow cycling of the upper levels between extensive and compressive flow. Very near the surface, the λ_S peak intervals are

15 narrow and the shear strain rates there are very small (corresponding to transition scales of several kilometres) so that there will be no appreciable development of a shear compatible fabric. Either side of the peaks, the main extensive and compressive flow domains for $L = 20$ km (see Fig. 6e) are ≈ 5 km long and have transition scales of < 1 km which suggests that the strongly normal stress dominated upper layer will be mainly in tertiary state. Turning to the transient shear intrusions into this layer: at 100 m depth over the bump the shear transition scale is 3 km while at 200 m depth over the depression the shear transition

20 scale is ≈ 5 km, suggesting that that the λ_S peaks do represent a local failure of ESTAR's tertiary assumption. Throughout the domain the lower half of the ice column has transition scales of ≤ 300 m which, given the gradual variations in λ_S and the direction of ice flow, indicates that region is in the tertiary state.

~~Many large-scale ice sheet model simulations are run using approximations to the full Stokes (FS)equations, notably higher order (HO, e.g., Blatter, 1995; Pattyn, 2003) , shelfy-stream (e.g., MacAyeal, 1989; Morland and Zainuddin, 1987) , or~~

25 ~~shallow ice (e.g., Hutter, 1982) approximations. We compared the ESTAR FS simulations for the embayed ice shelf, ISMIPB, and ISMIPD, with corresponding HO simulations. The local differences between the ESTAR FS and HO simulations were typically smaller than the corresponding differences between ESTAR and the Glen rheology. However, we only performed simulations in idealised situations where the approximations underlying the HO flowequations were generally expected to hold. We anticipate more pronounced differences between the FS and HO flow equations in regions where these assumptions~~

30 ~~fail.The magnitude of such differences will be explored in future studies~~For ISMIPB with $L = 5$ km, which displays a generally deeper band of normal stress dominated regime (Fig. 7d), the transition scales for the compressive and extensive regions are ~ 500 m for regions of ≈ 1 km in extent, while the shear transition scales at 100 m depth above the bump and 200 m depth above the depression are now ~ 10 km and ~ 1 km, respectively. For most of the domain the transition rates in the lower half of the ice column are ≤ 100 m, although this rises to nearly 1000 m above the bedrock bump.

In the ISMIPD case, for $L = 20$ km, the pattern of λ_S (Fig. 9a) shows there are also transitions between simple shear dominated and extension dominated deformation associated with the slippery region, with varying abruptness at different depths, and some of the contours of λ_S in this instance almost orthogonal to the ice flow. A complication is that there is very little longitudinal deformation (Fig. 9e) occurring over the slippery region because the overall flow is controlled by the periodic

5 sticky spot. Accordingly, there would not be any significant fabric evolution across this ~ 4 km region (estimated transition scales there are > 40 km) so that the tertiary assumption and using E_C (since $\lambda_S = 1$) would be inappropriate. Once again, the low strain rates here (Figs. 9e-f) translate into very stiff ice and might make the influence of ESTAR enhancement factors relatively unimportant. A factor of 100 in $\dot{\varepsilon}_e$ changes viscosity by a factor of 21.5, whereas the maximum viscosity contrast from $E(\lambda_S)$ is 1.39. The shear strain rates are also very low, with transition scales > 1 km except very close to the bed over

10 the sticky spot. Accordingly, while a compatible fabric could be expected where the large λ_S values are shown in Fig. 6a, its presence would be due to the periodic flow, and the inability of the $\lambda_S \sim 0$ region to modify it.

For the last test, ISMIPD with $L = 5$ km, strain-rates are once again very low, and there is no simple structure to the picture of the stress regime portrayed by λ_S in Fig. 10f. Below mid-depth there is a periodically continuous band of shear that might favour the development of crystal anisotropy, but clearly the tertiary flow assumption of ESTAR would not be particularly

15 useful here.

The focus of this study was to explore the effect ~~of a contrast between the predicted~~ on the dynamic response of ~~an ice sheet to~~ ice sheets of using an anisotropic (ESTAR) description of rheology, sensitive to the varying proportions of simple shear and normal stresses ~~when using isotropic~~, compared to using the standard (Glen) ~~and anisotropic (ESTAR) descriptions~~ isotropic description of rheology. Our results, particularly with respect to the differences between the Glen and ESTAR simulations, are

20 sensitive to the choice of E_S and E_C. Experimental evidence (Treverrow et al., 2012) suggests that the ratio $E_S/E_C = 8/3$, rather than their overall magnitude, is the dominant control in the level of enhancement $E(\lambda_S)$ and corresponding dynamic response of grounded and floating ice sheets. Here, we used values of $E_S = 8$ and $E_C = 3$, which are based on laboratory experiments of tertiary creep (Treverrow et al., 2012), and which yield values for the overall enhancement that are compatible with estimates from borehole inclination measurements (e.g., Russell-Head and Budd, 1979) and modelling studies (e.g., Wang

25 and Warner, 1999). Nevertheless, further investigation into suitable values of E_S and E_C to use in numerical modelling studies of grounded and floating ice sheets is warranted. Indeed, with the implementation of ESTAR in ISSM, it might be possible to use inverse methods to search for values of E_S and E_C that improved the match between modelled and observed surface velocities.

In order to examine the impact of an anisotropic rheology on simulated ice dynamics, the ISMIP-HOM and embayed ice shelf

30 experiments were carried out assuming isothermal conditions. However, as discussed earlier, real ice sheets and ice shelves typically have cold, upper layers and strong vertical gradients in temperature, and these will often be stronger controls on vertical contrasts in deformation rates, through $A(T')$ (Eqs. 2-3), than a factor of 3 to 8 produced by anisotropic enhancement.

7 Conclusions

We have investigated ~~anisotropic flow~~ some consequences of incorporating the flow properties of anisotropic ice into modelling flow in ice sheets and ice shelves. Specifically, we have investigated the flow response to prolonged deformation under a constant or slowly changing stress regime and the associated development of an anisotropic crystal orientation fabric compatible with that deformation, as represented by the empirical, scalar, tertiary, anisotropic rheology ~~ESTAR,~~ of Budd et al. (2013) – ESTAR. Having implemented this rheology in ISSM, we made initial studies in the context of idealised experiments: for an embayed ice shelf, and in two-dimensional models of grounded ice flow over ~~bumpy or sticky beds~~ varying topography and variable basal friction previously explored by ice flow modellers (Pattyn et al., 2007, 2008) . We have demonstrated that ESTAR is a computationally-efficient anisotropic rheology for large-scale ice sheet models. We have highlighted that ESTAR produces different flow responses compared with the prevailing rheological description based on the Glen flow relation, in regions where simple shear and normal stresses, and combinations of these, are drivers of ice flow. ~~Further~~ We have also noted some possible limitations of this empirical treatment of the tertiary flow regime, although their significance and whether there is scope for developing the empirical approach to resolve them remain to be determined. It would also be interesting to compare ESTAR with the predictions of modelling that uses more complex rheological descriptions, even if the comparison was limited to local domains or idealised cases.

Our embayed ice shelf results have significant implications for ice sheet model simulations that rely on the Glen flow relation to simulate past, present, and future ice flow, which are used to constrain uncertainty in reconstructions and projections of sea levels. In particular, the effect of unrealistically fast thinning ice near the calving front, as simulated with the Glen flow relation, is to deform the ice shelf, which could lead to unrealistic ice shelf geometries and affect buttressing if it were to spread beyond the "passive ice" sector (Furst et al., 2016) near the ice front.

With the implementation of ESTAR into ISSM completed, further investigation into the capabilities of ESTAR to replicate real-world ice sheet flow in Antarctic outlet glaciers is currently underway.

References

Azuma, N. and Goto-Azuma, K.: An anisotropic flow law for ice sheet ice and its implications, Ann. Glaciol., 23, 202–208, 1996.

Blatter, H.: Velocity And Stress-Fields In Grounded Glaciers: A Simple Algorithm For Including Deviatoric Stress Gradients, J. Glaciol., 41, 333–344, 1995.

Breuer, B., Lange, M. A., and Blindow, N.: Sensitivity studies on model modifications to assess the dynamics of a temperature ice cap, such as that on King George Island, Antarctica, J. Glaciol., 52, 235–247, 2006.

Budd, W. and Jacka, T.: A review of ice rheology for ice sheet modelling, Cold Reg. Sci. Technol., 16, 107–144, 1989.

Budd, W. F.: The development of crystal orientation fabrics in moving ice, Z. Gletscherkd. Glazialgeol, 8, 65–105, 1972.

Budd, W. F., Warner, R. C., Jacka, T. H., Li, J., and Treverrow, A.: Ice flow relations for stress and strain-rate components from combined shear and compression laboratory experiments, J. Glaciol., 59, 374–392, doi:10.3189/2013JoG12J106, 2013.

Cuffey, K. and Paterson, W. S. B.: The Physics of Glaciers, 4th Edition, Elsevier, Oxford, 2010.

DiPrinzio, C., Wilen, L., Alley, R., Fitzpatrick, J., Spencer, M., and Gow, A.: Fabric and texture at Siple Dome, Antarctica, J. Glaciol., 51, 281–290, 2005.

Durand, G., Gagliardini, O., Zwinger, T., Le Meur, E., and Hindmarsh, R.: Full Stokes modeling of marine ice sheets: influence of the grid size, Ann. Glaciol., 50, 109–114, 2009.

Duval, P.: Creep and fabrics of polycrystalline ice under shear and compression, J. Glaciol., 27, 129–140, 1981.

Ern, A. and Guermond, J.-L.: Applied Mathematical Sciences, vol. 159, chap. Theory and practice of finite elements, pp. 175–217, Springer, 2004.

Faria, S. H., Weikusat, I., and Azuma, N.: The microstructure of polar ice. Part II: State of the art, J. Struct. Geol., 61, 21 – 49, doi:10.1016/j.jsg.2013.11.003, 2014.

Furst, J. J., Durand, G., Gillet-Chaulet, F., Tavard, L., Rankl, M., Braun, M., and Gagliardini, O.: The safety band of Antarctic ice shelves, Nat. Clim. Change, 6, 479–482, doi:10.1038/NCLIMATE2912, 2016.

Gagliardini, O., Gillet-Chaulet, F., and Montagnat, M.: A review of anisotropic polar ice models: from crystal to ice-sheet flow models, in: Physics of Ice Core Records II, edited by Hondoh, T., pp. 149–166, Institute of Low Temperature Science, Hokkaido University, Sapporo, Japan, 2009.

Gao, X. and Jacka, T.: The approach to similar tertiary creep rates for Antarctic core ice and laboratory prepared ice, Journal de Physique, Colloque C1, supplement to no. 3, Tome 48, pp. 289–296, 1987.

Gillet-Chaulet, F., Gagliardini, O., Meyssonnier, J., Montagnat, M., and Castelnau, O.: A user-friendly anisotropic flow law for ice-sheet modelling, J. Glaciol., 51, 3–14, doi:10.3189/172756505781829584, 2005.

Glen, J.: The creep of polycrystalline ice, Proc. R. Soc. A, 228, 519–538, 1955.

Glen, J.: The flow law of ice: A discussion of the assumptions made in glacier theory, their experimental foundations and consequences, IASH Publ, 47, 171–183, 1958.

Glen, J. W.: Experiments on the deformation of ice, J. Glaciol., 2, 111–114, 1952.

Glen, J. W.: Rate of flow of polycrystalline ice, Nature, 172, 721–722, 1953.

Gödert, G.: A mesocopic approach for modelling texture evolution of polar ice including recrystallisation phenomena, Ann. Glaciol., 37, 23–28, doi:10.3189/172756403781815375, 2003.

Greve, R.: Application of a polythermal three-dimensional ice sheet model to the Greenland Ice Sheet: Response to steady-state and transient climate scenarios, J. Clim., 10, 901–918, 1997.

Greve, R.: Relation of measured basal temperatures and the spatial distribution of the geothermal heat flux for the Greenland ice sheet, Ann. Glaciol., 42, 424–432, 2005.

5 Greve, R. and Blatter, H.: Dynamics of Ice Sheets and Glaciers, Advances in Geophysical and Environmental Mechanics and Mathematics, Springer-Verlag, 2009.

Greve, R. and Blatter, H.: Comparison of thermodynamics solvers in the polythermal ice sheet model SICOPOLIS, Polar Science, 10, 11 – 23, doi:http://dx.doi.org/10.1016/j.polar.2015.12.004, 2016.

Hulbe, C. L., Wang, W., Joughin, I. R., and Siegert, M. J.: The role of lateral and vertical shear in tributary flow toward a West Antarctic ice

10 stream, Ann. Glaciol., 36, 244–250, 2003.

Hutter, K.: Dynamics of glaciers and large ice masses, Ann. Rev. Fluid Mech., 14, 87–130, 1982.

Huybrechts, P., Rybak, O., Pattyn, F., Ruth, U., and Steinhage, D.: Ice thinning, upstream advection, and non-climatic biases for the upper 89% of the EDML ice core from a nested model of the Antarctic ice sheet, Clim. Past, 3, 577–589, 2007.

Jacka, T. and Maccagnan, M.: Ice crystallographic and strain rate changes with strain in compression and extension, Cold Reg. Sci. Technol.,

15 8, 269–286, 1984.

Jaeger, J. C.: Elasticity, fracture and flow: with engineering and geological applications, Methuen, 3rd edn., 1969.

Kamb, B.: Experimental recrystallization of ice under stress, American Geophysical Union, 1973.

Kipfstuhl, S., Faria, S., Azuma, N., Freitag, J., Hamann, I., Kaufmann, P., Miller, H., Weiler, K., and Wilhelms, F.: Evidence of dynamic recrystallization in polar firn, J. Geophys. Res., 114, B05 204, 2009.

20 Larour, E., Seroussi, H., Morlighem, M., and Rignot, E.: Continental scale, high order, high spatial resolution, ice sheet modeling using the Ice Sheet System Model (ISSM), J. Geophys. Res., 117, 1–20, doi:10.1029/2011JF002140, 2012.

Li, J. and Jacka, T.: Correspondence. Horizontal shear rate of ice initially exhibiting vertical compression fabrics, J. Glaciol., 44, 670–672, 1998.

Li, J., Jacka, J., and Budd, W. F.: Deformation rates in combined compression and shear for ice which is initially isotropic and after the

25 development of strong anisotropy, Ann. Glaciol., 23, 247–252, 1996.

Lile, R.: The effect of anisotropy on the creep of polycrystalline ice, J. Glaciol., 21, 475–483, 1978.

Lliboutry, L.: Anisotropic, transversely isotropic nonlinear viscosity of rock ice and rheological parameters inferred from homogenization, Int. J. Plasticity, 9, 619–632, 1993.

Ma, Y., Gagliardini, O., Ritz, C., Gillet-Chaulet, F., Durand, G., and Montagnat, M.: Enhancement factors for grounded ice and ice shelves

30 inferred from an anisotropic ice-flow model, J. Glaciol., 56, 805–812, 2010.

MacAyeal, D.: Large-scale ice flow over a viscous basal sediment: Theory and application to Ice Stream B, Antarctica, J. Geophys. Res., 94, 4071–4087, 1989.

Martín, C. and Gudmundsson, G. H.: Effects of nonlinear rheology, temperature and anisotropy on the relationship between age and depth at ice divides, The Cryosphere, 6, 1221–1229, doi:10.5194/tc-6-1221-2012, 2012.

35 Martin, M. A., Winkelmann, R., Haseloff, M., Albrecht, T., Bueler, E., Khroulev, C., and Levermann, A.: The Potsdam Parallel Ice Sheet Model (PISM-PIK) - Part 2: Dynamic equilibrium simulation of the Antarctic ice sheet, Cryosphere, 5, 727–740, doi:10.5194/tc-5-727-2011, 2011.

Montagnat, M., Azuma, N., Dahl-Jensen, D., Eichler, J., Fujita, S., Gillet-Chaulet, F., Kipfstuhl, S., Samyn, D., Svensson, A., and Weikusat, I.: Fabric along the NEEM ice core, Greenland, and its comparison with GRIP and NGRIP ice cores, The Cryosphere, 8, 1129–1138, doi:10.5194/tc-8-1129-2014, 2014.

Morgan, V., Wookey, C., Li, J., van Ommen, T., Skinner, W., and Fitzpatrick, M.: Site information and initial results from deep ice drilling on Law Dome, Antarctica, J. Glaciol., 43, 3–10, 1997.

Morgan, V., van Ommen, T., Elcheikh, A., and Li, J.: Variations in shear deformation rate with depth at Dome Summit South, Law Dome, East Antarctica, Ann. Glaciol., pp. 135–139, 1998.

Morland, L. and Zainuddin, R.: Plane and radial ice-shelf flow with prescribed temperature profile., In Veen, C.J. van der, and Oerlemans, J., eds. Dynamics of the West Antarctica Ice Sheet. Proceedings of a Workshop held in Utrecht, May 6-8, 1985. Dordrecht, D. Rediel Publishing Company, 117, 117–140, 1987.

Nye, J. F.: The flow law of ice from measurements in glacier tunnels, laboratory experiments and the Jungfraufirn borehole experiment, Proc. R. Soc. A, 219, 477–489, 1953.

Parizek, B. R. and Alley, R. B.: Implications of increased Greenland surface melt under global-warming scenarios: ice-sheet simulations, Quat. Sci. Rev., 23, 1013–1027, 2004.

Paterson, W.: The Physics of Glaciers, Pergamon Press, Oxford, London, New York, 3rd edn., 1994.

Pattyn, F.: A new three-dimensional higher-order thermomechanical ice sheet model: Basic sensitivity, ice stream development, and ice flow across subglacial lakes, J. Geophys. Res., 108, 1–15, doi:10.1029/2002JB002329, 2003.

Pattyn, F., Perichon, L., Aschwanden, A., Breuer, B., De Smedt, B., Gagliardini, O., Hindmarsh, R., Hubbard, A., Johnson, J., Kleiner, T., Konovalov, Y., Martin, C., Payne, T., Pollard, D., Price, S., Saito, F., and Sugiyama, S.: ISMIP-HOM: Results of the Higher-Order Ice Sheet Model Intercomparison Project, in: European Geosciences Union, 2007.

Pattyn, F., Perichon, L., Aschwanden, A., Breuer, B., de Smedt, B., Gagliardini, O., Gudmundsson, G. H., Hindmarsh, R. C. A., Hubbard, A., Johnson, J. V., Kleiner, T., Konovalov, Y., Martin, C., Payne, A. J., Pollard, D., Price, S., Rückamp, M., Saito, F., Soucek, O., Sugiyama, S., and Zwinger, T.: Benchmark experiments for higher-order and full-Stokes ice sheet models (ISMIP-HOM), The Cryosphere, 2, 95–108, 2008.

Pettit, E., Thorsteinsson, T., Jacobson, H., and Waddington, E.: The role of crystal fabric in flow near an ice divide, J. Glaciol., 53, 277–288, doi:10.3189/172756507782202766, 2007.

Pimienta, P., Duval, P., and Lipenkov, V. Y.: Mechanical behaviour of anisotropic polar ice, in: The Physical Basis of Ice Sheet Modelling, pp. 57–65, IAHS Publ. 170, 1987.

Placidi, L., Greve, R., Seddik, H., and Faria, S.: Continuum-mechanical, Anisotropic Flow model, for polar ice masses, based on an anisotropic Flow Enhancement factor, Continuum Mech. Thermodyn., 22, 221–237, doi:10.1007/s00161-009-0126-0, 2010.

Russell-Head, D. and Budd, W.: Ice-sheet flow properties derived from bore-hole shear measurements combined with ice-core studies, J. Glaciol., 24, 117–130, 1979.

Saito, F. and Abe-Ouchi, A.: Thermal structure of Dome Fuji and east Dronning Maud Land, Antarctica, simulated by a three-dimensional ice-sheet model, in: Ann. Glaciol., VOL 39, edited by Jacka, J, vol. 39 of *Ann. Glaciol.*, INT GLACIOLOGICAL SOC, LENSFIELD RD, CAMBRIDGE CB2 1ER, ENGLAND, 2004.

Schmid, E. and Boas, W.: Plasticity of crystals, F.A. Hughes and Co. Ltd., London, 1950.

Seddik, H., Greve, R., Zwinger, T., and Placidi, L.: A full Stokes ice flow model for the vicinity of Dome Fuji, Antarctica, with induced anisotropy and fabric evolution, The Cryosphere, 5, 495–508, doi:10.5194/tc-5-495-2011, 2011.

Staroszczyk, R. and Gagliardini, O.: Two orthotropic models for strain-induced anisotropy of polar ice, J. Glaciol., 45, 485–494, 1999.

Tarasov, L. and Peltier, W. R.: A geophysically constrained large ensemble analysis of the deglacial history of the North American ice-sheet complex, Quat. Sci. Rev., 23, 359=388, 2004.

Thorsteinsson, T.: An analytical approach to deformation of anisotropic ice-crystal aggregates, J. Glaciol., 47, 507–516, 2001.

5   Thorsteinsson, T.: Fabric development with nearest-neighbour interaction and dynamic recrystallization, J. Geophys. Res. - Solid Earth, 107, doi:10.1029/2001JB000244, 2002.

Treverrow, A., Budd, W. F., Jacka, T. H., and Warner, R. C.: The tertiary creep of polycrystalline ice: experimental evidence for stress-dependent levels of strain-rate enhancement, J. Glaciol., 58, 301–314, doi:10.3189/2012JoG11J149, 2012.

Treverrow, A., Warner, R. C., Budd, W. F., Jacka, T. H., and Roberts, J. L.: Modelled stress distributions at the Dome Summit South borehole,

10   Law Dome, East Antarctica: a comparison of anisotropic ice flow relations, J. Glaciol., 61, 987–1004, doi:13.3189/2016JoG14J198, 2015.

Treverrow, A., Jun, L., and Jacka, T. H.: Ice crystal c-axis orientation and mean grain size measurements from the Dome Summit South ice core, Law Dome, East Antarctica, Earth System Science Data, 8, 253–263, doi:10.5194/essd-8-253-2016, 2016.

Trickett, Y., Baker, I., and Pradhan, P.: The orientation dependence of the strength of ice single crystals, J. Glaciol., 46, 41–44, doi:10.3189/172756500781833296, 2000.

15   van der Veen, C. J. and Whillans, I. M.: Force budget: I. Theory and numerical methods, J. Glaciol., 35, 53–60, 1989.

van der Veen, C. J. and Whillans, I. M.: Development of fabric in ice, Cold Reg. Sci. Technol., pp. 171–195, doi:10.1016/0165-232X(94)90027-2, 1994.

Wang, W. and Warner, R. C.: Modelling of anisotropic ice flow in Law Dome, East Antarctica, Ann. Glaciol., 29, 184–190, 1999.

Wang, W., Warner, R. C., and Budd, W. F.: Ice-flow properties at Dome Summit South, Law Dome, East Antarctica, Ann. Glaciol., 35,

20   567–573, 2002a.

Wang, W., Jun, L., Zwally, H. J., Morgan, V., and van Ommen, T. D.: The effect of anistropic flow properties on ice-sheet surface elevation change, Ann. Glaciol., 39, 439–444, 2004.

Wang, W., Li, J., and Zwally, H. J.: Dynamic inland propagation of thinning due to ice loss at the margins of the Greenland ice sheet, J. Glaciol., 58, 734–740, doi:10.3189/2012JoG11J187, 2012.

25   Wang, W. L. and Warner, R. C.: Simulation of the influence of ice rheology on velocity profiles and ice-sheet mass balance, Ann. Glaciol., 27, 194–200, 1998.

Wang, W. L., Zwally, H. J., Abdalati, W., and Luo, S.: Modeling of ice flow and internal layers along a flowline through Swiss Camp, West Greenland, Ann. Glaciol., 34, 303–308, 2002b.

Wang, W. L., Zwally, H. J., Hulbe, C. L., Siegert, M. J., and Joughin, I. R.: Anisotropic ice flow leading to the onset of Ice Stream D, West

30   Antarctica: numerical modelling based on the observations from Byrd Station borehole, Ann. Glaciol., 37, 397–403, 2003.

Warner, R. C., Jacka, T. H., Li, J., and Budd, W. F.: Tertiary flow relations for compression and shear components in combined stress tests on ice, in: Advances in cold-region thermal engineering and sciences: technological, environmental, and climatological impact, edited by Hutter, K., Wang, Y., and Beer, H., pp. 259–270, Springer-Verlag, 1999.

Weertman, J.: Deformation of floating ice shelves, J. Glaciol., 3, 38–42, 1957.

35   Winkelmann, R., Martin, M. A., Haseloff, M., Albrecht, T., Bueler, E., Khroulev, C., and Levermann, A.: The Potsdam Parallel Ice Sheet Model (PISM-PIK) - Part 1: Model description, The Cryosphere, 5, 715–726, doi:10.5194/tc-5-715-2011, 2011.

Zwinger, T., Schäfer, M., Martín, C., and Moore, J. C.: Influence of anisotropy on velocity and age distribution at Scharffenbotnen blue ice area, The Cryosphere, 8, 607–621, doi:10.5194/tc-8-607-2014, 2014.
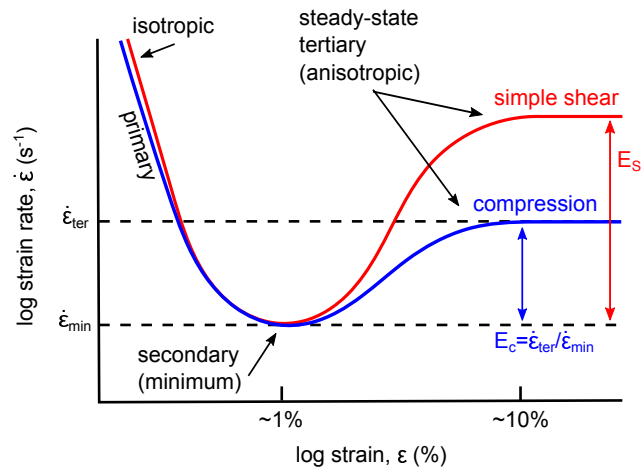
Figure 1. Strain rate characteristics of polycrystalline ice undergoing deformation driven by single stresses as measured in laboratory experiments. The part of the curve corresponding to tertiary (steady-state) anisotropic creep is relevant to the deformation of ice masses in typical ice sheets and glaciers. The red (blue) curve illustrates the result of simple shear-alone (compression-alone) stress configurations. Note that the ratio of the shear enhancement factor E_S to the compression enhancement factor E_C is approximately $8/3$, and the enhancement due to compression-alone is approximately three times that of the secondary (minimum) creep rate.
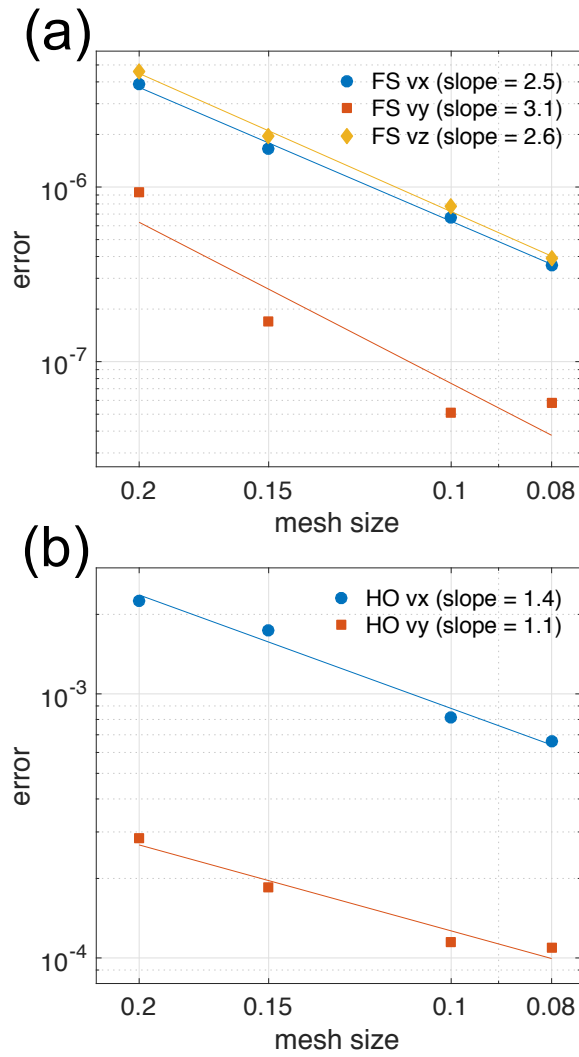
Figure 2. Convergence rates of the simulated **(a)** ~~full Stokes~~ full-Stokes (FS) and **(b)** ~~higher order~~ higher-order (HO) velocity fields (v_x, v_y, v_z) to the analytical solutions in Eqs. 13-17 for increasing mesh resolutions.
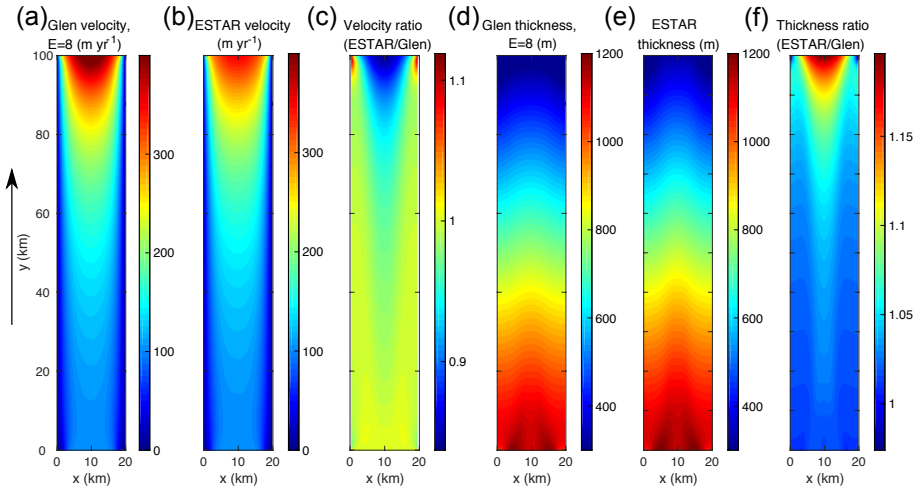
Figure 3. Rectangular ice shelf HO ~~steady-state~~ surface ~~velocity magnitudes~~ fields. **(a)** Velocity magnitude (m yr^{-1}) ~~using (a)~~ for the Glen ~~and~~ flow relation ($E_G = 8$); **(b)** velocity magnitude (m yr^{-1}) for ESTAR~~, and the corresponding~~; **(c)** ratios (i.e., ESTAR/Glen) ~~between of velocity magnitudes;~~ **(d)** thickness (m) for ~~the steady-state (c) velocities~~ Glen flow relation ($E_G = 8$); **(e)** thickness (m) for ESTAR; and ~~(d)~~ **(f)** ratios (i.e., ESTAR/Glen) thicknesses. The black arrow indicates the direction of flow.
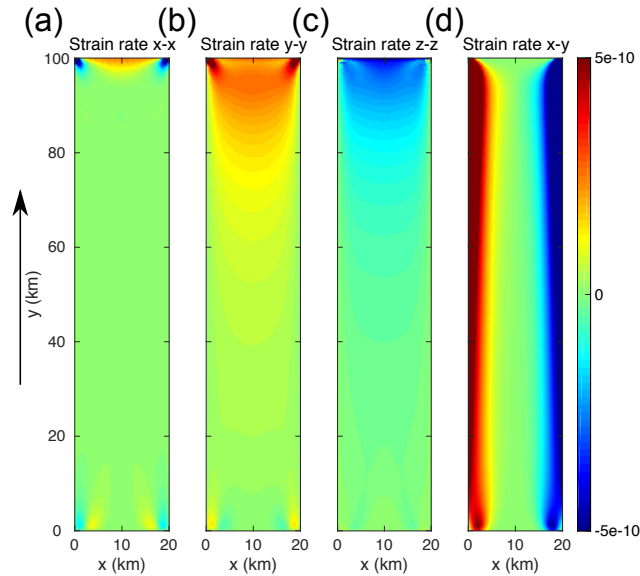

Figure 4. Rectangular ice shelf ESTAR HO steady-state surface strain rates (s^{-1}): **(a)** $\dot{\varepsilon}_{xx}$; **(b)** $\dot{\varepsilon}_{yy}$, **(c)** $\dot{\varepsilon}_{zz}$; and **(d)** $\dot{\varepsilon}_{xy}$.
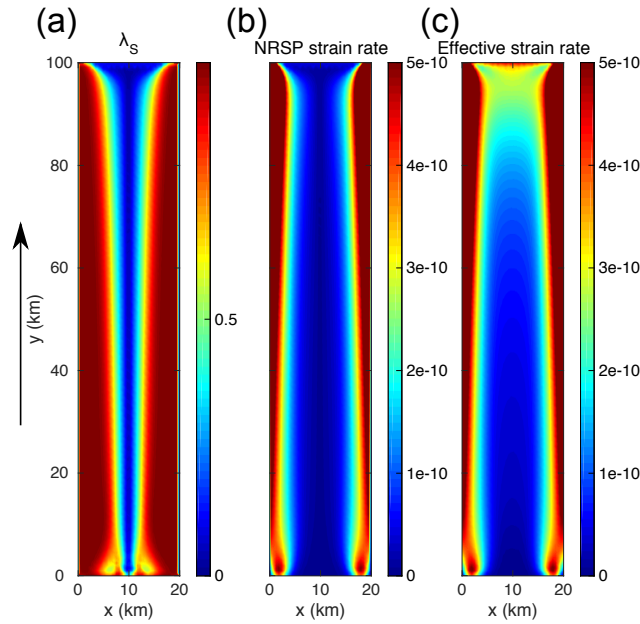
Figure 5. Rectangular ice shelf ESTAR HO steady-state surface fields. **(a)** ~~The~~ ESTAR shear ratio λ_S; **(b)** ~~the~~ shear strain rate resolved on the non-rotating shear plane (NRSP) $\dot{\varepsilon}'$ (s^{-1}); and **(c)** ~~the~~ effective strain rate $\dot{\varepsilon}_e$ (s^{-1}). The black arrow indicates the direction of flow. ~~In each case, the surface fields for the HO model are shown.~~
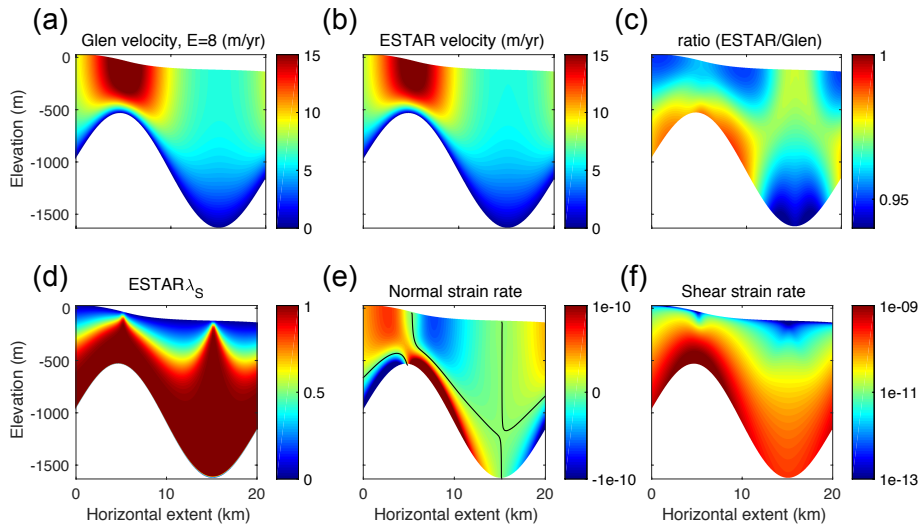

Figure 6. ISMIPB FS steady-state ~~(prognostic) along-flow velocities (v_x) for ISMIPB~~ results with horizontal extent $L = 20$ km. **(a)** Horizontal velocity v_x (m yr^{-1}) for the Glen flow relation with $E_G = 8$; **(b)** v_x (m yr^{-1}) for ESTAR with $E_S = 8$ and $E_C = 3$; and **(c)** ratio between the Glen and ESTAR v_x fields; **(d)** ESTAR shear enhancement factor λ_S (Eq. 6); **(e)** ESTAR normal strain rate (i.e., $x - x$ strain rate; s^{-1}); and **(f)** ESTAR shear strain rate (i.e., $x - z$ strain rate; s^{-1}). The black contours in **(e)** correspond to the curves where $\dot{\varepsilon}_{xx} = 0$. Note the log scale in **(f)**.
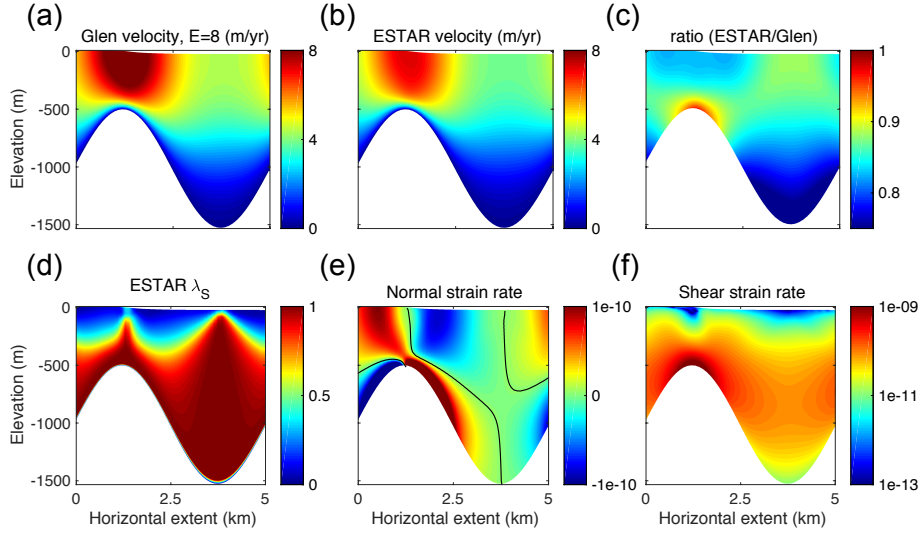
32

Figure 7. ~~Enhancement factors and normal and shear strain rates for the~~ ISMIPB FS steady-state ~~simulations~~results with horizontal extent $L = 5$ km. **(a)** ~~Shear~~ Horizontal velocity v_x (m yr^{-1}) for the Glen flow relation with $E_G = 8$; **(b)** v_x (m yr^{-1}) for ESTAR with $E_S = 8$ and $E_C = 3$; and **(c)** ratio between the Glen and ESTAR v_x fields; **(d)** ESTAR shear enhancement factor λ_S (Eq. 6); ~~(b)~~ **(e)** ESTAR normal strain rate (i.e., $x-x$ strain rate; s^{-1}); and ~~(c)~~ **(f)** ESTAR shear strain rate (i.e., $x-z$ strain rate; s^{-1}). The black contours in ~~(b)~~ **(e)** correspond to the curves where $\dot{\epsilon}_{xx} = 0$. Note the log scale in **(f)**.

~~Steady-state (prognostic) results for ISMIPB HO and FS models.~~ **(a)-(b)** ~~HO and FS along-flow velocities (v_x; m yr^{-1}), respectively;~~ **(c)** ~~ratio of the deformation velocities (HO/FS);~~ **(d)-(e)** ~~HO and FS enhancement factors λ_S, respectively, with their ratio in~~ **(f)**; ~~and~~ **(g)-(h)** ~~final HO and FS viscosities (μ; Pa s), with their ratio in panel~~ **(i)**.
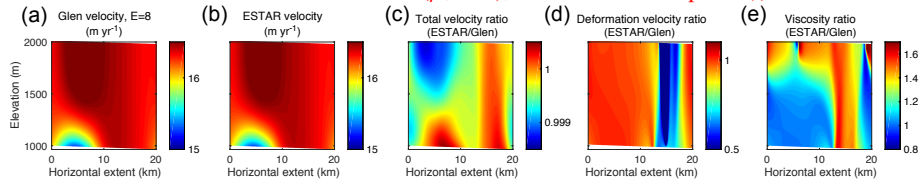

Figure 8. ISMIPD FS ~~diagnostic (stress balance – SB; (a)-(c)) and prognostic (transient – TR; (d)-(f)) along-flow velocities (v_x)~~steady-state results with horizontal extent $L = 20$ km. **(a)** ~~and (d)~~ Glen ~~SB and TR~~ horizontal velocities v_x ~~,respectively~~(m yr^{-1}); **(b)** ~~and (e)~~ ESTAR ~~SB and TR~~ v_x ~~,respectively~~(m yr^{-1}); ~~and~~ **(c)** ~~and (f)~~ ratios of ESTAR/Glen ~~to~~ v_x; **(d)** ratios of ESTAR~~SB and TR~~/Glen deformation velocities (i.e., the difference between v_x and the sliding velocity, which is taken to be equal to the velocity along the basal mesh points); and **(e)** ratios of ESTAR/Glen viscosities.
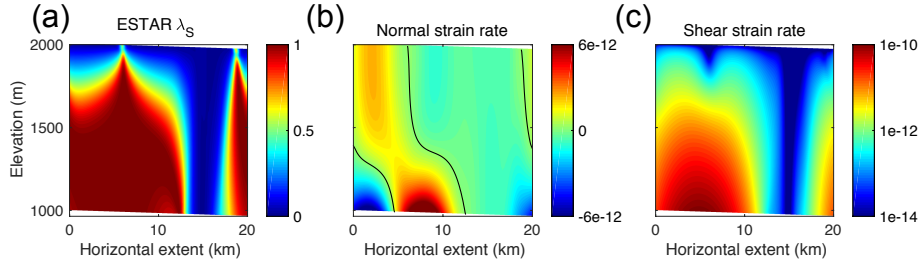
Figure 9. ISMIPD ESTAR FS ~~SB and TR~~ steady-state enhancement factors and normal and shear strain rates with horizontal extent $L = 20$ km. **(a)** ~~(d) SB and TR~~ λ_S; **(b)** ~~(e) SB and TR~~ normal strain rates (s^{-1}); and **(c)** ~~(f) SB and TR~~ shear strain rates (s^{-1}). The black contour lines in **(b)** ~~and (e)~~ correspond to the curves where $\dot{\epsilon}_{xx} = 0$. Note the log scale in **(c)**.
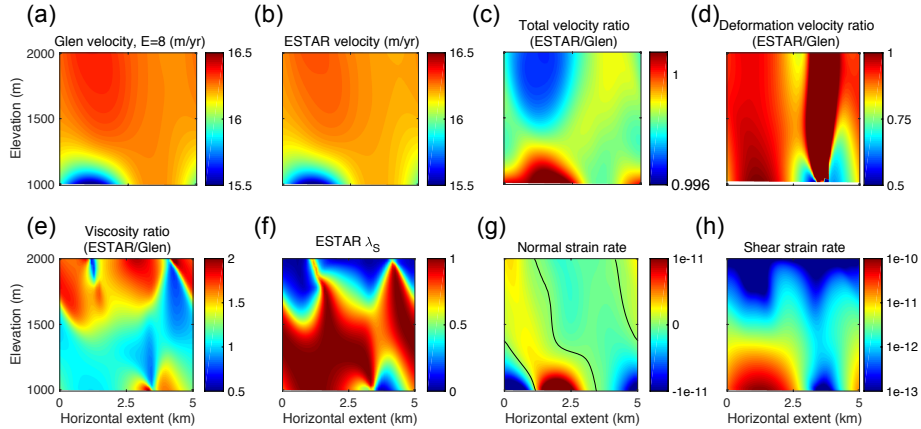

Figure 10. ISMIPD FS steady-state results with horizontal extent $L = 5$ km. **(a)** Glen horizontal velocity v_x (m yr^{-1}, with $E_G = 8$); **(b)** ESTAR v_x (m yr^{-1}); **(c)** ratio of ESTAR/Glen v_x; **(d)** ratio of ESTAR/Glen deformation v_x; **(e)** ratio of ESTAR/Glen viscosity; **(f)** ESTAR λ_S; **(g)** ESTAR normal strain rate (s^{-1}); and **(h)** ESTAR shear strain rate (s^{-1}). The black contours in **(g)** correspond to the curves where $\dot{\varepsilon}_{xx} = 0$. Note the log scale in **(h)**.

34

Table 1. Computational times for ~~full Stokes~~ full-Stokes simulations of the embayed ice shelf (~~section~~Sect. 5.1) using Glen and ESTAR for increasing mesh resolution. The model is simulated for 1 month and for a total of 833 time steps in each case. Dof stands for model degrees of freedom.

Dof	Vertices	CPUs	Glen walltime (s)	ESTAR walltime (s)
2210	10040	16	9084	9281
2760	15665	32	10467	10778
3310	22540	64	12920	13008
4410	40040	128	20852	21008
8820	80080	256	59057	59934